NUMERICAL CONSTITUTIVE MODELS OF WOVEN AND BRAIDED TEXTILE STRUCTURAL COMPOSITES

by

Nicolas Chretien

Thesis submitted to the faculty of Virginia Polytechnic Institute and State University in partial fulfillment of the requirements for the degree of

Master of Science

in

Aerospace Engineering

Approved:

Dr. Eric R. Johnson, Chair

Dr. Rakesh K. Kapania

Dr. Michael W. Hyer

April 16, 2002

Blacksburg,Virginia

Keywords: Composite materials, textile structural composites, woven and braided fabrics, homogenization, effective moduli, constitutive models, progressive failure.

NUMERICAL CONSTITUTIVE MODELS OF WOVEN AND BRAIDED TEXTILE STRUCTURAL COMPOSITES

by

Nicolas Chretien

(ABSTRACT)

Equivalent, three-dimensional elastic moduli are determined from unit cell models of balanced plain weave, 2D braid, 2D triaxial braid and 4x4 twill textile composite materials consisting of interlaced or intertwined yarns. The yarn paths are modeled with undulation portions, in which one yarn passes over and under one or more yarns, and with straight portions. It is assumed that the centerline of a yarn in the undulation portions is described by the sine function, and that the cross-sectional area of a yarn and the thickness of a yarn, normal to the centerline, are uniform along the centerline.

For the balanced plain weave architecture, equations for the fiber volume fraction and the cross-sectional shape of the yarn are derived for large crimp angles. It is shown that the maximum crimp angle is limited to forty-five degrees, and that limits on the ratio of the length of the undulation portion of the path to the width of the unit cell impose constraints on the fiber volume fraction and yarn packing density. For small crimp angles, approximations to the volume fraction and yarn shape equations are obtained. This assumption is used in the derivation of the geometry of the remaining architectures, and subsequent equations are obtained for the corresponding geometric parameters.

For each architecture, the yarns are assumed to be transversely isotropic and a stress averaging technique based on an iso-strain assumption is used to determine the effective moduli of the unit cells. Comparisons of the effective moduli are made to other unit cell models in the literature.

The micromechanical models are implemented in Fortran programs and user material subroutines for ABAQUS[1], called UMAT, are created out of these programs. For a balanced plain weave fabric under the small crimp angle approximation, a progressive failure model is developed to predict failure within each yarn and to degrade the material properties of the representative unit cell. Material failure is predicted by discretizing the yarns into slices and applying Tsai-Wu quadratic criterion to the on-axis strains in each slice. A stiffness and strength reduction scheme is then used to account for the change in yarn compliance.

At the present time, the UMAT has only been tested as a stand-alone program with Visual Fortran 6.0, and would require further development to be used within ABAQUS on sample structural problems.

1. ABAQUS is a registered trademark of Hibbitt, Karlsson & Sorensen, Inc.

Dedication

This work is dedicated to Jean-Claude and Catherine Chretien, my parents, and my brother, Jerome. With all my love.

Acknowledgements

The author would like to acknowledge the following for their contribution and support in this work:

- Mr. Naveen Rastogi, technical fellow for the Chassis Advanced Technology Department at Visteon Corporation, who supported financially and supervised this project. I am very grateful to him for giving me the resources to perform my work.
- Dr. Eric Johnson, my advisor, for giving me the opportunity to work on this project and guiding me throughout my research studies. I am deeply obliged to him for his constant support and availability, as well as his helpful and numerous advises.
- Dr. Hyer and Dr. Kapania for taking the time to be on my advisory committee.
- Vinay Goyal for helping me with the programming part of the project and providing me with many beneficial information about ABAQUS. I wish to thank him also for his friendship and his happiness always lighting up the graduate computer lab.
- Sneha Pattel for helping me with the fiber volume fraction measurements in the ESM composite lab.
- Ms. Betty Williams for helping me with all the (complex) paper work a graduate student has (unfortunately) to go through, I would like to express my gratitude for her availability and her kindness.
- Last but not least, I would like to thank my parents for their support and endless love all these years, my brother Jerome for keeping me informed of the ‘family stories’ overseas, my friends here in VT, that I will always remember: Rodolf, Nerio, Anne, Nico, Dave, Will, Vero...

Table of Contents

List of Figures

List of Tables

Chapter 1. Introduction & Literature Review

1.1 Introduction

Textile structural composites represent a class of advanced materials which are reinforced with textile preforms for structural or load bearing applications. Presently, textile structural composites are part of a larger category of composite materials: textile composites.

In general, composites can be defined as a select combination of dissimilar materials with a specific internal structure and external shape. The unique combination of two material components leads to singular mechanical properties and superior performance characteristics not possible with any of the components alone. Additionally composite materials are often overwhelmingly superior to other materials (e.g. metals) on a strength-to-weight or stiffness-to-weight basis. With this reassurance, the range of applications for composite materials appears to be limitless.

Textile composites can be defined as the combination of a resin system with a textile fiber, yarn or fabric system. They may be either flexible or quite rigid. Flexible textile composites include, for example, heavy duty conveyor belts or inflatable life rafts. On the other hand, examples of inflexible or rigid textile composites are found in a variety of products referred to as fiber reinforced plastic (FRP) systems. These textile composites have been used since the 1950’s mostly in interior and exterior panels and in parts for the automotive and aircraft industry and represent a good alternative for metal and wood applications.

Textile structural composite are mainly use as structural materials to resist heavy loads that occur in the basic framework for buildings, bridges, vehicles, etc. The vast majority of textile structural composites are fiber reinforced plastics (FRP). They are made of a textile

composite preform embedded in a resin, metal or ceramic matrix. The matrix system provides rigidity and holds the textile reinforcement material in a prescribed position and orientation in the composite. The composite preform is obtained from the assemblage of unrigidized fibrous material (fibers, yarns or fabrics) and its architecture can vary from a simple planar sheet to a complex 3D net shape.

Textile structural composites have been the focus of many aircraft and automotive manufacturers for more than two decades. They offer a good alternative to develop composite primary structures for commercial transport airplanes with costs that are competitive with those of current metallic airplanes. Textile composites were considered for many components to improve structural performance and to reduce costs. Boeing and Lockheed-Martin evaluated textile composites for fuselage frames, window belt reinforcements, and various keel components of the fuselage. Northrop-Grumman evaluated textile concepts for making stiffened skins using 3-D textile composites, and McDonnell Douglas evaluated knitted, braided, and stitched textile fabrics for a wing box. A large part of the early investigations on textile structural composite applications were conducted within the scope of the textile working group within NASA's Advanced Composites Technology (ACT) program. Some of the most important and earliest research carried out into textile composite science were gathered in Ref. [1].

As a result of this increasing interest in textile structural composites, numerous micromechanical models to predict effective strengths and stiffnesses of such composites have been developed. Most of these models, even though they are based on rather very simplifying assumptions, provide a fairly good approximation of textile effective mechanical properties. Most of all, programming of these models provide engineers with powerful tools to compute effective properties for use in FEM softwares and a cost-effective alternative to extensive testing.

In the following sections, a general description of basic textile composite structures and mechanical features will be presented. Secondly some of the earliest micromechanical

models for analyzing woven and braided fabrics will be highlighted. Then a brief description of progressive failure models for textile composites will be outlined and finally, the objectives of this thesis will be discussed.

1.2 Overview of Textile Structural Composites

The mechanics of textile structural composites can be best studied by taking into account their hierarchical organization.There are usually four important levels in the manufacturing process of textile composites:

FIBER > YARN > FABRIC > COMPOSITE

The choice of the fibers represents the first step in the fabrication of textile structural composites. To resist high loads in structural applications, textile structural composite products must be made from high modulus fibers, e.g. glass, graphite, aramid, ceramic or steel fibers.

The second step of the manufacturing process consists of grouping together the fibers (or filaments) in a linear assemblage to form a continuous strand having textile-like characteristics. The group of filaments is then impregnated with resin (for non-hybrid fabrics, the resin is the same for all the strands and usually the same for the preform) and the resulting tubular form is called yarn. Fig. 1.1 shows different examples of idealized models of various yarn structures

.

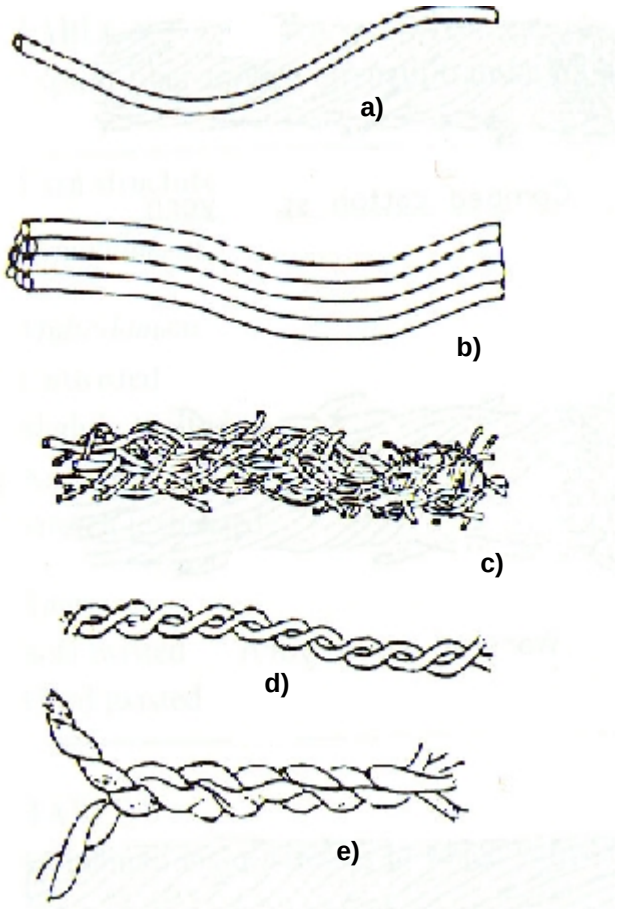

Fig. 1.1 Idealized models of various yarn structures [2]

As illustrated by the figure, yarns may be composed of one (a) or more (b) continuous filaments, or even discontinuous chopped fibers (c), and finally, two or more single yarns can be twisted together to form ply or plied yarns (d and e). Thus, the manufacturing process of yarns itself can involve rather complicated shapes. For our purpose we will only be concerned with continuous filament yarns where the filaments are not twisted together (ex. (b)).

Yarn structural features are characterized by several geometrical parameters, as the number of filaments, n, the diameter of the filaments (assuming the fibers have a cylindri-

cal shape), d_f, and the yarn packing density, p_d, defined as the ratio of the fiber volume to the yarn overall volume. Yarn structure plays a dominant role in the translation of fiber properties into yarn properties. For example, typical fiber-to-yarn strength translation efficiencies in various yarn structures for ordinary textile composites are listed in Table 1.1.

Table 1.1: Typical fiber-to-yarn strength translation efficiencies in various yarn structures

Yarn Structure	Strength translation efficiency (%)[a]
Monofilament	100
Multifilament	
Untwisted	98
Slightly Twisted	95
Air jet texturized	85
Stretch texturized	85

a. From Ref. [2]

Table 1.1 shows that the mechanical properties of the yarns are mainly dictated by the fiber obliquity (orientation relative to the yarn axis) and the fiber entanglement in the various structural forms. For multifilament untwisted yarn structures, the strength translation efficiency ratio is close to 100%, therefore the behavior of these yarns is very close to that of the fibers themselves. The loss of strength in the fiber direction is due mostly to degradation during yarn processing and lack of toughness. Also, the fibers are usually assumed to be transversely isotropic and the resin isotropic, such that untwisted yarns can be considered as transversely isotropic.

The third step in the textile structural composites manufacturing process consists of bonding and interlocking the yarns together to produce a flat sheet with a specific pattern. Fabric types are categorized by the orientation of the yarns used, and by the various con-

struction methods used to hold the yarns together. The periodicity of the repeating pattern in a textile fabric can usually be used to isolate a small repeating unit cell (RUC) which is sufficient to describe the fabric architecture. The four basic fabric structure categories are wovens, knits, braids, and nonwovens as described in Fig. 1.2.

	Woven	Knitted	Braided	Nonwoven
Geometry				
Cell model	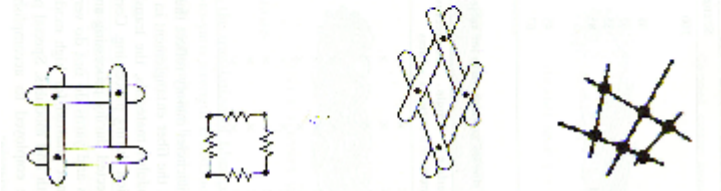			
Composition	yarn	yarn	yarn	fibers
Formation	interlace	interloop	intertwine	bond

Fig. 1.2 Comparison of basic fabric structures [2]

The interlacing of the yarns in a fabric leads to yarn undulation or ‘crimp’. As we will see in the forthcoming chapter, yarn crimp has a critical influence on the composite stiffness and strength properties. Other factors such as drape (the ability of a fabric to conform to a complex surface), stability, or porosity are also very important for the manufacturer.

Wovens: Woven fabrics are produced on a loom by the interlacing of warp (0°) and fill (90°) yarns in a regular pattern or weave style. The fabric's integrity is maintained by the mechanical interlocking of the yarns. Drape, surface smoothness and stability of the fabric are controlled primarily by the weave style. Fig. 1.3 shows miscellaneous woven

fabric structures. Currently, the most common constructions are plain, twill, basket and satin weaves.

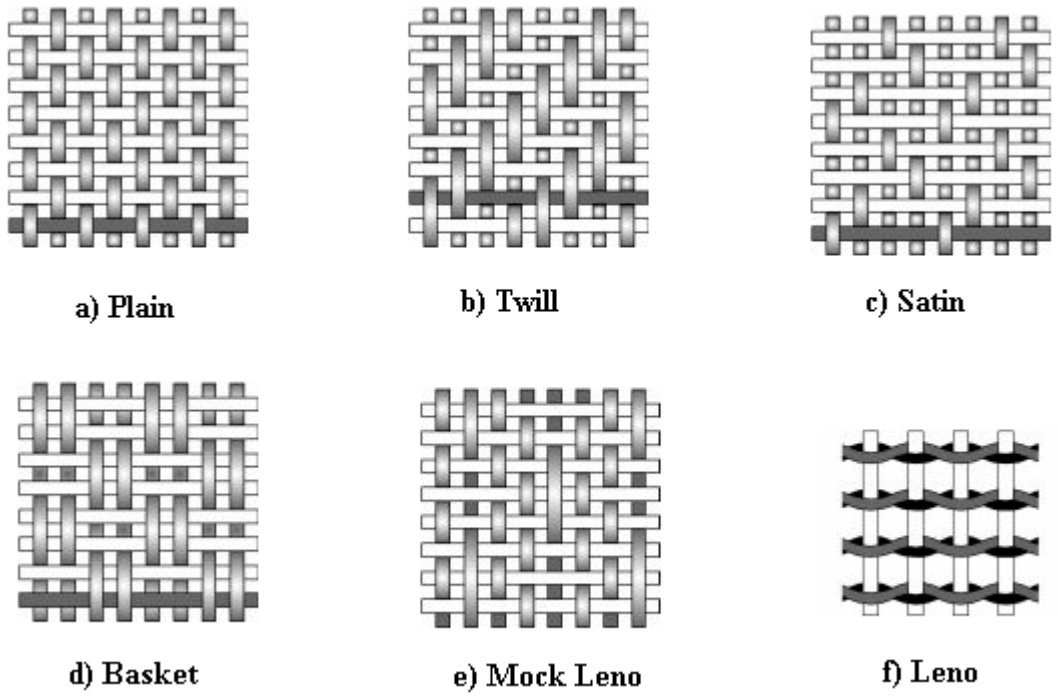

Fig. 1.3 Comparison of most common woven fabric structures [3]

Knits: Knits fabrics are usually made by interlooping one or more yarns and offer a much wider range of forms and behaviors than wovens. Simple fill (or weft) and warp knit constructions (Fig. 1.4 a) provide considerable extensity in all directions and therefore are quite suitable for deep-draw molded composites. They can also be added to a woven or braided preform for specific directional extensibility and good stability. In this case, the knitting threads are passed around the primary yarns and one another in interpenetrating loops as shown in Fig. 1.4 b.

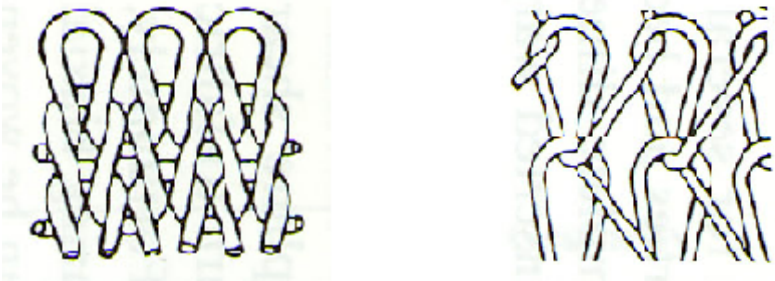

Fig. 1.4 (a) Simple warp and weft knits ; (b) Multi-axial warp knit insertion [4]

Knit fabrics offer higher yarn-to-fabric tensile strength translation efficiencies, greater in-plane shear resistance and better handling than comparable wovens. The process of knitting can also be used to provide through-thickness reinforcement in composite structures. The process, called stitching, significantly enhances damage tolerance and often represents a helpful step in the fabrication of textile structural composites. Fig. 1.5 shows

the two forms of stitching that are of interest for structural applications: the modified lock stitch and the chain stitch.

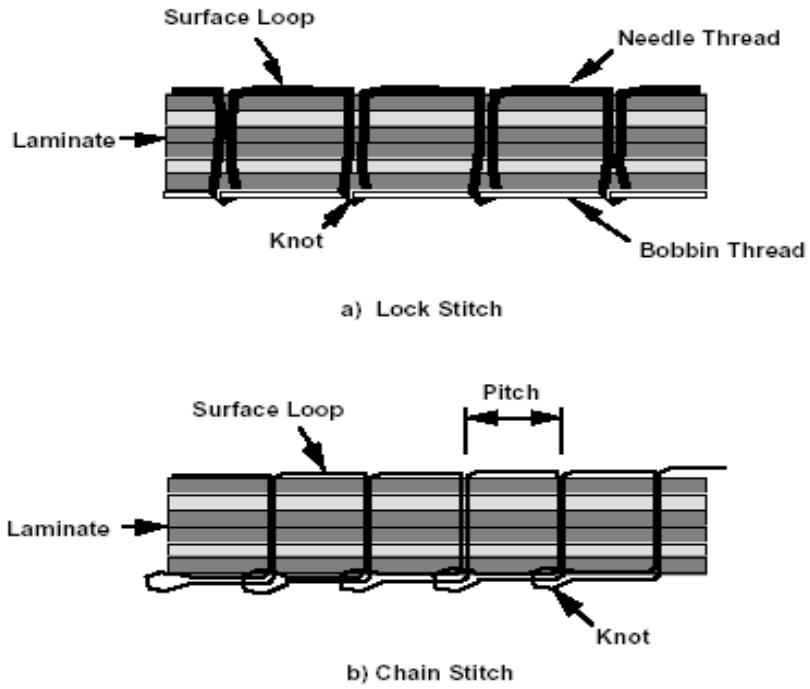

Fig. 1.5 Types of stitching used for through-thickness reinforcement [4]

Braids: Braided preforms are fabricated over a cylindrical mandrel (Fig. 1.6). Yarns are intertwined together in a spiral nature to form a tubular fabric. The braid angle is usually noted θ_b and is controlled by the rotational speed of the yarn carriers relative to the transverse speed of the mandrel. The braider yarns follow the $\pm\theta_b$ directions and usually interlace in either a 1x1 or 2x2 pattern. Triaxial braided fabrics can be designed by inserting axial yarns between the braider yarns in the longitudinal or vertical direction. Braids can be found in such composite components as masts, antennae, drive shafts and other tubular structures that require torsional strength.

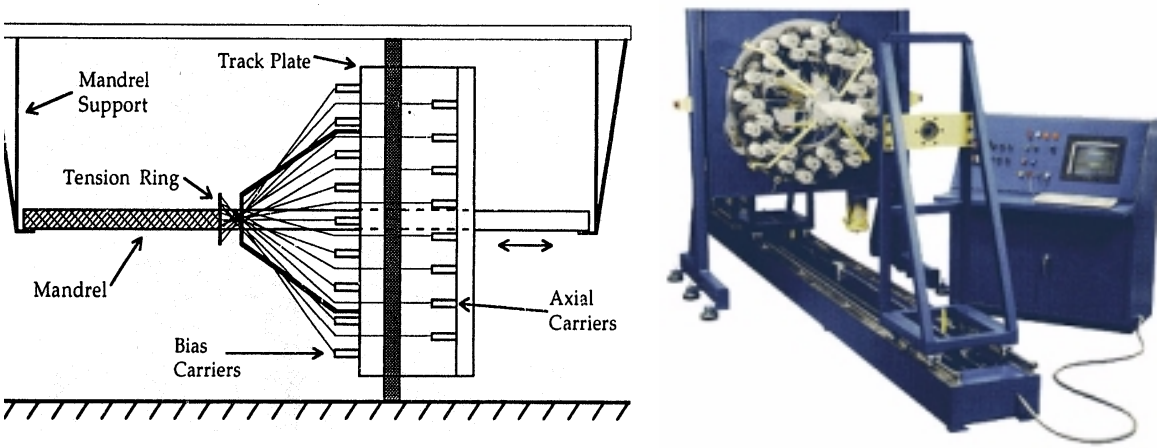

Fig. 1.6 Schematic view and photo of a cylindrical mandrel [5]

Nonwovens: Nonwoven fabrics consist of randomly bonded yarns such as fiber mats, stitch bonded, XYZ, and adhesively bonded fabrics.They are characterized by slight conformability, very short yarns and rigid entanglements. As the yarns are bonded together, these fabrics offer no substantial directional extensibility and often low in-plane shear resistance.

The fourth step of the textile composites manufacturing process consists of assembling several layers of fabrics in a laminate-like manner. The unrigidized textile dry preform is then molded to a final shape and infused with a matrix (e.g. resin transfer molding (RTM) or resin film infusion (RFI)).

Fig. 1.7 illustrates scales in one textile process. The part shown is an integrally formed skin/stiffener assembly. The first processing step is the formation of yarns from fibers. In the second step, the yarns are woven into a plain weave fabric. The cloths are then laid up in the shape of the skin and stiffener and stitched together to create an integral preform. Finally, the composite part is consolidated by the infiltration of resin and cured in a mold.

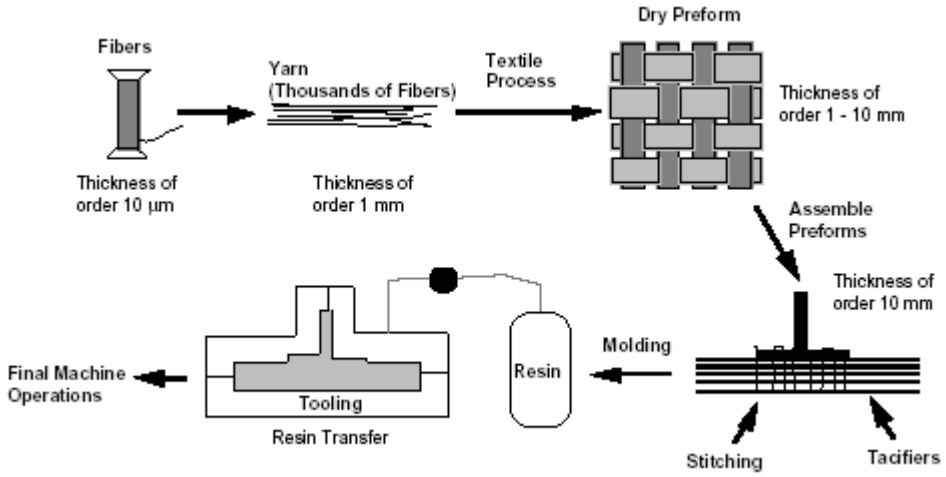

Fig. 1.7 Steps in the production of a textile composite structure [4]

As we can see, textile structural composites offer a wide range of shapes, architectures and manufacturing processes. In the choice between textile composites and conventional tape laminates, we have to weigh the advantages and disadvantages of each option in terms of weight, performances and the ease and cost of fabrication.

Textile structural composites often possess a good tailorability and good drapability. Moreover, most of the textile composite preforms can be manufactured on highly automated machines (e.g loom for woven fabrics, mandrels for 2D braids) already used in the textile industry. This allows a production at low cost and a high productivity.

In terms of mechanical properties, textile composites have interesting advantages over unidirectional laminates. Indeed, laminates made from unidirectional layers have no fibers in the thickness direction. The layers are usually prepreg tape. On the other hand, textile composites are characterized by their 3-D architecture. The interlacing yarns of most textiles either pass completely or go through the textile and give true through-the-thickness reinforcement. Compared to laminates, some textiles might have lower in-plane properties but manage to give a good balance between in-plane and out-of-plane properties.

1.3 Micromechanical Modeling of Textile Structural Composites

In order to justify the use of textile composites and because their overall mechanical properties are controlled by microscopic parameters and properties, one need to analyze these materials at this level. However, as described in the previous section, textile composites involve very complicated shapes and architectures, where two or more yarns interlace with each other. Thus only very refined models would be able to capture the complexity of these structures. Consequently, in the process of homogenizing the microscopic variations of the yarns, a large part is left to the analyst's own interpretation. This explains the diversity of geometric models for the same architecture among different authors.

One of the first attempts to model thermo-elastic behavior of two-dimensional woven fabric composites was presented by Professor Tsu-Wei Chou and Dr. Takashi Ishikawa ([6]-[8]). They developed three analytical models for 2D woven composites based on classical lamination theory (CLT): the mosaic model, the fiber crimp model and the bridging model. The mosaic model provides a convenient and rough estimate of the thermo-elastic properties of fabric composites and is discussed in more details in Chapter 2, Section 2.4 on page 58. The crimp model is suitable for plain weave fabrics and the bridging model is desirable for satin weave fabrics. As these three models are based on CLT they do not allow prediction of three-dimensional properties for a specific woven fabric, therefore, they are relatively limited, especially with respect to predicting the influence of the undulations within the fabric on the out-of-plane stiffnesses.

In Refs. [9] and [10], R.A. Naik presented a general purpose micromechanics analysis that discretely modeled the yarn architecture within representative unit cell (RUC) of the textile. This model was developed to predict overall, three dimensional, thermal and mechanical properties based on an iso-strain assumption and using a stress averaging technique [11]. The model was also implemented in a computer program called Textile Composite Analysis for Design (TEXCAD) [9] to analyze plain, 5-harness satin, 8-harness

satin woven composites along with 2D and 2x2 2D triaxial braided composites. The analytical technique, although it was based on restrictive assumptions, gave a good approximation for the overall mechanical behavior of the RUC, and allowed accurate analyses of the influence of the undulations and orientations of the yarns on the overall three-dimensional effective properties. These models [9] for the balanced plain weave fabric as well as the 2D and 2x2 2D triaxial braids are discussed in the forthcoming chapters.

N.K Naik and V.K. Ganesh [12] presented an analytical model for woven composites based on CLT that accounted for undulations in both the fill and warp directions of the yarns. They computed overall stiffness properties by assuming either iso-strain or iso-stress, or a combination of these, and analytically integrated through the volume of the RUC. They developed two models to describe the geometry of the undulating region by assuming either a circular or sinusoidal yarn path. Even though the model gives fairly accurate results to predict in-plane thermo elastic properties, the tedious analytical description of yarn cross-sectional shapes and yarn paths is not well suited for the analysis of more complicated architectures such as 2D braids and 2D triaxial braids.

In Ref. [13] D.Scida et al., used the sinusoidal model from N.K Naik to make comparisons with test data and investigate the relative accuracy of the results. Other references involve publications such as Ref. [14] where Masters, et al. investigated the unnotched tensile properties of two-dimensional triaxial braided composites from both an experimental and analytical viewpoint. They predicted linear elastic moduli for 2D triaxial braided fabrics using two different analytical models: a laminate model based on CLT, which ignored the out-of-plane undulations of the braided yarns, and a diagonal brick model, based upon the concept of a simplified unit cell representation. J-H Byun [15] also developed his own analytical model to determine three-dimensional elastic stiffness properties for 2D triaxial braided fabrics using either iso-strain or iso-stress assumption.

Various computer programs that can predict the properties of textile composites were also presented by B.N. Cox in Ref.[4], most of these programs were developed within the

Advanced Composites Technology (ACT) Program sponsored by NASA Langley Research Center.

1.4 Failure Analysis of Textile Structural Composites

Although numerous analytical and numerical techniques have been used to predict the stiffness properties of both woven and braided composites, there are only a few models that have been developed for the strength prediction of textile composites. However, some authors have developed constitutive models to predict the strength of textile composites for a specific fabric geometry. Ko and Pastore [16] used the yarn orientations to first estimate the strength of the fabric preform and then computed composite strength using a simple rule of mixture. Dow and Ramnath [17] modeled woven fabric composites using a simple geometry model that assumed a linear undulation path for the fill and warp yarns. They computed constituent fiber and matrix stresses from local stresses which were calculated using an iso-strain assumption and predicted failure based on the average stresses in the fiber and the matrix along with a maximum stress criterion.

An important characteristic of textile composites is that they also exhibit non-linear shear behavior. The earlier analysis techniques to model damage propagation and strength of textile composites often made simplifying assumptions regarding the fabric architecture and did not account for both geometric and material nonlinearities. In Ref. [18] R.A. Naik developed a general-purpose analysis technique for the prediction of failure initiation, damage progression and strength of 2D woven and braided composite materials, including the effects of non linear shear response and nonlinear material response. R.A. Naik predicted failure within the RUC by discretizing the yarns into slices, averaging the stresses over the volume of the RUC to get the overall stiffness matrix and using the cumulative stresses in each yarn slice, together with appropriate failure criteria, to predict failure at each step of the incremental analysis. He further developed a progressive damage model

by using either a stress reduction scheme or a cracked yarn bending model to account for the change in yarn compliance.

1.5 Goal of Present Study

The first part of the project consist in developing constitutive models of specific textile composite materials - presently plain weave, 2D braid, 2x2 2D triaxial braid and 4x4 twill - at different length scales, and to implement them into a Fortran program. These are numerical constitutive models which approximate the mechanical behavior at the local scale. The parameters in the models are material and scale dependent. They are defined by the user as inputs to the Fortran programs which return numerical values for the RUC effective properties. The geometric models are mostly based on the work of R.A. Naik [9], however the validity and limitations of each model will be studied carefully and in some cases some modifications will be carried out to extend the range of applications.

The implementation of these various models into Fortran programs will allow us to develop user-defined subroutines called UMAT in order to use the constitutive models in the ABAQUS[1] structural analysis software system. These UMAT subroutines provide the capability to combine a new material model with the powerful numerical algorithms for structural analysis available in ABAQUS.

The last part of the project consist of developing a progressive failure analysis model for a balanced plain weave fabric and implementing this model into the UMAT. The resulting analysis technique may then be used to calculate overall load-displacement response of, and damage progressions in, a textile material coupon configuration under a simple loading.

1. ABAQUS is registered trademark of Hibbitt, Karlsson & Sorensen, Inc.

It is important to emphasize the need for these numerical constitutive models and their implementation in the Fortran language, as they allow to predict the material response of textile composites within ABAQUS procedures, while TEXCAD [9], for example, is a stand-alone finite element software that can not be combined with ABAQUS and which requires a specific license. There is truly a demand to implement these constitutive models in the ABAQUS system and this is an important purpose of this project.

Chapter 2. Balanced Plain Weave Fabric

2.1 Description

A plain weave fabric consists of orthogonal interlaced yarns, called warp and fill yarns, produced by the process of weaving. The warp and fill yarns interlace in a regular sequence of one under and one over. Although the plain weave is the simplest form of fabric structure, it has a relatively large portion of its volume in the unit cell containing yarn undulations compared to satin weaves for example. Consequently, one can expect that the effective moduli of a plain weave are more sensitive to the undulations of the yarns than they are for satin weaves. Moreover, the rather high frequency of undulating portions within the fabric allows us to predict that this particular woven fabric will potentially exhibit high out-of-plane stiffnesses and will therefore be of much interest in mechanical problems related to out-of-plane loads.

2.2 Textile Preform Architecture

Consider a balanced plain weave textile composite in which the warp and fill yarns contain the same number of filaments (or fibers), n, with all filaments having the same diameter, d_f, and with the warp and fill yarns having the same yarn packing density, p_d. Then, the cross-sectional area, A, of the yarns is given by

$$A = (\pi d_f^2/4)n/p_d \tag{2.1}$$

Eq. (2.1) can be easily verified by the reader, $\pi d_f^2/4$ being the cross-sectional area of the filaments. Also, it is assumed that the spacing between the warp yarns and fill yarns is

the same and that there is no gap between adjacent yarns. The yarn spacing is denoted by a, which is also the yarn width when there is no gap between adjacent yarns. The representative unit cell (RUC) is a rectangular parallelepiped consisting of two warp yarns interlaced with two fill yarns with resin matrix filling the remaining portion of the volume; its planform dimensions are $2a \times 2a$ and its thickness dimension is denoted by H. Fig. 2.1 shows the related notations for the planform and cross-sectional geometry of the RUC.

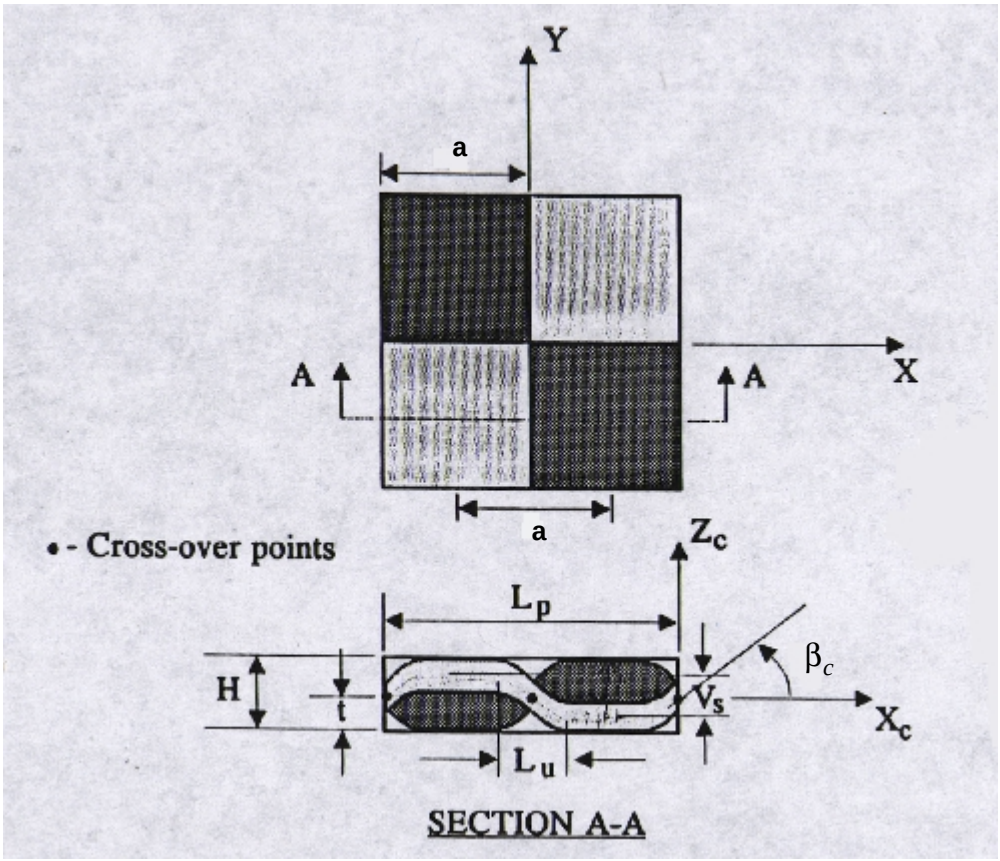

Fig. 2.1 Plain weave RUC geometry and notation[9]

Following R.A. Naik [9], the geometry of the path of either the warp or fill yarn in the RUC is modeled using two assumptions.

1. *The centerline of the yarn path consists of undulation portions and straight portions, with the centerline of the undulating portions described by the sine function.*
2. *The cross-sectional area and the thickness of the yarn normal to its centerline are uniform along the arc-length of the centerline.*

Assumption 2 does not imply that the shape of the vertical cross section (in the out-of-plane direction) is uniform along the centerline of the yarn. In the undulation region, the shape of the cross section changes while the cross-sectional area remains constant. On the other hand, we could have assumed that it is not the yarn cross-sectional area that remains constant along the path, but that its vertical cross-section remains constant. This alternate assumption would imply that the yarn cross-sectional area would have varied along the arc-length of the centerline.

The RUC is referenced to Cartesian coordinates $x - y - z$, with the x-axis in the direction of the warp yarns, the y-axis in the direction of the fill yarns, and the z-axis in the thickness direction, such that $0 \le (x, y) \le 2a$ and $-H/2 \le z \le H/2$. Let the thickness of the yarn along the centerline of the yarn path be denoted by t. If the fiber volume fraction specified for the unit cell is too small, it is necessary to add an additional resin layer of thickness t_r to the unit cell. This condition of a low relative fiber volume fraction is discussed in more detail in Section 2.2.5 on page 29. Hence, the thickness of the RUC is specified as $H = 2t + t_r$. The cross section of the RUC along the centerline of the warp yarn is shown in Fig. 2.2.

The centerline of the warp yarn path in an undulating region is specified by

$$z_w(x) = (t/2)\sin(\pi x/L_u) \qquad -L_u/2 \le x \le L_u/2 \tag{2.2}$$

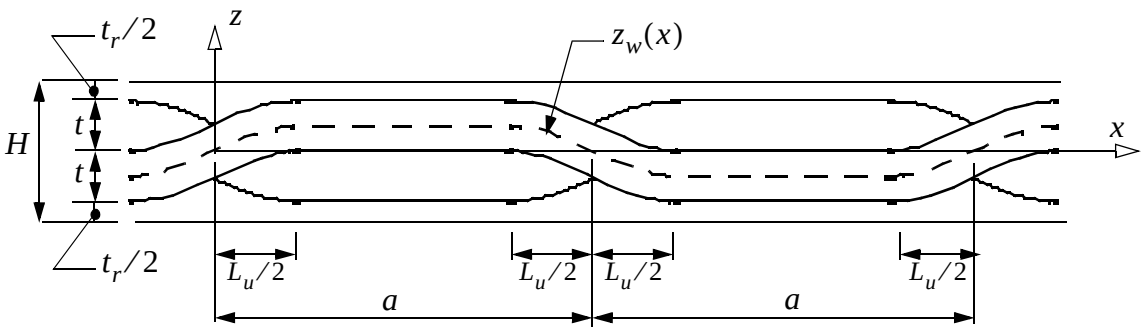

Fig. 2.2 Cross section of the RUC along the warp yarn at y = a/2

where length of the undulation region is denoted by L_u, and $x = 0$ is a crossover point. For this assumed configuration, we have the constraint that the undulation length must be less than, or equal to, the yarn width; i.e., $0 < L_u \le a$. Let β_w denote the angle between the x-axis and the tangent to the centerline. The trigonometric functions of the angle β_w in terms of function $z_w(x)$ are

$$\cos\beta_w = [1 + (z_w')^2]^{-1/2} \qquad \sin\beta_w = z_w'[1 + (z_w')^2]^{-1/2} \qquad \tan\beta_w = z_w' \quad (2.3)$$

where the prime denotes the ordinary derivative with respect to x. From Eqs. (2.2) and (2.3), the tangent of the angle β_w as function of x is

$$\tan\beta_w = \tan\beta_c \cos(\pi x / L_u) \quad (2.4)$$

where the value of β_w at the crossover point is called the crimp angle, β_c (see Fig. 2.1). The tangent of the crimp angle is defined by

$$\tan\beta_c \equiv \pi t / (2L_u) \quad (2.5)$$

2.2.1 Fiber volume fraction

The volume of the four yarns in the RUC is given by $Vol_{yarns} = 4Al$, where l denotes the arc length of one of these identical yarns. For the warp yarns the arc-length is given by

$$l = 2\int_{-L_u/2}^{L_u/2}\sqrt{1+(z_w')^2}dx + 2(a-L_u) \tag{2.6}$$

The integral in this latter equation is the arc length along the sinusoidal portion of the path. This integral can be evaluated in terms of the complete elliptic integral of the second kind, $E(m)$, where the parameter m for the sine function specified by Eq. (2.2) is determined to be

$$m = \tan^2\beta_c/(1+\tan^2\beta_c) \qquad 0 \le m \le 1 \text{ for } 0 \le \beta_c \le \pi/2 \tag{2.7}$$

The expression for the arc length of the yarns in Eq. (2.6) becomes

$$l = (4L_u/\pi)\sqrt{1+\tan^2\beta_c}E(m) + 2(a-L_u) \tag{2.8}$$

which is re-written as

$$l = 2a[1-(L_u/a)g_1(\beta_c)] \tag{2.9}$$

The function $g_1(\beta_c)$ is defined by

$$g_1(\beta_c) \equiv 1 - 2\sqrt{1+\tan^2\beta_c}E(m)/\pi \tag{2.10}$$

The volume fraction of the fibers in the RUC is given by

$$V_f = (p_d Vol_{yarns})/(4a^2H) \tag{2.11}$$

Substitute Eq. (2.9) for arc length in the equation $Vol_{yarns} = 4Al$, and then substitute this result into Eq. (2.11) to get

$$V_f = [p_d A/(tah_r)](1-(L_u/a)g_1(\beta_c)) \tag{2.12}$$

where we defined

$$h_r \equiv 1 + t_r/(2t) \tag{2.13}$$

2.2.2 Analytic geometry of the undulation region

The thickness of the yarn along its centerline is assumed to be constant. On the basis of a constant thickness normal to the centerline path, we can determine the equations of the lower and upper curves of the warp yarn in the cross section of the RUC along the undulating portion of the path. These lower and upper curves are depicted in the detail of the undulation region shown in Fig. 2.3. The parametric equations of the lower curve are:

$$x_1(x) = x + (t/2)\sin\beta_w(x) \qquad z_1(x) = z_w(x) - (t/2)\cos\beta_w(x) \tag{2.14}$$

and the parametric equations of the upper curve are:

$$x_2(x) = x - (t/2)\sin\beta_w(x) \qquad z_2(x) = z_w(x) + (t/2)\cos\beta_w(x) \tag{2.15}$$

Note that $[x_1(L_u/2), z_1(L_u/2)] = [L_u/2, 0]$ and $[x_2(L_u/2), z_2(L_u/2)] = [L_u/2, t]$.

At the crossover point of the warp yarn, $x = 0$, it assumed that there is no gap between adjacent fill yarns. That is, the tip of the cross-sectional area of the lower fill yarn contacts the warp yarn at $x_1(x_a) = 0$, and the tip of the cross-sectional area of upper fill yarn contacts the warp yarn at $x_2(x_b) = 0$. Using Eqs. (2.2) to (2.5) and setting $x_1(x_a) = 0$ in the first of Eqs. (2.14), it can be shown that the value of x_a is the root of the transcendental equation

$$\phi_a + (\tan^2\beta_c\cos\phi_a)/(\sqrt{1+\tan^2\beta_c\cos^2\phi_a}) = 0 \tag{2.16}$$

where $\phi_a \equiv \pi x_a / L_u$. A similar equation to Eq. (2.16) results for x_b from setting $x_2(x_b) = 0$ in the first of Eqs. (2.15), except for the sign of the second term in Eq. (2.16). So, we find $x_b = -x_a$. See Fig. 2.3. In the numerical algorithms described below, the solution of Eq. (2.16) for a specified crimp angle β_c is determined by the Newton-Raphson method with an initial guess of $\phi_a = -\pi/2$.

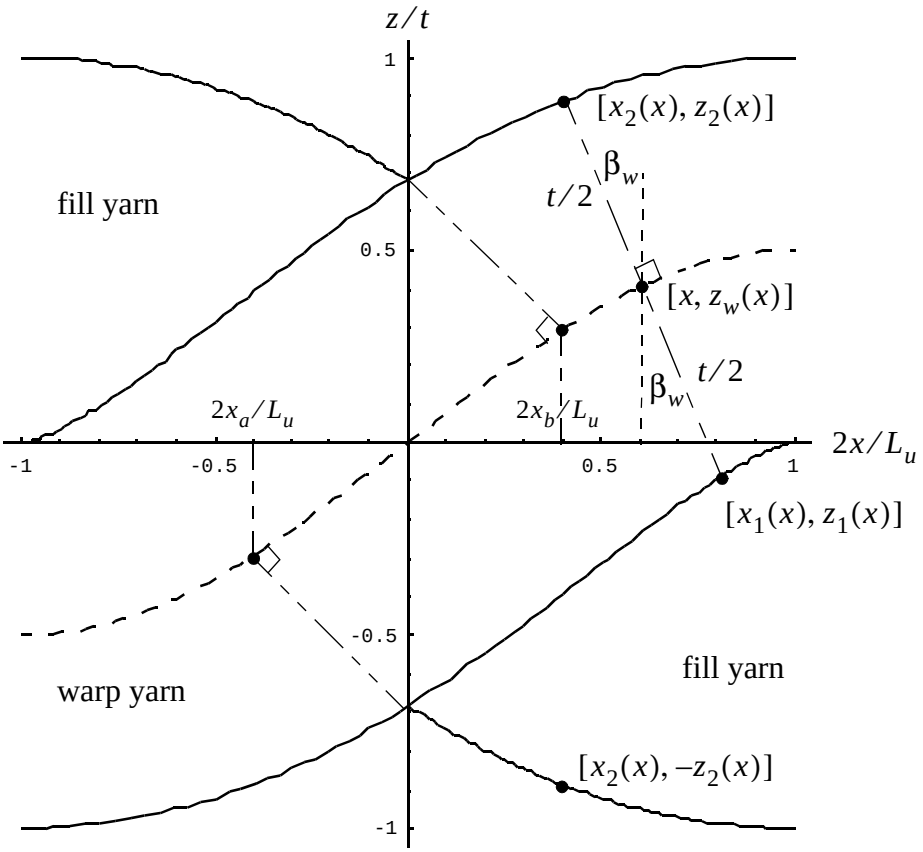

Fig. 2.3 Geometry of an undulation region along the warp yarn

The slope of the lower curve along the warp yarn is given by dz_1/dx_1. Differentiating Eqs. (2.14) with respect to x, and using Eqs. (2.3), it can be shown that

$$dx_1 = [1 + t\kappa(x)/2]dx \qquad dz_1 = z_w'[1 + t\kappa(x)/2]dx \tag{2.17}$$

where $\kappa(x)$ is the curvature of the centerline in the x-z plane. This curvature is given by

$$\kappa(x) = (z_w'')/[1 + (z_w')^2]^{3/2} \tag{2.18}$$

Hence, we conclude from Eqs. (2.17) that the slope of the lower curve is

$$\frac{dz_1}{dx_1} = z_w' \tag{2.19}$$

The curvature of the lower curve, $\kappa_1(x)$, is defined by

$$\kappa_1(x) = \frac{d^2 z_1}{dx_1^2} \Big/ \left[1 + \left(\frac{dz_1}{dx_1} \right)^2 \right]^{3/2} \tag{2.20}$$

Differentiating Eq. (2.19) with respect to x_1, using the chain rule, using Eq. (2.19) again, and then using the first of Eqs. (2.17), the second derivative in Eq. (2.20) is evaluated as

$$\frac{d^2 z_1}{dx_1^2} = \frac{d}{dx_1}\left(\frac{dz_1}{dx_1} \right) = \frac{d}{dx}(z_w')\frac{dx}{dx_1} = (z_w'')/(1 + t\kappa(x)/2) \tag{2.21}$$

Hence, the curvature of the lower curve is obtained by substituting Eq. (2.19) and the last result in Eq. (2.21) into Eq. (2.20) to get

$$\kappa_1(x) = \kappa(x)/[1 + t\kappa(x)/2] \tag{2.22}$$

Equation (2.22) shows that the curvature of the lower curve is related to the curvature of the centerline and the yarn thickness. The curvature of the lower curve is singular, which means a cusp forms in the lower curve, when the denominator of Eq. (2.22) vanishes. For the centerline defined by the sine function, the denominator in Eq. (2.22) evaluates as

$$1 + t\kappa(x)/2 = 1 - \tan^2\beta_c \sin(\pi x/L_u)/[1 + \tan^2\beta_c \cos^2(\pi x/L_u)]^{3/2} \tag{2.23}$$

When $x = L_u/2$, Eq. (2.23) is positive for $0 \le \beta_c < \pi/4$, and vanishes for $\beta_c = \pi/4$. Setting Eq. (2.23) equal to zero, and investigating the roots x for various values of β_c we found

1. *No real root in the range* $0 \le x < L_u/2$ *if* $0 \le \beta_c < \pi/4$,
2. *One real root at* $x = L_u/2$ *if* $\beta_c = \pi/4$,
3. *One real root in the range* $0.62 < x/(L_u/2) < 1$ *if* $\pi/4 < \beta_c < \pi/2$.

Hence, if the filament on the concave side of the yarn does not have a cusp, or discontinuous slope, then the value of the crimp angle is limited to the range $0 \le \beta_c < \pi/4$. If $\beta_c = \pi/4$, then a cusp forms in the lower filament on the concave side of the yarn at the end of the undulation region where $x = L_u/2$. For $\pi/4 < \beta_c < \pi/2$ a cusp forms in the lower filament in a region close to the end of the undulating region. As a result of the cusp, some fibers inside the yarn might be damaged and the model is no longer valid. Thus, the model applies only for a range of crimp angle such that $0 \le \beta_c \le (\pi/4)$.

2.2.3 Cross-sectional shape of the yarn

The shape of the cross-sectional area of the fill yarns in the undulating region is shown in Fig. 2.3. Let the cross-sectional area of the tip of the fill yarns in the undulating region be denoted by A_{tip}, and this area is determined by integration using the functions given in Eqs. (2.14) to (2.16). That is, for the lower fill yarn shown in Fig. 2.3 we have

$$A_{tip} = \int_0^{L_u/2} [z_1 - (-t)]dx_1 - \int_0^{L_u/2} [-z_2 - (-t)]dx_2 = \int_0^{L_u/2} z_1 dx_1 + \int_0^{L_u/2} z_2 dx_2 \qquad (2.24)$$

Since coordinates of the curves are given parametrically in terms of x, the latter equation becomes

$$A_{tip} = \int_{x_a}^{L_u/2} z_1(x)\frac{dx_1}{dx}dx + \int_{x_b}^{L_u/2} z_2(x)\frac{dx_2}{dx}dx \tag{2.25}$$

The integrations in this equation are carried out in Appendix A, and the final result is

$$A_{tip} = \{tL_u G_2[\phi_a(\beta_c), \beta_c]\}/(2\pi) \tag{2.26}$$

where the transcendental function of the crimp angle, $G_2[\phi_a(\beta_c), \beta_c]$, is given by Eqs. (A.6) to (A.13). Now the cross-sectional area of the fill yarn, which is the same as the warp yarn, is

$$A = 2A_{tip} + t(a - L_u) \qquad 0 \le L_u \le a \tag{2.27}$$

Substituting Eq. (2.26) for A_{tip} in this last equation and rearranging terms we get

$$A = at[1 - (L_u/a)g_2(\beta_c)] \tag{2.28}$$

where

$$g_2(\beta_c) = 1 - G_2[\phi_a(\beta_c), \beta_c]/\pi \tag{2.29}$$

Equation (2.28) relates the cross-sectional area of the yarn to its shape. Substituting Eq. (2.28) for A in Eq. (2.12), we can rearrange the result as a quadratic equation in the ratio of L_u/a; i.e.,

$$g_1 g_2 (L_u/a)^2 - (g_1 + g_2)(L_u/a) + 1 - (V_f h_r)/p_d = 0 \tag{2.30}$$

Equation (2.30) is used in the iterative procedure to determine parameters L_u and t that is described in Section 2.2.6 on page 32.

2.2.4 Small crimp angle approximations

Assume that $0 \le \beta_c^2 \ll 1$, and obtain approximations to the volume fraction equation, Eq. (2.12), and the yarn shape equation, Eq. (2.28). We neglect terms of order β_c^2 and higher in the expansions to get the final results.

The series expansion of function g_1 in Eq. (2.10) for small crimp angles is

$$g_1(\beta_c) = -\frac{1}{4}\beta_c^2 - \frac{23}{192}\beta_c^4 + O[\beta_c]^5 \tag{2.31}$$

The series expansion of Eq. (2.16) is

$$\phi_a + (\cos\phi_a)\beta_c^2 + O[\beta_c]^4 = 0$$

Neglecting terms β_c^4 and higher, the approximation to the lowest root is

$$\phi_a = -\beta_c^2 + O[\beta_c]^3 \tag{2.32}$$

Neglecting terms β_c^2 and higher means that the approximation to the lowest root is $\phi_a = 0$. Now the series expansion of function g_2 in Eq. (2.29) for $\phi_a = 0$ is

$$g_2 = \left(1 - \frac{2}{\pi}\right) - \frac{2}{\pi}\beta_c^2 + O(\beta_c)^5 \tag{2.33}$$

To get the expansion of the ratio L_u/a in terms of the crimp angle, substitute the expansions for functions g_1 and g_2 from Eqs. (2.31) and (2.33), respectively, into Eq. (2.30). Then let

$$L_u/a = r_0 + r_1\beta_c + r_2\beta_c^2 + \ldots \tag{2.34}$$

where $r_0, r_1, r_2, \ldots$ are independent of the crimp angle. After substituting the series expansions, Eqs. (2.31), (2.33), and (2.34), into Eq. (2.30), the resulting equation is satisfied by requiring each "coefficient" of a power of β_c to vanish. This process leads to

$$r_0 = \frac{\pi(1 - V_f h_r/p_d)}{(\pi - 2)} \qquad r_1 = 0 \qquad r_2 = \frac{(8 + \pi + 2r_0 - \pi r_0)\, r_0}{4(\pi - 2)} \tag{2.35}$$

Therefore, the series expansion of the ratio of the undulation length to the yarn spacing is

$$(L_u/a) = (1 - V_f h_r/p_d)(1 - 2/\pi)^{-1} + O[\beta_c]^2 \tag{2.36}$$

Neglecting terms of β_c^2 and higher, we see that the undulation length is independent of the crimp angle. The series expansion of the fiber volume fraction equation, Eq. (2.12) becomes

$$V_f = [p_d A/(tah_r)]\{1 - r_0 O[\beta_c]^2\} \tag{2.37}$$

The expansion of the equation for the cross-sectional shape of the yarn, Eq. (2.28) becomes

$$A = at\left[1 - r_0\left(1 - \frac{2}{\pi}\right) + O[\beta_c]^2\right] \tag{2.38}$$

For $0 < \beta_c^2 \ll 1$, and then neglecting terms of β_c^2 and higher in the volume fraction equation, the equation for the cross-sectional shape of the yarn, and the equation for the undulation length, gives the following approximations

$$V_f = p_d A/tah_r \qquad A = at\left[1 - \left(\frac{L_u}{a}\right)(1 - 2/\pi)\right] \qquad \frac{L_u}{a} = \frac{(1 - V_f h_r/p_d)}{\left(1 - \frac{2}{\pi}\right)} \tag{2.39}$$

Equations (2.39) are the same as those given in Ref. [1] if $h_r = 1$.

2.2.5 Limiting condition on fiber volume fraction and yarn packing density

From the small crimp angle approximations, the third of Eqs. (2.39), the ratio of the undulation length to the yarn spacing is approximated by

$$L_u/a \;=\; (1 - V_f h_r/p_d)(1 - 2/\pi)^{-1}$$

Recall that the undulation length cannot be negative nor exceed the yarn width, so $0 \le L_u/a \le 1$. We get the following limit from this equation

$$1 \ge V_f h_r/p_d \ge 2/\pi = 0.636620 \qquad \text{for } 0 \le \beta_c^2 \ll 1 \tag{2.40}$$

Equation (2.40) imposes a permissible range of values for the ratio $V_f h_r/p_d$ in the RUC for very small crimp angles.

For large crimp angles, solve the quadratic equation, Eq. (2.30), for the ratio of L_u/a to get

$$L_u/a \;=\; \frac{g_1 + g_2 \pm \sqrt{(g_1 - g_2)^2 + 4g_1g_2(V_f h_r/p_d)}}{2g_1g_2} \tag{2.41}$$

The functions g_1 and g_2 evaluated in the range of $0 \le \beta_c \le \pi/4$ were found to be of opposite sign with $g_1 < 0$ and $g_2 > 0$, and also that $|g_1| < |g_2|$. These relationships can easily be verified for the small crimp angle approximations, Eqs. (2.31) and (2.33). Hence, the unique positive root of Eq. (2.41) is

$$L_u/a \;=\; \frac{g_1 + g_2 - \sqrt{(g_1 - g_2)^2 + 4g_1g_2(V_f h_r/p_d)}}{2g_1g_2} \tag{2.42}$$

Substituting L_u/a from Eq. (2.42) in the inequality $0 \le L_u/a \le 1$, then multiplying this result by the negative product g_1g_2 leads to

$$0 \geq g_1 + g_2 - \sqrt{(g_1 - g_2)^2 + 4g_1g_2(V_f h_r / p_d)} \geq 2g_1g_2$$

Subtracting $g_1 + g_2$ from each side of this last inequality, followed by squaring the results gives

$$(g_1 + g_2)^2 \leq (g_1 - g_2)^2 + 4g_1g_2(V_f h_r / p_d) \leq (2g_1g_2 - (g_1 + g_2))^2$$

Now subtract $(g_1 - g_2)^2$ from each side of this inequality and perform some algebraic manipulations, to get

$$4g_1g_2 \leq 4g_1g_2(V_f h_r / p_d) \leq 4g_1g_2(g_1g_2 - (g_1 + g_2) + 1) \tag{2.43}$$

Finally, divide by the negative product $4g_1g_2$ to get

$$1 \geq V_f h_r / p_d \geq g_1g_2 - g_1 - g_2 + 1 \tag{2.44}$$

The right-hand side of this inequality is a function of the crimp angle only, and it is plotted in Fig. 2.4 as the curve labeled $L_u / a = 1$, for various values of β_c. The inequality (2.44) divides feasible and infeasible values of the ratio $V_f h_r / p_d$ as a function of the crimp angle. For $\beta_c = 0$, $1 \geq V_f h_r / p_d \geq 0.636620$, while for $\beta_c = \pi / 4$, $1 \geq V_f h_r / p_d \geq 0.697982$. The maximum value of the ratio $(V_f h_r / p_d)_{max} = 1$ corresponds to setting ratio $L_u / a = 0$ in Eq. (2.30), and the minimum value of the ratio $(V_f h_r / p_d)_{min} = g_1g_2 - g_1 - g_2 + 1$ corresponds to setting ratio $L_u / a = 1$ in Eq. (2.30). Therefore, intermediate values of the ratio $V_f h_r / p_d$ as a function of the crimp angle can be obtained from Eq. (2.30) by selecting a value of L_u / a in the range from zero to one. Curves for intermediate values of the ratio $V_f h_r / p_d$ are plotted in Fig. 2.4 for $L_u / a = 0.2, 0.4, 0.6, 0.8$.

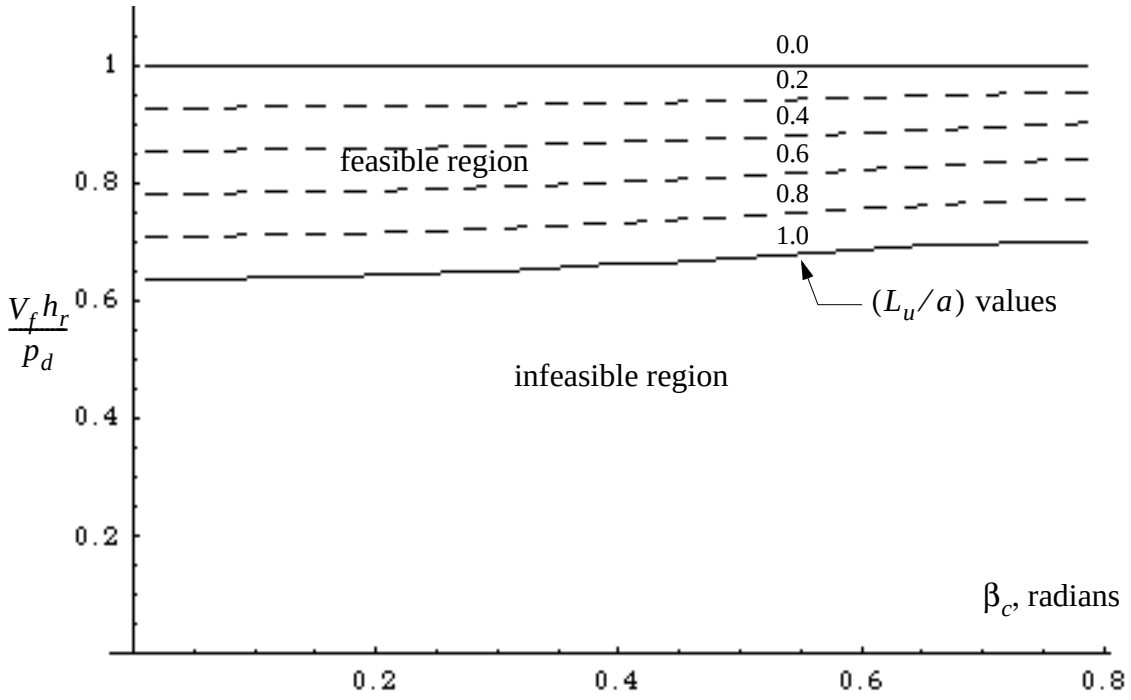

Fig. 2.4 Feasible values for the ratio of the fiber volume fraction to the yarn packing density as a function of the crimp angle

If the ratio of V_f/p_d lies in the feasible region of Fig. 2.4 then no resin needs to be added; so $t_r = 0$ and $h_r = 1$. If the ratio of V_f/p_d lies in the infeasible region of Fig. 2.4, then resin needs to be added to the RUC. That is, from inequality (2.44) we need to determine a value of $h_r > 1$ such that

$$(p_d/V_f) \geq h_r \geq (p_d/V_f)(g_1 g_2 - g_1 - g_2 + 1) \tag{2.45}$$

Selecting a value of h_r within the range defined by inequality (2.45) implies that the ratio L_u/a ranges from zero, when h_r is equal to its maximum value, to one, when h_r is equal to its minimum value. We chose to set h_r equal to its minimum value such that a minimum amount of additional resin is added to the RUC. Hence, for the case when the ratio V_f/p_d lies in the infeasible region of Fig. 2.4, we selected:

$$h_r = (h_r)_{min} = (p_d/V_f)(g_1 g_2 - g_1 - g_2 + 1) \tag{2.46}$$

which implies that $L_u = a$. Then, the thickness of the additional resin is determined by

$$t_r = 2t(h_r - 1). \tag{2.47}$$

2.2.6 Algorithm to determine the architecture parameters

The nonlinear equations describing the preform architecture are solved using an iterative procedure programmed in the FORTRAN language. The FORTRAN subroutine associated with these equations is called GEOMET. The input parameters for the GEOMET subroutine are listed in Table 2.1, and the output parameters are listed in Table 2.2.

Table 2.1: Input variables for subroutine GEOMET

Variable	Description
n	number of filaments in a yarn
d_f	diameter of a filament
p_d	yarn packing density
a	yarn spacing; also the half width of the RUC
V_f	fiber volume fraction of the RUC
TOL	tolerance on successive iterates of the crimp angle
$imax$	maximum number of iterations

Table 2.2: Output variables for subroutine GEOMET

Variable	Description
t	yarn thickness
L_u	length of the undulation region
β_c	crimp angle
t_r	thickness of additional resin layer
$newa$	new yarn spacing; only if $\beta_c = 45°$
V_{yarn}	volume of the yarns in one quarter of the RUC
Vol	volume of one quarter of the RUC
Vol_r	volume of the resin in one quarter of the RUC

An algorithm is developed to determine the yarn thickness t, undulation length L_u, and the thickness of additional resin, t_r, if any. To satisfy the fiber volume fraction equation, Eq. (2.12), and the yarn shape equation, Eq. (2.28), this algorithm is based on fixed point iteration for the yarn thickness t and undulation length L_u. These equations for volume fraction and yarn shape are combine into one equation, Eq. (2.30), to effect the procedure. There are limits on values of the thickness t and undulation length L_u that are imposed by the conditions that $0 < L_u \le a$ and $0 \le \beta_c \le \pi/4$. The algorithm is as follows:

1. *Compute the cross-sectional area of the yarn from Eq. (2.1), and from the small crimp angle equations, Eqs. (2.39), compute the initial values of the thickness t and undulation length L_u. The initial crimp angle $(\beta_c)_0$ is computed from Eq. (2.5).*

2. *Begin iteration loop: For $i = 1$ to $imax$ in steps of one.*

   2.a Set $t_r = 0$, or $h_r = 1$, and for the crimp angle $(\beta_c)_{i-1}$ solve the quadratic equation, Eq. (30), for the two roots of the ratio L_u/a.

2.b If no positive real root L_u/a exists, then STOP the program and issue a warning message.

2.c Take the smallest positive real root, and multiply the root by the yarn spacing a to get a new value of the undulation length L_u.

2.d If $0 < L_u \leq a$, then go to step 2.f.

2.e If $L_u > a$, then set $L_u = a$ and solve Eq. (2.30) for h_r. Go to step 2.f.
(See Section 2.2.5 on page 29. for a discussion of this condition)

2.f Determine a new thickness t from the fiber volume fraction equation, Eq. (2.12).

2.g Calculate a new crimp angle $(\beta_c)_i$ from Eq. (2.5) using the new L_u and t determined in steps 2.c to 2.f.

2.h Calculate the difference in the iterates using the measure $\varepsilon = \left|(\beta_c)_i - (\beta_c)_{i-1}\right|$

2.i If $\varepsilon > TOL$, then increase the index $i \rightarrow i + 1$.

2.j If $i \leq imax$, then go to step 2.a.

2.k If $i > imax$, then STOP and print non-convergence message.

2.l If $\varepsilon < TOL$, then the fixed point iteration is judged to have converged to the crimp angle $\beta_c = (\beta_c)_i$, with the thickness t, and the undulation length L_u, satisfying Eqs. (2.5), (2.12) and (2.28), and the constraint that $0 < L_u \leq a$. Go to step 3.

3. Check the constraint on the crimp angle.

3.a If $0 < \beta_c \leq \pi/4$, then STOP. Convergence of the geometric parameters t, L_u, and t_r has been achieved and the geometry of the RUC is establish.

3.b If $\beta_c > \pi/4$, then set $\beta_c = \pi/4$ and it is assumed that the specified value of the yarn spacing a is incorrect. Solve for t, L_u, t_r and a in steps 3c to 3.g.

3.c Set $t_r = 0$, or $h_r = 1$, and solve the quadratic equation, Eq. (2.30), for the two roots L_u/a. Take the positive real root for the ratio of L_u/a.

3.d *If* $0 < L_u/a \le 1$, *then go to step 3.f.*

3.e *If* $L_u/a > 1$, *then set* $L_u/a = 1$ *and solve Eq. (2.30) for* h_r. *Go to step 3.f.*

3.f *Since* $\tan\beta_c = 1$, *we determine from Eq. (2.5) that* $t = (2/\pi)(L_u/a)a$ *where the ratio* L_u/a *is known from either step 3.d or 3.e. Substitute this expression for* t *into the volume fraction equation, Eq. (2.12), and solve for the new yarn spacing* $newa$ *to get*

$$newa = \sqrt{\frac{\pi p_d A[1 - g_1(\pi/4)\cdot(L_u/a)]}{2(L_u/a)V_f h_r}}$$

3.g *For* $newa$ *from step 3.f, compute in secession* $L_u = (L_u/a)\cdot newa$, $t = (2/\pi)L_u$, *and* $t_r = 2t(h_r - 1)$. *This completes the geometry of the RUC for the maximum crimp angle.*

2.2.7 Example from R.A. Naik

Take the following values of the balanced plain weave from Ref. [9]: $V_f = 0.64$, $d_f = 0.007$ mm, $a = 1.411$ mm, and $p_d = 0.75$. The subroutine GEOMET of the Fortran program described in Appendix C was executed for $TOL = \pi/4\times10^{-6}$ and $I_{max} = 30$. For the number of filaments $n = 2000$ to 14000, in steps of 2000, the geometric parameters t, L_u, and t_r were determined from the subroutine. For these input values no additional resin layer was required, so $t_r = 0$ for all values of n considered.

In Ref. [9], the values of t and L_u are determined from equations that are the same as Eqs. (2.39) presented here. The results computed in the present work and those results determined by the equations from Ref. [9] are given in Table 2.3. As was shown for the small crimp angle approximations, Eqs. (2.39), the undulation length is independent of the

of n and is equal to 0.5695 mm for these examples. Also, the maximum value of the crimp angle is violated for $n \geq 12000$ using the small crimp angle equations. In general, the undulation lengths computed from the present analysis are longer if $0 \leq \beta_c \leq \pi/4$, and the crimp angles are smaller, than those computed from the equations of Ref. [9]. As determined from the present analysis, properly scaled cross sections of the RUC along the warp yarn for several values of n are depicted in Fig. 2.5. For $n = 15000$ the Newton-Raphson method failed to converge to a root for ϕ_a in Eq. (2.16), so results for $n \geq 15000$ are not available.

Table 2.3: Preform architectures for an increasing number of yarn filaments

n	a, mm[a]	t, mm		L_u, mm[b]	β_c, degrees		No. of iterations
		present	Ref. [9]		present	Ref. [9]	
2000	1.411	0.0857	0.0852	0.5869	12.9	13.2	4
4000	1.411	0.1739	0.1705	0.6297	23.5	25.2	7
6000	1.411	0.2666	0.2557	0.6826	31.53	35.19	9
8000	1.411	0.3655	0.3409	0.7356	37.97	43.24	8
10000	1.411	0.4727	0.4262	0.7812	43.54	49.61	6
12000	1.5055[c]	0.5373	0.5114	0.8441	45.00[c]	54.66	9
14000	1.6260[c]	0.5804	0.5966	0.9117	45.00[c]	58.71	23

a. In Ref. [9] the yarn spacing a is 1.411mm for all values of n.
b. In Ref. [9] the undulation length is 0.5695 mm for all values of n.
c. A maximum crimp angle condition.The yarn spacing a is re-computed.

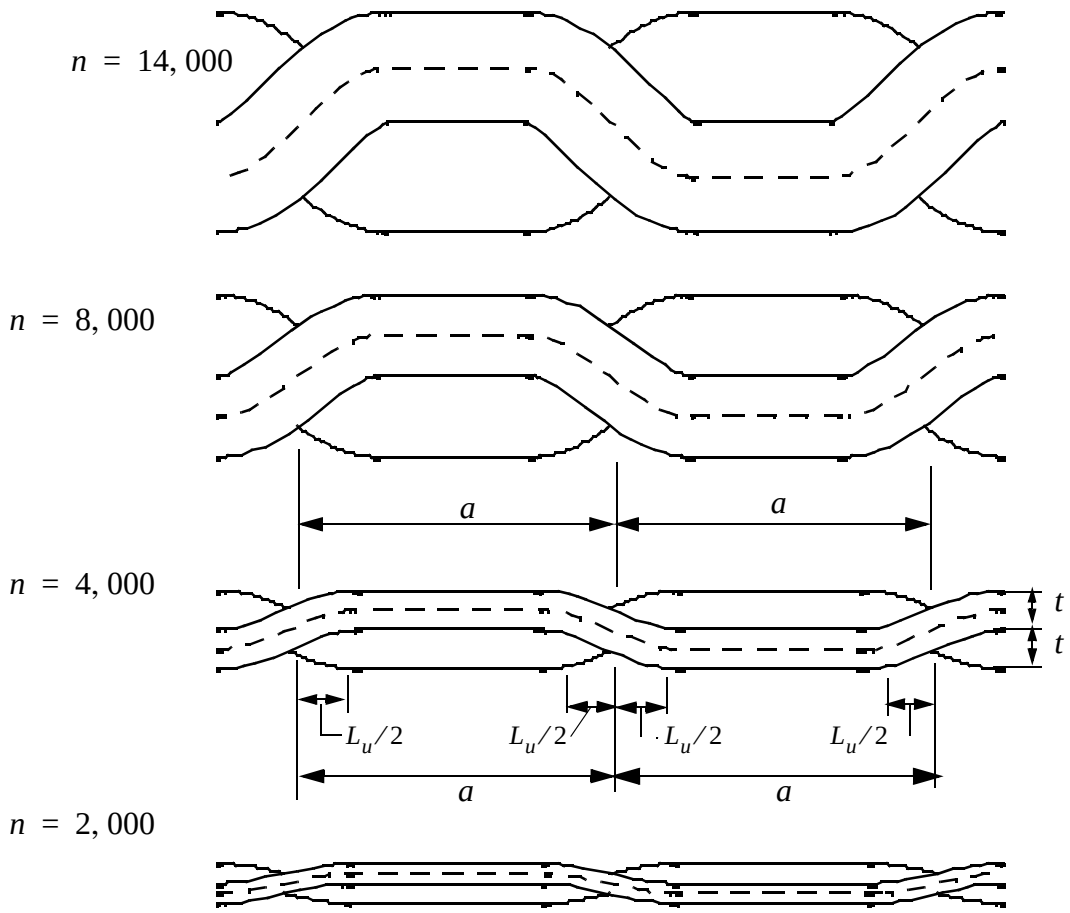

Fig. 2.5 Cross sections of a balanced plain weave preform for various number of yarn filaments n. Yarn packing density $p_d = 0{,}75$, unit cell fiber volume fraction $V_f = 0{,}64$, and filament diameter $d_f = 0{,}007$ mm.

2.3 Effective Moduli of the RUC

2.3.1 Iso-strain assumption

The RUC is assumed to be composed of three linear elastic phases: two warp yarns, two fill yarns, and resin matrix. In general, the strain energy of a linear elastic solid is

$$U = \frac{1}{2}\int_V \varepsilon^T C \varepsilon dV \tag{2.48}$$

where in this case the volume is that of the RUC, or $V = 4a^2H$, the engineering strain vector is specified by

$$\varepsilon^T = \left[\varepsilon_x \ \varepsilon_y \ \varepsilon_z \ \gamma_{yz} \ \gamma_{zx} \ \gamma_{xy}\right] \tag{2.49}$$

and C is the six-by-six, symmetric elasticity matrix. Homogenization of the RUC to determine its effective moduli is based on the iso-strain assumption; i.e., the strains are spatially uniform. By this iso-strain assumption, the strain vectors can be taken out of the integrand of Eq. (2.48) and the strain energy can be written in the form

$$U = \frac{V}{2}\varepsilon^T C_{eq} \varepsilon \tag{2.50}$$

where the equivalent elasticity matrix for the RUC is defined by

$$C_{eq} \equiv \frac{1}{V}\int_V C dV. \tag{2.51}$$

The volume of the RUC is subdivided into the volume of the two warp yarns, $2Al$, the two fill yarns, $2Al$, and the volume of the resin matrix, $V_{\text{resin}} = V - 4Al$. The equivalent elasticity matrix is, then, the sum of the volume integral of the elasticity matrices over each phase. That is,

$$C_{eq} = \frac{1}{V}\left\{ \int_{V_{\text{warp}}} C_{\text{warp}}\,dV + \int_{V_{\text{fill}}} C_{\text{fill}}\,dV + \int_{V_{\text{resin}}} C_{\text{resin}}\,dV \right\} \tag{2.52}$$

This equation is re-written in the form

$$C_{eq} = v_w C_{eqw} + v_f C_{eqf} + v_r C_{eqr} \tag{2.53}$$

where the volume fractions of the warp yarns, the fill yarns, and the resin are given by

$$v_w = v_f = (2Al)/V \qquad v_r = V_{\text{resin}}/V = 1 - v_w - v_f \tag{2.54}$$

The volume element of one warp yarn, under the present assumptions, is represented in terms of the differential length dx by

$$dV = A\sqrt{1 + (z_w')^2}\,dx \tag{2.55}$$

The function z_w' over one-half of the length of the warp yarn is

$$z_w' = \begin{cases} \tan\beta_c \cos(\pi x/L_u) & x \in (0, L_u/2) \\ 0 & x \in (L_u/2,\ a - L_u/2) \\ -\tan\beta_c \cos[\pi(x-a)/L_u] & x \in (a - L_u/2,\ a) \end{cases} \tag{2.56}$$

Similarly, the volume element of a fill yarn is represented in terms of the differential length dy as

$$dV = A\sqrt{1 + (z_f')^2}\,dy \tag{2.57}$$

where the function z_f' is

$$z_f' = \begin{cases} -\tan\beta_c \cos(\pi y/L_u) & y \in (0, L_u/2) \\ 0 & y \in (L_u/2,\ a - L_u/2) \\ \tan\beta_c \cos[\pi(y-a)/L_u] & y \in (a - L_u/2,\ a) \end{cases} \tag{2.58}$$

As a consequence of Eqs. (2.55) and (2.57), and that the on-axis elasticity matrix of a yarn is uniform (homogeneity), the phase equivalent elasticity matrices for the warp and fill yarns in Eq. (2.53) are expressed as line integrals rather than three-dimensional integrals. That is,

$$C_{eqw} = \frac{1}{2Al}\int_{V_{\text{warp}}} C_{\text{warp}}\,dV = \frac{1}{l}\int_{0}^{2a} C_1(0, \beta_w)\sqrt{1 + (z_w')^2}\,dx \tag{2.59}$$

$$C_{eqf} = \frac{1}{2Al}\int_{V_{\text{fill}}} C_{\text{fill}}\,dV = \frac{1}{l}\int_{0}^{2a} C_1\left(\frac{\pi}{2}, \beta_f\right)\sqrt{1 + (z_f')^2}\,dy \tag{2.60}$$

where the elasticity matrix in x-,y-,z-coordinate directions at a generic position in a yarn, either warp or fill, is denoted by $C_1(\theta, \beta)$. The six-by-six matrix $C_1(\theta, \beta)$ is derived in Appendix B and given by Eq. (B.9).The angles of the centerlines of the warp and fill yarns with respect to the x- and y-axes are, respectively, determined by

$$\beta_w = \operatorname{atan}(z_w') \qquad \beta_f = \operatorname{atan}(z_f') \tag{2.61}$$

The resin is assumed to be homogeneous and isotropic, so its equivalent elasticity matrix is equal to its elasticity matrix evaluated point-wise; i.e.,

$$C_{eqr} = \frac{1}{V_{\text{resin}}}\int_{V_{\text{resin}}} C_{\text{resin}}\,dV = C_{\text{resin}} \tag{2.62}$$

This resin elasticity matrix is given by Eq. (B.10) in Appendix B. It turns out that the equivalent elasticity matrices for the warp and fill yarns are the same if the integrations in Eqs. (2.59) and (2.60) are performed over the interval from 0 to a as for the interval of a to 2a. As a result, we can integrate over one quarter of the RUC to determine the equivalent moduli for the entire RUC. Thus,

$$C_{eqw} = \frac{2}{l}\int_0^a C_1(0, \beta_w)\sqrt{1 + (z_w')^2}\,dx \tag{2.63}$$

$$C_{eqf} = \frac{2}{l}\int_0^a C_1\left(\frac{\pi}{2}, \beta_f\right)\sqrt{1 + (z_f')^2}\,dy \tag{2.64}$$

The integrations indicated in Eqs. (2.63) and (2.64) are done numerically using the trapezoidal rule in the 'exactplainweave.f' FORTRAN program.

2.3.2 Structure of the elasticity matrices for the yarns and RUC

The elasticity matrix for the warp yarn in the global coordinate directions, or the *x*- *y*- *z* coordinate directions, is $C_1(0, \beta_w)$, and the elasticity matrix of the fill yarn in the global coordinate directions is $C_1(\pi/2, \beta_f)$. The yarns are assumed to be transversely isotropic, so that the form that these elasticity matrices take in the global coordinate directions are

$$C_1[0, \beta_w(x)] = \begin{bmatrix} \blacksquare & \blacksquare & \blacksquare & 0 & \blacksquare & 0 \\ \blacksquare & \blacksquare & \blacksquare & 0 & \blacksquare & 0 \\ \blacksquare & \blacksquare & \blacksquare & 0 & \blacksquare & 0 \\ 0 & 0 & 0 & \blacksquare & 0 & \blacksquare \\ \blacksquare & \blacksquare & \blacksquare & 0 & \blacksquare & 0 \\ 0 & 0 & 0 & \blacksquare & 0 & \blacksquare \end{bmatrix} \qquad C_1\left[\frac{\pi}{2}, \beta_f(y)\right] = \begin{bmatrix} \blacksquare & \blacksquare & \blacksquare & \blacksquare & 0 & 0 \\ \blacksquare & \blacksquare & \blacksquare & \blacksquare & 0 & 0 \\ \blacksquare & \blacksquare & \blacksquare & \blacksquare & 0 & 0 \\ \blacksquare & \blacksquare & \blacksquare & \blacksquare & 0 & 0 \\ 0 & 0 & 0 & 0 & \blacksquare & \blacksquare \\ 0 & 0 & 0 & 0 & \blacksquare & \blacksquare \end{bmatrix} \tag{2.65}$$

where the elements in the matrices indicated by filled squares denote non-zero values. The material couplings indicated in Eqs. (2.65) between shear stress and normal strains, and between shear stresses and shear strains, vanish when the integrations in Eqs. (2.63) and (2.64) are performed over the unit cell. Hence, the resulting phase equivalent elasticity matrices C_{eqw} and C_{eqf} have the same form as for an orthotropic material; i.e.,

$$C_{eqw}, C_{eqf} \rightarrow \begin{bmatrix} \blacksquare & \blacksquare & \blacksquare & 0 & 0 & 0 \\ \blacksquare & \blacksquare & \blacksquare & 0 & 0 & 0 \\ \blacksquare & \blacksquare & \blacksquare & 0 & 0 & 0 \\ 0 & 0 & 0 & \blacksquare & 0 & 0 \\ 0 & 0 & 0 & 0 & \blacksquare & 0 \\ 0 & 0 & 0 & 0 & 0 & \blacksquare \end{bmatrix} \tag{2.66}$$

For example, take the material properties for the yarn listed in Table 2.4 on page 45. From Table 2.3 on page 36, take the preform architecture data $n = 10000$, $a = 1.411$ mm, $t = 0.4727$ mm, and $L_u = 0.7812$ mm. For these data, the non-zero elements of the elasticity matrix for the warp yarn are plotted as a function of x, $0 \le x \le 2a$, in Fig. 2.6 and Fig. 2.7. The distributions of the elements $c_{51}, c_{52}, c_{53}, c_{64}$ shown in the figures suggest that integrals of them over $0 \le x \le 2a$ will vanish.

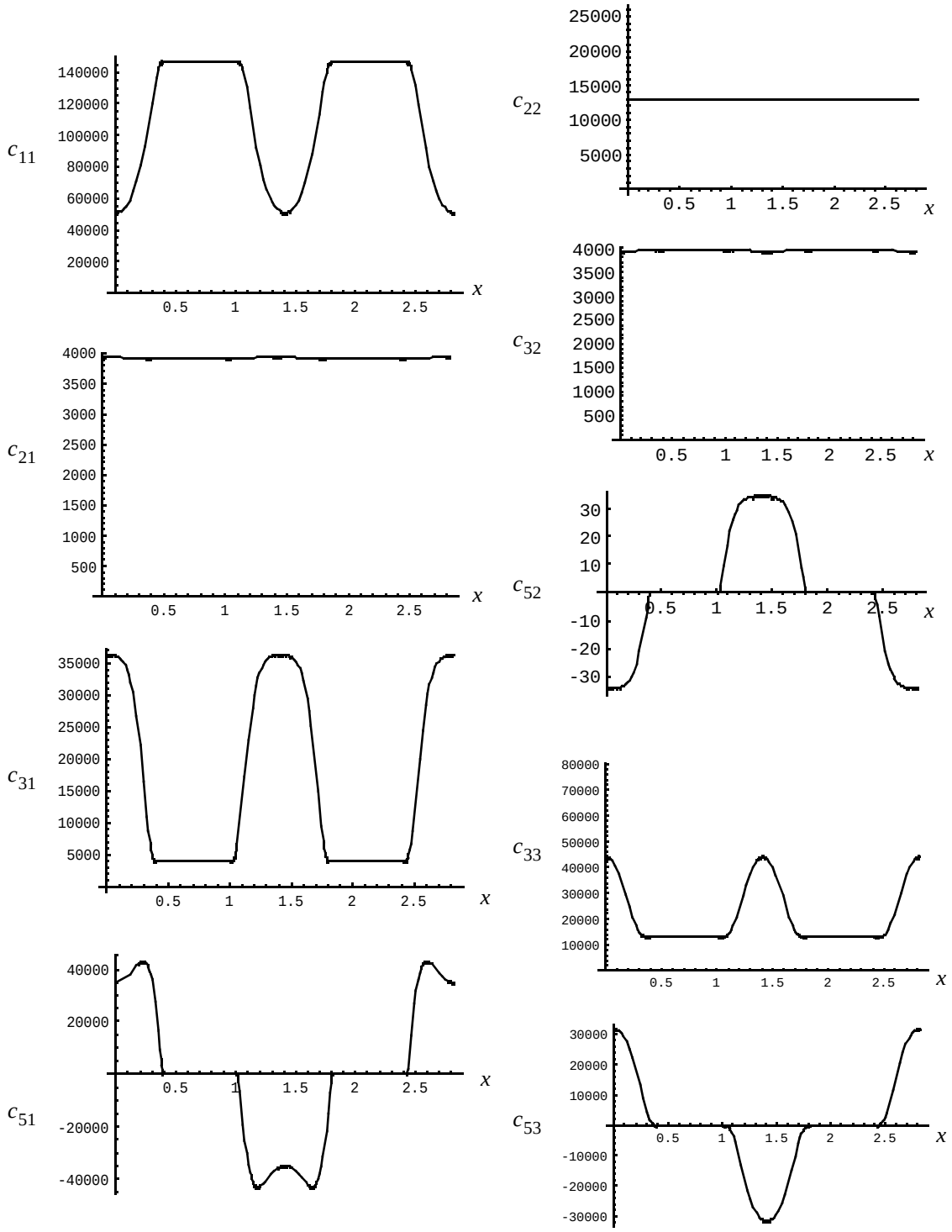

Fig. 2.6 Non-zero elements of the elasticity matrix for the warp yarn, in kPa, as a function of x, in mm. For x = 0 to x = 2a, where a = 1.411 mm

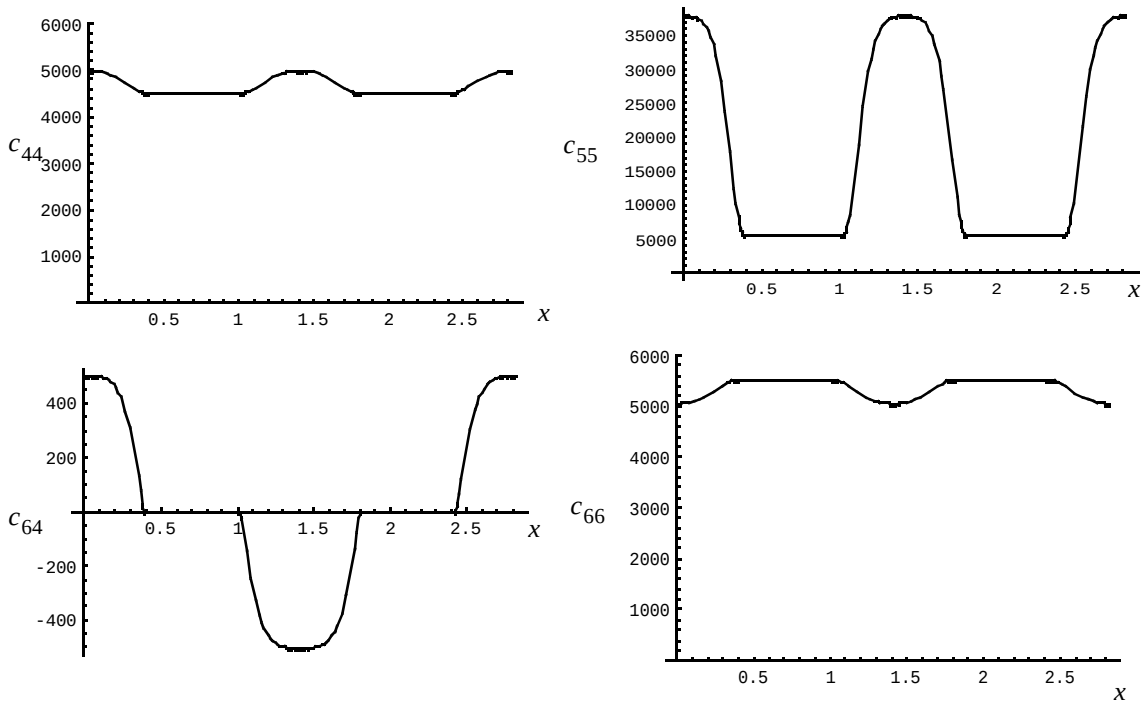

Fig. 2.7 Remaining non-zero elements of the elasticity matrix for the warp yarn, in kPa, as a function of x, in mm. For x = 0 to x = 2a, and a = 1.411 mm

2.3.3 Example from R.A. Naik

Effective moduli are computed for a plain weave example from Ref.[9], and the input geometric data for the textile preforms in this example are the same as those given in Section 2.2.7 on page 35. The output geometric data determined for the GEOMET subroutine are presented in Table 2.3 for several values of n. The yarn is transversely isotropic, and the resin is isotropic, and properties of these with materials are listed in Table 2.4.

Table 2.4: Yarn and resin properties from Ref [9].

Material	E_{11}, GPa	E_{22}, GPa	G_{12}, GPa	ν_{12}	ν_{23}
Yarn	144.80	11.73	5.52	0.23	0.30
Resin	3.45	3.45	1.28	0.35	0.35

Numerical results from the present analysis and Ref.[9] for the effective Young's moduli E_{xx}, E_{yy}, E_{zz} are listed in Table 2.5, effective shear moduli G_{yz}, G_{zx}, G_{xy} are listed in Table 2.6, and Poisson ratios ν_{xy}, ν_{xz}, ν_{yz} are listed in Table 2.7. The effective Young moduli and shear moduli are essentially the same as those in Ref. [9] for $n = 2000$. As the number of filaments in the yarns increases, the effective in-plane moduli E_{xx}, E_{yy}, G_{xy} decrease and the transverse moduli E_{zz}, G_{yz}, G_{zx} increase. The Young moduli E_{xx}, E_{yy}, E_{zz} from our analysis are, in general, less than those from the analysis of Ref. [9], but transverse shear moduli G_{yz}, G_{zx} are greater than those from Ref. [9]. There is little difference in the in-plane shear modulus from the present results and those of Ref. [9]. The in-plane Poisson ratio ν_{xy} decreases with increasing n, and the in-plane Poisson ratios from the present analysis are less than those from the analysis of Ref. [9]. Finally, the transverse Poisson ratios ν_{xz}, ν_{yz} from the present analysis are greater than those predicted from the analysis of Ref. [9], and both analyses show that ν_{xz}, ν_{yz} initially increase with n and then decrease with further increasing n. The results presented in these tables show that the present analysis compares very well with the analysis from Ref. [9] for small crimp angles, which correspond to small values of n. Discrepancies occur for larger crimp

angles, which is expected since the analysis of Ref. [9] is based on the crimp angles being small,

Table 2.5: Young moduli in GPa for the plain weave example from Ref. [9]

Number of filaments, n	Ref. [9]			Present model		
	E_{xx}	E_{yy}	E_{zz}	E_{xx}	E_{yy}	E_{zz}
2000	66.0613	66.0613	11.4495	66.0648	66.0648	11.4475
4000	62.3531	62.3531	11.6922	62.2436	62.2436	11.6091
6000	58.3916	58.3916	12.8242	57.4660	57.4660	12.4008
8000	55.3797	55.3797	14.9065	52.6202	52.6202	13.9950
10000	53.36	53.36	17.5873	48.0907	48.0907	16.5524
12000	52.0058	52.0058	20.4744	46.9379	46.9379	17.4539
14000	51.0557	51.0557	23.3026	46.9379	46.9379	17.4539

Table 2.6: Shear moduli in GPa for the plain weave example from Ref. [9]

Number of filaments, n	Ref. [9]			Present model		
	G_{yz}	G_{zx}	G_{xy}	G_{yz}	G_{zx}	G_{xy}
2000	5.0415	5.0415	4.8885	5.0405	5.0405	4.8886
4000	6.3138	6.3138	4.8648	6.3593	6.3593	4.8646
6000	7.5309	7.5309	4.8343	7.8662	7.8662	4.8313
8000	8.3328	8.3328	4.8035	9.2945	9.2945	4.7917
10000	8.7269	8.7269	4.7755	10.5318	10.5318	4.7468
12000	8.8394	8.8394	4.7513	10.8217	10.8217	4.7337
14000	8.7867	8.7867	4.7308	10.8217	10.8217	4.7337

Table 2.7: Poisson's ratios for the plain weave example from Ref. [9]

Number of filaments, *n*	Ref. [9]			Present model		
	ν_{xy}	ν_{xz}	ν_{yz}	ν_{xy}	ν_{xz}	ν_{yz}
2000	0.03292	0.35232	0.35232	0.03292	0.35231	0.35231
4000	0.02021	0.43692	0.43692	0.01937	0.44319	0.44319
6000	0.00858	0.47495	0.47495	0.01828	0.51117	0.51117
8000	0.00571	0.45162	0.45162	-0.01328	0.52910	0.52910
10000	0.01001	0.40149	0.40149	-0.02126	0.50123	0.50123
12000	0.01719	0.35018	0.35018	-0.02174	0.48726	0.48726
14000	0.02459	0.30644	0.30644	-0.02174	0.48726	0.48726

2.3.4 Example from N.K Naik and Ganesh

The second balanced plain weave example is from N.K. Naik and Ganesh [12]. The yarn spacing $a = 2.0$ mm, fiber volume fraction $V_f = 0.45$, and the packing density $p_d = 0.71$. The yarns are composed of T-300 carbon filaments and an epoxy resin whose material properties are listed in Table 2.8. The equivalent yarn properties are computed from the composite cylinder assemblage model in Ref. [12], but we used the self-consistent model to get the results shown in Table 2.9. N.K. Naik and Ganesh do not use the filament diameter or the number of filaments in the yarn in their unit cell models. Instead, for the unit cell model, they plot the effective in-plane modulus E_{xx}, effective in-plane shear modulus G_{xy}, and effective in-plane Poisson ratio ν_{xy} as a function of the ratio of the yarn thickness to one-half the width of the unit cell, t/a. For our model we specified $d_f = 0.007$ mm, varied the number of filaments in the yarn n, and then computed the ratio of t/a from the GEOMET subroutine results. In this example the ratio of the fiber

volume fraction to the packing density, $V_f / p_d = 0.6338$, violates the limiting condition given by Eq. (2.40) for small crimp angles, and also Eq. (2.44) for large crimp angles, if $h_r = 1$. Hence, it is necessary to add a resin layer to the unit cell, $h_r > 1$, and we selected the minimum value $(h_r)_{min}$ as given by Eq. (2.46). Selecting $h_r = (h_r)_{min}$ implies that there is no straight portion of the yarn along its path, or $L_u = a$. The results from the GEOMET subroutine are listed in Table 2.10.

Table 2.8: Yarn properties from Ref. [12]

Material	E_{11}, GPa	E_{22}, GPa	G_{12}, GPa	G_{23}, GPa	ν_{12}
T-300	230	40	24	14.3	0.26
Epoxy[a]	3.5	3.5	1.3	1.3	0.35

a. Isotropic

Table 2.9: T-300 carbon/epoxy effective yarn properties from the self-consistent model

E_{11}, GPa	E_{22}, GPa	G_{12}, GPa	G_{23}, GPa	ν_{12}	ν_{23}
163.3	13.5	5.85	4.6	0.28	0.46

Table 2.10: Unit cell architectures for the example from Ref. [12][a]

Number of filaments n [b]	Crimp angle β_c, degrees	Ratio t/a	Resin thickness t_r, mm
1000	1.915	0.0213	0.004
2000	3.825	0.0426	0.0009
3000	5.728	0.0638	0.0017
4000	7.6180	0.0851	0.0030
5000	9.4919	0.1064	0.0048
6000	11.3466	0.1277	0.0072
7000	13.1790	0.1491	0.0105
8000	14.9868	0.1704	0.0145
9000	16.7681	0.1918	0.0195
10000	18.5214	0.2133	0.0256
11000	20.2459	0.2348	0.0327
12000	21.9410	0.2564	0.0408

a. Unit cell half width $a = 2{,}0$ mm, and the undulation length $L_u = a$ for all values of n

b. Diameter of the filaments in the yarn assumed to be $d_f = 0{,}007$ mm.

For the unit cell, the effective Young moduli are listed in Table 2.11, the effective shear moduli in Table 2.12, and the effective Poisson's ratios are listed in Table 2.13.

Table 2.11: Effective Young moduli for the example from Ref. [12]

n	t/a	E_{xx}, GPa	E_{yy}, GPa	E_{zz}, GPa
1000	0.0213	57.9816	57.9816	12.0562
2000	0.0426	57.7588	57.7588	12.0288
3000	0.0638	57.3896	57.3896	11.9844
4000	0.0851	56.8770	56.8770	11.9247
5000	0.1064	56.2253	56.2253	11.8521
6000	0.1277	55.4404	55.4404	11.7694
7000	0.1491	54.5295	54.5295	11.6801
8000	0.1704	53.5016	53.5016	11.5879
9000	0.1918	52.3670	52.3670	11.4969
10000	0.2133	51.1378	51.1378	11.4113
11000	0.2348	49.8272	49.8272	11.3356
12000	0.2564	48.4500	48.4500	11.2742

Table 2.12: Effective shear moduli for the example from Ref. [12]

n	t/a	G_{yz}, GPa	G_{zx}, GPa	G_{xy}, GPa
1000	0.0213	3.8145	3.8145	4.1823
2000	0.0426	3.8932	3.8932	4.1809
3000	0.0638	4.0228	4.0228	4.1788
4000	0.0851	4.2009	4.2009	4.1757
5000	0.1064	4.4246	4.4246	4.1719
6000	0.1277	4.6900	4.6900	4.1672
7000	0.1491	4.9930	4.9930	4.1618
8000	0.1704	5.3289	5.3289	4.1556
9000	0.1918	5.6930	506930	4.1488
10000	0.2133	6.0805	6.0805	4.1413
11000	0.2348	6.4865	6.4865	4.1332
12000	0.2564	6.9064	6.9064	4.1245

Table 2.13: Effective Poisson ratios for the example from Ref. [12]

n	t/a	ν_{xy}	ν_{xz}	ν_{yz}
1000	0.0213	0.05026	0.43847	0.43847
2000	0.0426	0.04925	0.44440	0.44440
3000	0.0638	0.04754	0.45415	0.45415
4000	0.0851	0.04511	0.46751	0.46751
5000	0.1064	0.04192	0.48416	0.48416
6000	0.1277	0.03794	0.50372	0.50372
7000	0.1491	0.03313	0.52574	0.52574
8000	0.1704	0.02749	0.54965	0.54965
9000	0.1918	0.02101	0.57486	0.57486
10000	0.2133	0.01372	0.60069	0.60069
11000	0.2348	0.00568	0.62644	0.62644
12000	0.2564	-0.00301	0.65140	0.65140

Some of the data in the above tables can be compared to the graphical results given in Ref. [12]. A scanned image of the graph of moduli E_{xx} and E_{yy} as a function of h/a from Ref. [12] is shown in Fig. 2.8. The yarn thickness is designated by h in Ref. [12], but it is designated t in this report. The corresponding moduli from the present analysis are listed in Table 2.11. Our results compare most favorably to the Parallel-Series, 2D analysis in Ref. [12]. Our model predicts larger values of the in-plane Young moduli that do not decrease as rapidly as those shown in Fig. 2.8 for increasing values of h/a, or t/a. Refer to the present results in Table 2.11. However, our moduli predictions are within the ranges predicted by the various analyses of Ref. [12]. Note in Fig. 2.8 the notation $u/a = 0.6$, which means that $L_u/a = 0.6$ in our notation. However, for this model we have

$L_u/a = 1$, which may be the reason for the discrepancies between the present model and those from Ref. [12].

A scanned image from Ref. [12] of the plot of the in-plane Poisson ratio ν_{xy} as a function of h/a is shown in Fig. 2.9. Our predictions of the in-plane Poisson ratio is given in Table 2.13. For $t/a = 0.0213$ our result is $\nu_{xy} = 005026$, which compares well to the value on curve labeled I in Fig. 2.9. However, our predictions of the in-plane Poisson's ratio decrease with increasing values of t/a, while the analysis from Ref. [12] show an increase in the in-plane Poisson's ratio with increasing values of h/a.

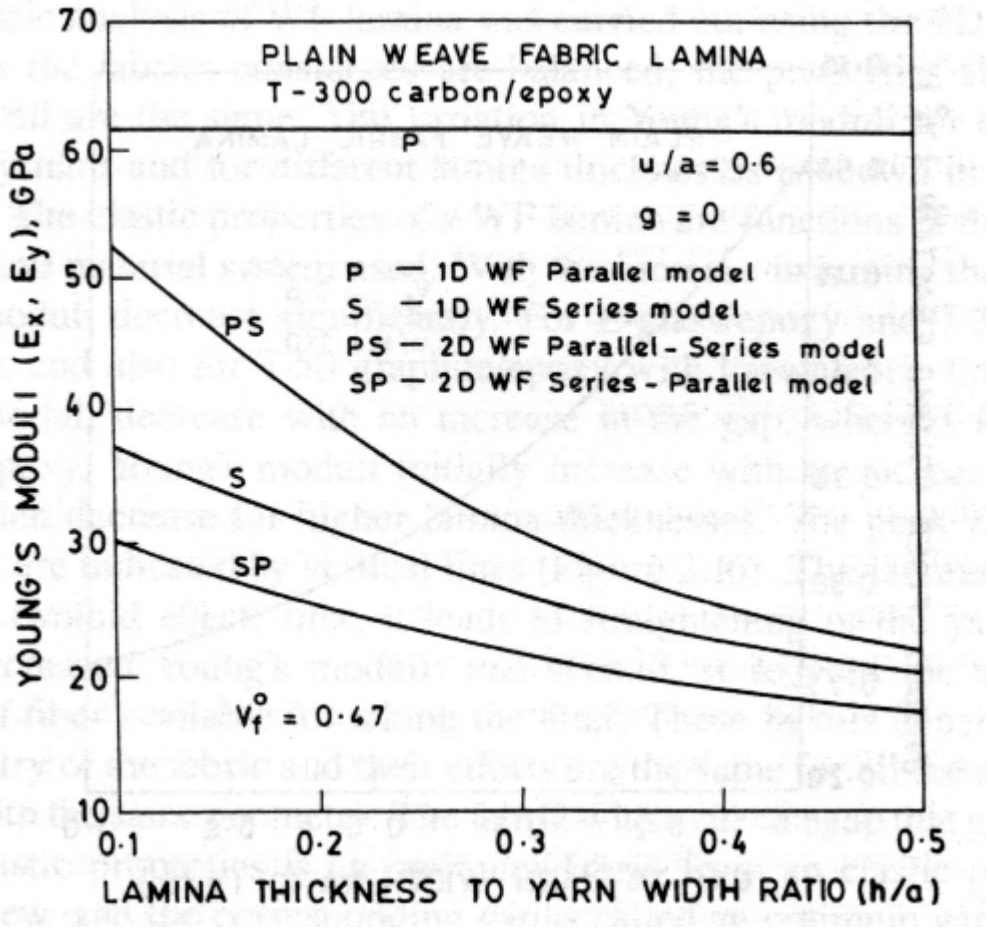

Fig. 2.8 Effective in-plane moduli from Ref. [12]

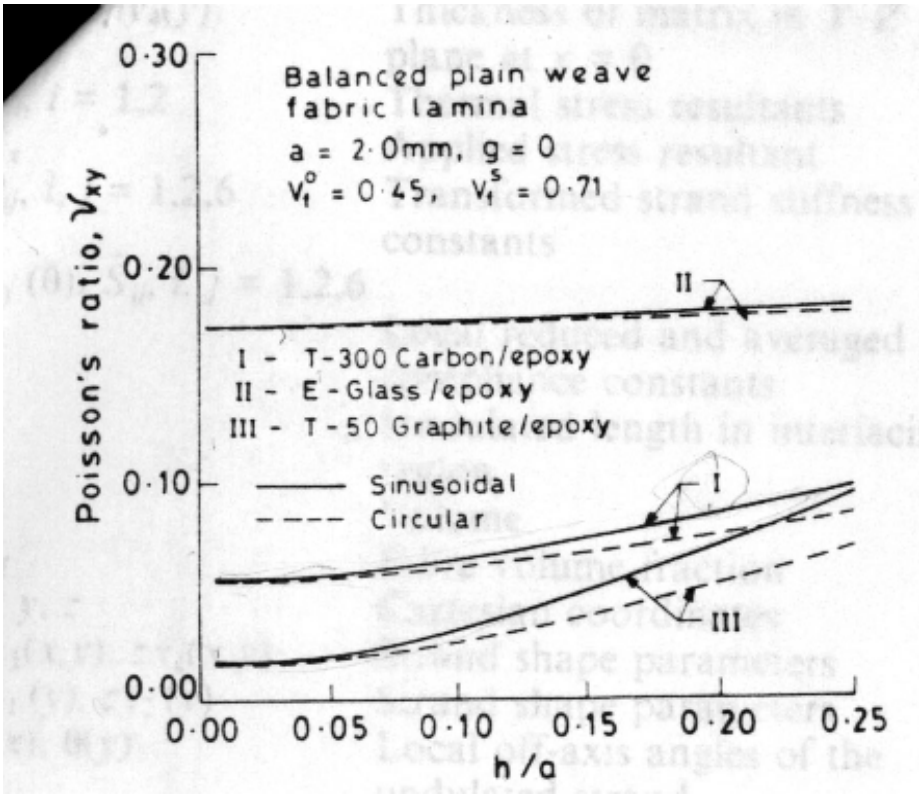

Fig. 2.9 In-plane Poisson's ratio from Ref. [12]

To better understand the trends in Poisson ratio with respect to increasing values of t/a, we specified the plane strain condition that $\varepsilon_z = 0$ in the final effective compliance matrix for the RUC. The effect of this plane strain constraint on the in-plane elastic constants are given in Table 2.14. The in-plane Poisson ratios ν_{xy} increase in value with respect to their values from the elasticity solution given in Table 2.13. More importantly, note that ν_{xy} increases with increasing values of t/a for the plane strain results shown in Table 2.14. The trend in ν_{xy} with increasing t/a for plane strain is reversed with respect to the trend from the elasticity solution. This plane strain result derived from the present analysis suggests that the predictions from Ref. [12] are based on the kinematic relation-

ships in classical lamination theory, where, in particular, it is assumed that $\varepsilon_z = 0$. Also, note that in-plane modulus E_{xx} for the plane strain results, Table 2.14, increase in value with respect to their values from the elasticity results, Table 2.11. However, the modulus E_{xx} decreases with increasing t/a for both the elasticity and plane strain results, as is predicted from the analyses in Ref. [12] as well. Increasing values of t/a imply larger crimp angles as is shown in Table 2.10. So one expects the in-plane moduli to decrease with increasing values of t/a since the fibers in the undulation regions are more steeply inclined with respect to the $x-y$ plane.

Table 2.14: In-plane elastic constants for plane strain in the example from Ref. [12]

n	β_c degrees	t/a	t_r, mm	E_{xx} GPa	G_{xy} GPa	ν_{xy}
1000	1.915	0.0213	0.0004	60.3959	4.1823	0.0940
2000	3.825	0.0426	0.0009	60.2364	4.1809	0.0942
3000	5.728	0.0638	0.0017	59.9728	4.1788	0.0947
4000	7.6180	0.0851	0.0030	59.9728	4.1788	0.0947
4000	7.6180	0.0851	0.0030	59.6085	4.1757	0.0953
5000	9.4919	0.1064	0.0048	59.1480	4.1719	0.0961
6000	11.3466	0.1277	0.0072	58.5968	4.1672	0.0970
7000	13.1790	0.1491	0.0105	57.9611	4.1618	0.0981
8000	14.9868	0.1704	0.0145	57.2476	4.1556	0.0994
9000	16.7681	0.1918	0.0195	56.4635	4.1488	0.1009
10000	18.5214	0.2133	0.0256	55.6158	4.1413	0.1025
11000	20.2459	0.2348	0.0327	54.7117	4.1332	0.1043
12000	21.9410	0.25664	0.0408	53.7580	4.1245	0.1062

2.3.5 Example from D. Scida et al.

The third example is from Scida, et al. [13], where the unit cell half width $a = 0.60$ mm, the yarn thickness $t = 0.05$ mm, the fiber volume fraction $V_f = 0.55$, and the yarn packing density $p_d = 0.80$. As in Ref. [12], the unit cell model in Ref. [13] does not use the number of filaments in a yarn and the filament diameter. We assumed a filament diameter $d_f = 0.007$ mm and determined from the GEOMET subroutine that $n = 428$. For $n = 428$, the preform geometric parameters from the GEOMET subroutine are the yarn thickness $t = 0.05$ mm, the undulation length $L_u = 0.52$ mm, the crimp angle $\beta_c = 8.59°$, resin thickness $t_r = 0$ mm, and a new yarn width $newa = a = 2.0$ mm. The yarns consist of E-glass fibers and vinylester derakane resin with properties listed in Table 2.15. The self consistent model and the rule of mixtures model were used to compute the equivalent yarn properties, and these are listed in Table 2.16.The unit cell effective properties are listed in Table 2.17 from Ref. [13], the present analysis using the self-consistent model for the yarns, and the present analysis using the rule-of-mixtures model for the yarns. The present analysis using the rule of mixtures for the yarn properties compares more favorably with the test and analysis results reported in Ref. [13].

Table 2.15: Fiber and resin properties from Ref. [13]

Material	E_{11}, GPa	E_{22}, GPa	G_{12}, GPa	G_{23}, GPa	ν_{12}
E-glass	73	73	30.4	30.4	0.20
Vinylester	3.4	3.4	1.49	1.49	0.35

Table 2.16: Equivalent yarn properties for the example from Ref. [13]

Model	E_{11}, GPa	E_{22}, GPa	G_{12}, GPa	G_{23}, GPa	ν_{12}	ν_{23}
Ref. [13]	57.5	18.8	7.44	7.26	0.25	0.29
Self-consistent	59.08	18.77	9.36	7.66	0.19	0.22
Rule of mixtures	59.08	14.33	6.23	5.82	0.23	0.23

Table 2.17: Effective properties for the unit cell for the example from Ref. [13]

Source	E_{xx}, E_{yy} GPa	E_{zz} GPa	G_{xy} GPa	G_{xz}, G_{yz} GPa	ν_{xy}	ν_{xz}, ν_{yz}
Test [13]	24.8	8.5	6.5	4.2	0.1	0.28
Analysis [13]	25.33	13.46	5.19	5.24	0.12	0.29
Present with self-consistent	28.95	17.17	6.89	6.62	0.13	0.31
Present with rule of mixtures	26.22	11.39	4.75	4.75	0.1	0.28

2.4 Comparison with the Mosaic Model from T. Ishikawa and T.W. Chou [6]

2.4.1 Geometric modeling

The “mosaic model” corresponds to an idealization of the woven fabric architecture. It has been developed for the first time ten years ago by T. Ishikawa and T.W. Chou [6] and represents an easy technique for modeling the stiffness and strength properties of fabric composites. Therefore it seems judicious to compare it with our own model. The basis of this idealization can be seen from Fig. 2.10 (*a* is the yarn width).

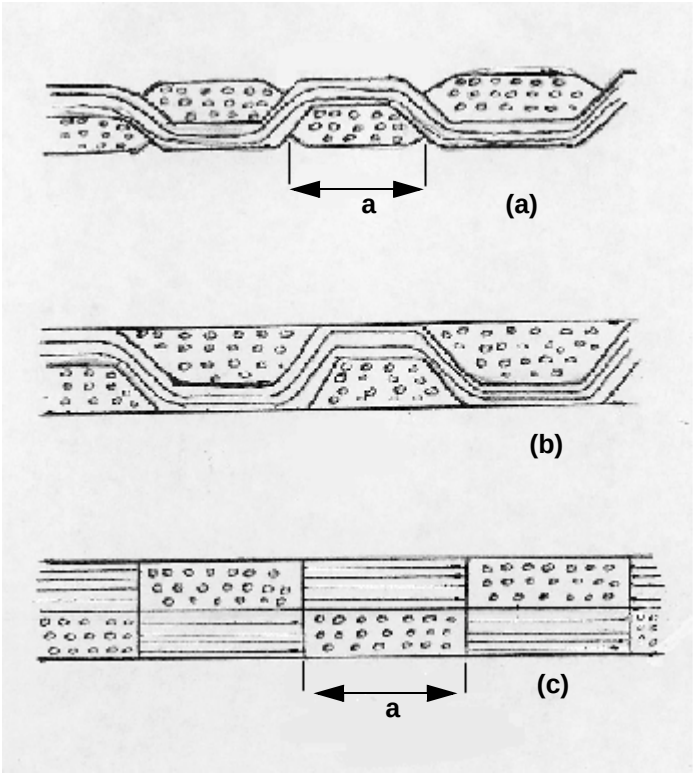

Fig. 2.10 Idealization of the mosaic model: (a) cross-sectional view of a plain weave fabric before resin impregnation; (b) plain weave fabric; (c) idealization of the mosaic model

Fig. 2.10a is a cross-sectional view of a plain weave fabric. As we've already seen, the fabric is composed of two sets of interlaced, mutually orthogonal yarns and the centerline of the yarn path consists of undulation portions and straight portions. The consolidation of the fabric with a resin matrix material is depicted in Fig. 2.10b, which can be simplified to the mosaic model of Fig. 2.10c. The key simplification of the mosaic model is the omission of the fiber continuity and undulation that exist in the actual fabric.

As a result, the fabric composite idealized by the mosaic model is now regarded as an assemblage of pieces of square asymmetric cross-ply laminates of width *a* (Fig. 2.11a). Each cross-ply laminate is made of two mutually orthogonal and unidirectional laminae of thickness $h/2$ so that the total laminate thickness in the *z*-direction is h and the *x*-*y* coordinate plane is positioned at the geometrical mid-plane of the laminate. Hence the Repeating Unit Cell (RUC) is made of 4 basic cross-ply laminates as shown in Fig. 2.11b.

The theoretical development of the mosaic model analysis is based on the classical lamination theory (CLT), under the assumption of the Kirchhoff-Love hypothesis (see Ref. [19] Chapter 2 p.17). Based upon the plane stress, we can express the reduced stiffness constants, Q_{ij}, of a unidirectional lamina, which has orthotropic symmetry in the *x*-*y* plane. For a single ply, assuming that fibers are aligned along the x direction, we get:

$$Q_{ij} = \begin{bmatrix} E_1/D_\nu & \nu_{12}E_2/D_\nu & 0 \\ \nu_{21}E_1/D_\nu & E_2/D_\nu & 0 \\ 0 & 0 & G_{12} \end{bmatrix} \tag{2.67}$$

where

$$D_\nu = 1 - \nu_{12}\nu_{21} \tag{2.68}$$

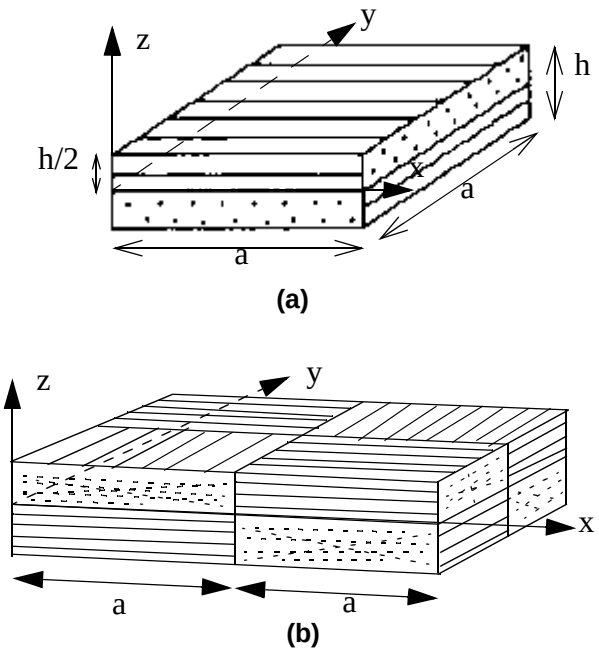

Fig. 2.11 Mosaic model architecture: (a) a basic cross-ply laminate; (b) the repeating unit cell (RUC)

The moduli and Poisson's ratios $E_1, E_2, G_{12}, \nu_{12}, \nu_{21}$ represent the yarn (warp or fill) material properties which are determined from fiber and resin properties using either self-consistent model or rule of mixture. Note that in this case as we consider the yarns embedded in the overall resin as a single ply, we need to consider the overall fiber volume fraction to compute these equivalent material properties and not the packing density as we did previously for our model. Note also that the Q_{ij} constants are symmetrical, i.e. $Q_{ij} = Q_{ji}$ and we get: $\nu_{21}E_1 = \nu_{12}E_2$ and only 4 of these variables are independent.

For a laminate consisting of several oriented plies, the constitutive equations are:

$$\begin{bmatrix} N_i \\ M_i \end{bmatrix} = \begin{bmatrix} A_{ij} & B_{ij} \\ B_{ij} & D_{ij} \end{bmatrix} \begin{bmatrix} \varepsilon_j \\ \kappa_j \end{bmatrix}, i, j = 1, 2, 6 \qquad (2.69)$$

where N_i, M_i, ε_j^o, and κ_j indicate membrane stress resultants, moment resultants, strain and curvature of the laminate midplane, respectively. The subscripts 1,2, and 6 indicate, in the global *x*-*y*-*z* coordinate system, the *x*-direction, *y*-direction, and the *x*-*y* plane, respectively.

Assuming that the laminate is made up of *N* unidirectional laminae, and that h_k represents the thickness of the first *k* plies in the *z*-direction, the k^{th} ply being therefore of thickness $h_k - h_{k-1}$, the components of the stiffness matrix *A*,*B* and *D* can be evaluated by integrating through the plate thickness in the *z*-direction:

$$(A_{ij}, B_{ij}, D_{ij}) = \sum_{k=1}^{N} \int_{h_{k-1}}^{h_k} (1, z, z^2) Q_{ij}^k dz \tag{2.70}$$

where Q_{ij}^k are the lamina reduced stiffness constants corresponding to the lamina bounded by h_k and h_{k-1} in the thickness direction. More explicitly, Eq. (2.70) can be written as:

$$A_{ij} = \sum_{k=1}^{N} Q_{ij}^k (h_k - h_{k-1}) \tag{2.71}$$

$$B_{ij} = \sum_{k=1}^{N} Q_{ij}^k \frac{1}{2} (h_k^2 - h_{k-1}^2) \tag{2.72}$$

$$D_{ij} = \sum_{k=1}^{N} Q_{ij}^k \frac{1}{3} (h_k^3 - h_{k-1}^3) \tag{2.73}$$

Thus for the cross-ply laminate described in Fig. 2.11a we can evaluate the corresponding stiffness matrix *A*, *B* and *D* using the previous equations. The laminate is composed of two unidirectional laminae of thickness $h/2$ with fibers in the *x*- and *y*-

directions. Hence, with N=2 in Eq. (2.70) we can define two reduced stiffness matrix Q_{ij}^{1} (in the x-direction) and Q_{ij}^{2} (in the y-direction) corresponding to each lamina, such that:

$$Q_{ij}^{1} = \begin{bmatrix} E_1/D_\nu & \nu_{12}E_2/D_\nu & 0 \\ \nu_{21}E_1/D_\nu & E_2/D_\nu & 0 \\ 0 & 0 & G_{12} \end{bmatrix} \tag{2.74}$$

and

$$Q_{ij}^{2} = \begin{bmatrix} E_2/D_\nu & \nu_{21}E_1/D_\nu & 0 \\ \nu_{12}E_2/D_\nu & E_1/D_\nu & 0 \\ 0 & 0 & G_{12} \end{bmatrix} \tag{2.75}$$

with $D_\nu = 1 - \nu_{12}\nu_{21}$.

Then substituting Eq. (2.74) and Eq. (2.75) in Eq. (2.71), Eq. (2.72) and Eq. (2.73), the non-vanishing stiffness constants are:

$$A_{11} = A_{22} = (E_1 + E_2)h/2D_\nu \tag{2.76}$$

$$A_{12} = \nu_{12}E_2h/D_\nu \tag{2.77}$$

$$A_{66} = G_{12}h \tag{2.78}$$

$$B_{11} = -B_{22} = (E_1 - E_2)h^2/8D_\nu \tag{2.79}$$

$$D_{11} = D_{22} = (E_1 + E_2)h^3/24D_\nu \tag{2.80}$$

$$D_{12} = \nu_{12}E_2h^3/12D_\nu \tag{2.81}$$

$$D_{66} = G_{12}h^3/12 \tag{2.82}$$

Note that the bending-stretching coupling constants B_{11} and B_{22} do not vanish because $E_1 \neq E_2$. Also note that A_{ij}, B_{ij} and D_{ij} are symmetrical constants as Q_{ij} are symmetric.

For the overall composite fabric, the architecture can no longer be seen as a stack of unidirectional laminates, but it is truly an entanglement of asymmetric cross-ply laminates. As a result we have to develop a methodology to compute the average stresses and strains within the RUC and the effective stiffness constant matrices that relate them. There are two main approaches to determine these constants, based upon either iso-stress or iso-strain assumptions, which allows simplification of the two-dimensional extent of the fabric composite plate by considering two one-dimensional models. The pieces of cross-ply laminates are either assumed to be in parallel or in series as shown in Fig. 2.12.

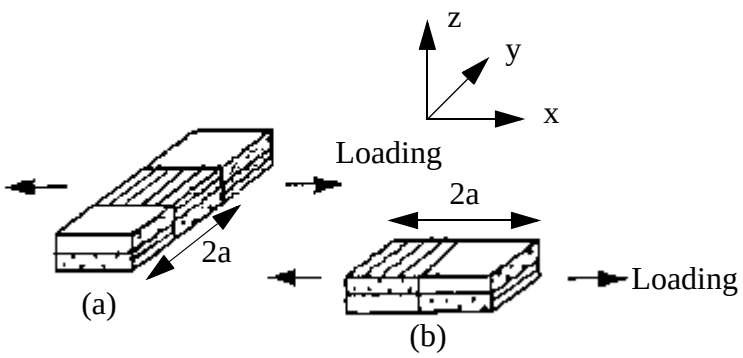

Fig. 2.12 Bound approach of the mosaic model: (a) parallel model; (b) series model

To do this simplification, we assume that the woven fabric lamina is subjected to a uniform in-plane loading along the *x*-axis. The infinitesimal pieces of a section parallel to the x-axis are then in series with respect to the loading direction and are assumed to be under uniform stress. On the other hand, the infinitesimal pieces of a section parallel to the *y*-axis are in parallel with respect to the loading direction, and the mid-plane strains of such pieces are assumed to be the same. The assembly of infinitesimal pieces of a section along

the loading direction with iso-stress condition is termed a series model, whereas the assembly of infinitesimal pieces across the loading direction with iso-strain condition is termed a parallel model.

In the series model (Fig. 2.12b) the disturbance of stress and strain near the interface of the interlaced region is neglected. The assumption of constant stress leads to the definition of average midplane strain and curvature which leads to upper bounds of the compliance constants. The lower bounds of stiffness constants are then obtained by taking the inverse of the compliance constant matrix.

In the parallel model (Fig. 2.12a), a uniform state of strain, ε^o, and curvature, κ, in the laminate midplane is assumed as a first approximation. This assumption leads to the definition of average stress and moment resultant which leads to upper bounds of the stiffness constants. The lower bounds of compliance constants are then obtained by taking the inverse of the stiffness constant matrix.

As our model is based on the iso-strain assumption, to compare our results with the mosaic model we will then proceed with the parallel model. Let $\overline{A_{ij}}$, $\overline{B_{ij}}$ and $\overline{D_{ij}}$ be the stiffness constant matrices relating the average stress resultant $\overline{N}$ and moment resultant $\overline{M}$ with ε^o and κ within the RUC. Let A_{ij}, B_{ij} and D_{ij} be the stiffness constant matrices for the cross-ply laminate defined in Fig. 2.11a (Eq. (2.76) to Eq. (2.82)). We can show (see Ref. [20]) that for a balanced plain weave fabric, we get:

$$\overline{A_{ij}} = A_{ij} \tag{2.83}$$

$$\overline{B_{ij}} = 0 \tag{2.84}$$

$$\overline{D_{ij}} = D_{ij} \tag{2.85}$$

To determine the in-plane engineering constants we define the normalized compliance constant matrix $\overline{a_{ij}}^*$ by:

$$[\bar{a}^*] = h[\bar{A}]^{-1} \tag{2.86}$$

Then the engineering constants are defined by (Ref [20]):

$$E_1 = 1/a_{11}^* \tag{2.87}$$

$$E_2 = 1/a_{22}^* \tag{2.88}$$

$$G_{12} = 1/a_{66}^* \tag{2.89}$$

$$\nu_{21} = -a_{21}^*/a_{11}^* \tag{2.90}$$

Note that as $\bar{A} = A$ and A varies linearly with respect to h ($A = \frac{h}{2}(Q^1 + Q^2)$), so $[\bar{a}^*] = h[\bar{A}]^{-1}$ is independent of h. As a result, the effective elastic properties of the plain weave fabric are independent of the thickness h of the RUC.

The numerical equations relative to the mosaic model have been programmed in Fortran in order to get effective material properties for the plain weave fabric. The Fortran program is called ‘mosaicplainweave.f’ and the results we obtained are discussed in the next section.

2.4.2 Results

It would be interesting to compare the results of our mosaic model with theoretical or experimental data from Ishikawa and Chou, however only few of these data are available in literature and we have to consider other authors.

1. *Comparison with N.K Naik’s mosaic model results:*

N.K Naik developed in Ref. [21] his own study of the mosaic model, based on Ishikawa and Chou theory, and made some analysis to evaluate the effect of undulation on elastic constants predicted by one-dimensional woven fabric (1D WF) models. Therefore, it seems interesting to check at first the validity of the equations previously described by comparing the results they give us with the results of N.K Naik. These results appear in Ref. [21], Tables 2.1 and 2.2, p. 23-24. The mosaic model is studied for T-300 carbon/ epoxy WF lamina and an overall fiber volume fraction of 0.47 is assumed. The following geometry is considered for the plain weave fabric:

- $a = 1.0$ mm (cross-ply width as described in Fig. 2.11a)
- $H = 2t = 0.1$ mm (cross-ply height as described in Fig. 2.11a)
- $V_f = 0.47$ (overall fiber volume fraction)

The elastic properties of fibers and resin used in the analysis are given in Table 2.18.

Table 2.18: Elastic Properties of Fibers and Matrix from Ref. [21]

Material	E_L GPa	E_T GPa	G_{LT} GPa	G_{TT} GPa	ν_{LT}
T-300 Carbon	230.0	40.0	24.0	14.3	0.26
Epoxy[a] Resin	3.5	3.5	1.3	1.3	0.35

a. Isotropic

We then compute the equivalent elastic properties of a single ply, which is seen as a unidirectional lamina made of fibers embedded in both yarn and matrix resin, using either a self consistent model or the rule of mixture. From these material properties we can evaluate the cross-ply stiffness constant matrices and furthermore, the normalized compliance constants $\overline{a_{ij}}^*$. Using Eq. (2.87) to Eq. (2.90) we can determine the elastic constants pre-

dicted by the mosaic model and then compare our results with those from Table 2.2 page 24 of Ref. [21]. These results are described below in Table 2.19.

Table 2.19: Comparison of moduli for the mosaic model using different equivalent ply elastic constant evaluation

Models	E_x, E_y GPa	G_{xy} GPa	ν_{xy}
Self-Consis-tent	59.4	3.19	0.0415
Rule of Mixture	58.3	2.34	0.0325
Ref.[21]	60.0	3.16	0.0450

We see that the results we got using the self-consistent model are relatively close to those from N.K. Naik. The difference between the results lay in the difference of computation of ply effective properties. No information is available to know which rule N.K. Naik used to compute the elastic properties of a single ply, but it seems that we can rely on the self-consistent model as a good approximation to N.K. Naik's model.

2. Comparison with the crimp model:

As we've seen previously, the RUC is made of two antisymmetric cross-ply laminae, each one made of two single plies where the yarns are embedded within the resin. As a result, to get the equivalent material properties of a single ply we can either consider the fiber material properties and the resin material properties (same for the yarns and the matrix) if we have access to these data, and use the rule of mixture or the self-consistent model with the overall fiber volume fraction as the fibers are embedded in both the yarn and matrix resin (e.g. N.K. Naik [12]). If we don't have access to the fiber material properties (e.g. R.A. Naik [9]), we can use a rule of mixtures incorporating directly the yarn

material properties and the resin properties, considering that the yarns are embedded within the matrix with a volume fraction equal to V_f / p_d.

Also, as we've seen previously, the mosaic model leads to results independent of the RUC thickness *h*. Therefore the reader shouldn't be surprised to see that in the following tables, the results for the mosaic model remain equal for different configurations of the RUC.

2.a Comparison with R.A. Naik:

The geometry is the same than the one described in Section 2.2.7 on page 35. The material properties of the yarns and the matrix are taken from Ref [9] and are given in Table 2.4 on page 45.

Using the rule of mixtures to compute the ply-equivalent elastic properties we get for the overall material properties of the plain weave fabric the results shown in Table 2.20.

Table 2.20: Comparison of Mosaic Model with R.A. Naik's results

Number of filaments, *n*	Ref. [9]			Mosaic model		
	$E_{xx} = E_{yy}$ GPa	G_{xy} GPa	ν_{xy}	$E_{xx} = E_{yy}$ GPa	G_{xy} GPa	ν_{xy}
2000	66.0613	4.8885	0.03292	78.5084	5.5200	0.03447
4000	62.3531	4.8648	0.02021	78.5084	5.5200	0.03447
6000	58.3916	4.8343	0.00858	78.5084	5.5200	0.03447
8000	55.3797	4.8035	0.00571	78.5084	5.5200	0.03447
10000	53.36	4.7755	0.01001	78.5084	5.5200	0.03447
12000	52.0058	4.7513	0.01719	78.5084	5.5200	0.03447
14000	51.0557	4.7308	0.02459	78.5084	5.5200	0.03447

2.b Comparison with N.K. Naik and Ganesh:

The geometry is the same as the one described in Section 2.2.7 on page 35. The material properties of the yarns and the matrix are taken from Ref [12] and are given in Table 2.8.

We can use either the self-consistent model or the rule of mixtures to compute the yarn/ply equivalent material properties as described previously. If we use the self-consistent model as in Section 2.2.7 on page 35, we get for the effective in-plane moduli and Poisson's ratio the values listed in Table 2.21.

:

Table 2.21: Comparison of Mosaic Model with N.K. Naik's results using self-consistent model to compute effective yarn/ply elastic properties

	Ref.[12]			Mosaic Model		
n	$E_{xx} = E_{yy}$, GPa	G_{xy}, GPa	ν_{xy}	$E_{xx} = E_{yy}$, GPa	G_{xy}, GPa	ν_{xy}
1000	57.9816	4.1823	0.05026	56.9208	3.0606	0.04206
2000	57.7588	4.1809	0.04925	56.9208	3.0606	0.04206
3000	57.3896	4.1788	0.04754	56.9208	3.0606	0.04206
4000	56.8770	4.1757	0.04511	56.9208	3.0606	0.04206
5000	56.2253	4.1719	0.04192	56.9208	3.0606	0.04206
6000	55.4404	4.1672	0.03794	56.9208	3.0606	0.04206
7000	54.5295	4.1618	0.03313	56.9208	3.0606	0.04206
8000	53.5016	4.1556	0.02749	56.9208	3.0606	0.04206
9000	52.3670	4.1488	0.02101	56.9208	3.0606	0.04206
10000	51.1378	4.1413	0.01372	56.9208	3.0606	0.04206
11000	49.8272	4.1332	0.00568	56.9208	3.0606	0.04206
12000	48.4500	4.1245	-0.00301	56.9208	3.0606	0.04206

2.5 Concluding Remarks

Assuming a yarn has a sinusoidal centerline in the undulation region, a uniform cross-sectional area normal to the centerline, and uniform thickness normal to the centerline, we have derived expressions for the fiber volume fraction, Eq. (2.12), and the shape of the cross section, Eq. (2.28), that are valid for large crimp angles. As is shown in Section 2.2.4 on page 27, these equations valid for large crimp angles reduce to the small crimp angle equations developed by R.A. Naik [9]. Also it is shown in Section 2.2.3 on page 25 that the crimp angle is limited to $45°$, if the filament corresponding to the curve on the concave side of the yarn is not to develop a cusp. In Section 2.2.5 on page 29 we determined that range of the ratio of the undulation length to the half length of the unit cell, $0 \le L_u/a \le 1$, also imposes a limit on the fiber volume fraction and yarn packing density. The nonlinear equations describing the preform geometry are solved by fixed point iteration as described in Section 2.2.6 on page 32.

The yarns are assumed to be untwisted, homogeneous and transversely isotropic, while the resin matrix is assumed to be isotropic. Using the iso-strain assumption equivalent, three-dimensional elastic moduli for the unit cell are determined. The equations for the equivalent moduli of the yarns, Eqs. (2.63) and (2.64), reduce to line integrals rather than volume integrals. The line integrals are evaluated by the trapezoid rule in the FORTRAN program ‘exactplainweave’ described in Appendix C, and this reduction to line integrals from volume integrals renders the evaluation of equivalent moduli efficient.

The present results for the equivalent moduli are compared to the predictions by R.A. Naik [9] in Table 2.5 on page 46 to Table 2.7 on page 47. Our results are the same as those from R.A. Naik for very small crimp angles, but differ as the crimp angle increases. These differences for increasing crimp angles are expected, since the preform geometry in Ref. [9] is limited to small crimp angles. The Young moduli E_{xx}, E_{yy}, E_{zz} from our analysis are, in general, less than those from the analysis of Ref. [9], but transverse shear moduli

G_{yz}, G_{zx} are greater than those from Ref. [9]. There is little difference in the in-plane shear modulus from the present results and those of Ref. [9].

Equivalent moduli computed for a carbon-epoxy, balanced plain weave example taken from N.K. Naik and Ganesh [12] are listed in Table 2.11 on page 50 to Table 2.14 on page 55. Fair agreement of the present results for the in-plane data to the corresponding data presented as graphs in Ref. [12] are obtained. Part of the discrepancies are due to the fact that the ratio of the undulation length to the half width of the unit cell, L_u/a, is unity from our algorithm, while this ratio is listed as 0.6 in Ref. [12]. See Fig. 2.8. Also, the trend for the in-plane Poisson ratio, ν_{xy}, to increase for increasing crimp angles in Ref. [12], which is equivalent to increasing ratios h/a shown in Fig. 2.9, appears to be due to the kinematic assumption from classical lamination theory that the thickness normal strain vanishes, or $\varepsilon_z = 0$. Elasticity results show ν_{xy} to decrease with increasing crimp angle in Table 2.13 on page 52. Refer to Table 2.14 on page 55 for our results for ν_{xy} when it is assumed that $\varepsilon_z = 0$.

Equivalent moduli computed for an E-glass/vinylester, balanced plain weave example taken from D. Scida et al. [13] are listed in Table 2.17 on page 57. Our results compare reasonably well with those in Ref. [13] when we use the rule-of-mixtures to compute the yarn properties.

Neglecting the influence of the undulating region, we have also derived equations for the mosaic model of Ishikawa and Chou [6] for a plain weave fabric, based on Classical Lamination Theory. Equivalent in-plane moduli were computed for the example of a T-300 carbon/epoxy balanced plain weave fabric taken from N.K. Naik [21], where the length of the undulating region was set to zero. Our results for the mosaic model compare fairly well with those in Ref. [21] when we use the self-consistent model to compute the yarn effective properties. Results for in-plane moduli were also compared to the crimp models from R.A. Naik [9] and N.K. Naik & Ganesh [12] and are listed in Table 2.20 on

page 68 and Table 2.21 on page 69. As described in Section 2.4.1, the effective elastic properties of the plain weave fabric for the mosaic model are independent of the thickness h of the RUC. As a result, in Tables 2.20 and 2.21, in-plane moduli for the mosaic model do not vary with the yarn filament count n. Thus, the mosaic model does not allow to capture the trend for the in-plane moduli and Poisson's ratio to decrease with n. However, for small values of the yarn filament count (typically $n = 1000$), that is for 'thin' RUC, the mosaic model compares reasonably well with those in Ref. [9] and [12]. When the yarn filament count increases, the influence of the undulating region can no longer be neglected and some major discrepancies appear in the results.

Chapter 3.Braided Fabrics

3.1 2D Braided Composite

3.1.1 Fabric architecture

A 2D braided preform consists of two sets of intertwined yarns, one set oriented in the $+\theta_b$ direction and the other in the $-\theta_b$ direction, the braider yarns interlacing in a 1x1 pattern similar to the plain weave fabric. Braided preforms are fabricated over a cylindrical mandrel as described in Chapter 1. The braid angle θ_b is controlled by the rotational speed of the yarn carriers relative to the transverse speed of the mandrel and the sequence of the crossovers is such that the two sets of yarns interlace to form a continuous tubular fabric. The relative simplicity and high productivity of braiding make it a cost-effective alternative to other manufacturing processes. Nevertheless, restricted width, diameter, thickness or shape selection are major limitations in the design of machine-made braided fabrics.

3.1.2 Geometric modeling

The RUC for the 2D braided architecture is shown in Fig. 3.1. The sectional view in Fig. 3.1 (section A-A) shows the undulations of a $+\theta_b$ braider yarn as it crosses over a $-\theta_b$ braider yarn. The major discrepancy with the balanced plain weave geometry is that the yarns now interlace at non-orthogonal angles. The angle between the $+\theta_b$ and $-\theta_b$ braider

yarns is then $2\theta_b$. This difference in the orientation of the RUC is accounted for in the derivation of the yarn path for the 2D braid.

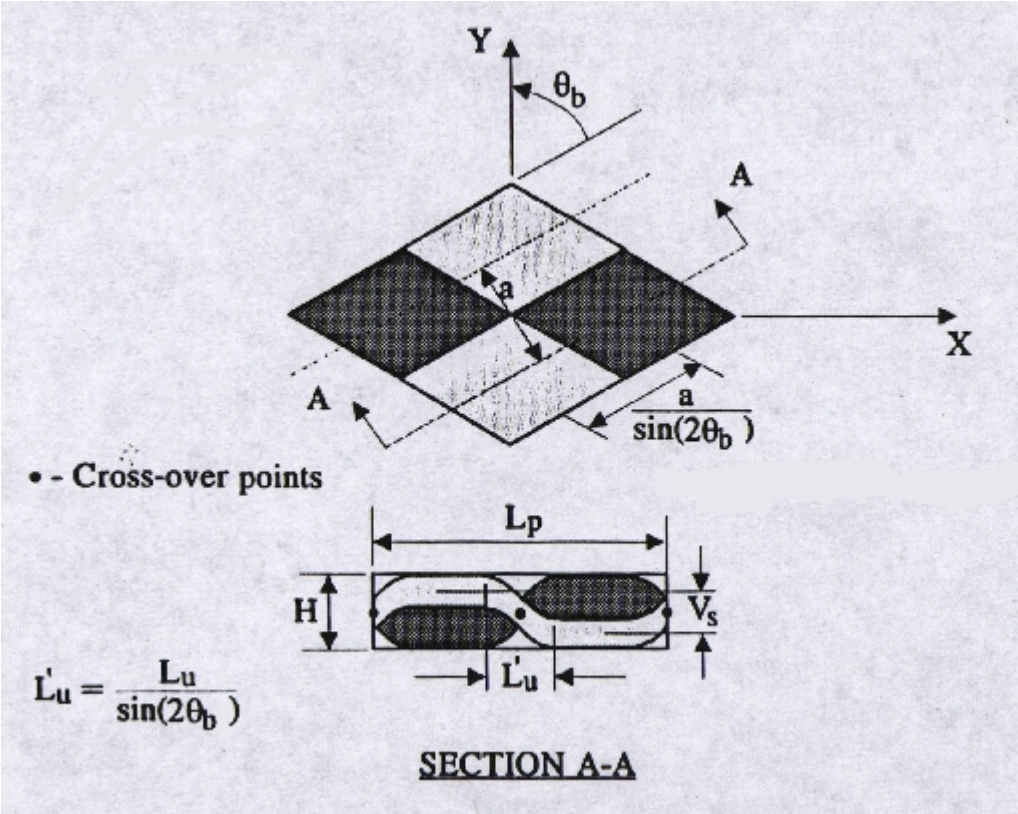

Fig. 3.1 RUC geometry and notation for 2D braided architecture

Following R.A. Naik [9], the geometry of the path of the braider yarns in the RUC is modeled using the two assumptions quoted in Chapter 2, Section 2.2 on page 17. However in order to simplify our model, we assume that the crimp angles remain small within the RUC, such that: $0 \le \beta_c^2 \ll 1$ and we obtain approximations for the derivation of the yarn geometry parameters as in Chapter 2, Section 2.2.4 on page 27.

The $+\theta_b$ and $-\theta_b$ braider yarns are assumed to have the same number of filaments, n, with all filaments having the same diameter, d_f, and with the braider yarns having the

same yarn packing density, p_d. The cross-sectional area A of the yarns is thus given by Eq. (2.1). Also, it is assumed that the spacing between the $+\theta_b$ and $-\theta_b$ braider yarns is the same and that there is no gap between adjacent yarns. The yarn spacing (perpendicular to the yarn direction), which is also the yarn width, is denoted by a. The planform shape of the RUC as shown in Fig. 3.1 is a trapezoid of height $2a$ and length $(2a)/(\sin 2\theta_b)$ and its thickness dimension is denoted by H. The overall volume of the RUC is thus:

$$V = \frac{4Ha^2}{\sin 2\theta_b} \tag{3.1}$$

The RUC is globally referenced to a Cartesian coordinate system $X - Y - Z$, such that the $+\theta_b$ braider yarn makes an angle $+\theta_b$ with the Y-axis and the $-\theta_b$ braider yarn makes an angle $-\theta_b$ with the Y-axis, and the Z-axis is in the thickness direction, such that $-H/2 \le Z \le H/2$. However, to determine the yarn path geometry, a local coordinate system $x - y - z$ is used, with the x-axis in the direction of the braider yarn, the z-axis in the thickness direction, and the y-axis such that $x - y - z$ be a right-handed, orthogonal triad as shown in Fig. 3.1.

Fig. 3.2 shows the cross-section of the RUC along the centerline of the $+\theta_b$ braider yarn in the corresponding local coordinate system $x - y - z$. The geometry of the yarn path is almost exactly identical to the plain weave fabric, except that all geometry parameters are now projected along the path. The yarn width a is projected into $a' = a/\sin 2\theta_b$, the length of the undulating region L_u is projected into $L_u' = L_u/\sin 2\theta_b$ and the yarn cross-sectional area A is projected into $A' = A/\sin 2\theta_b$.

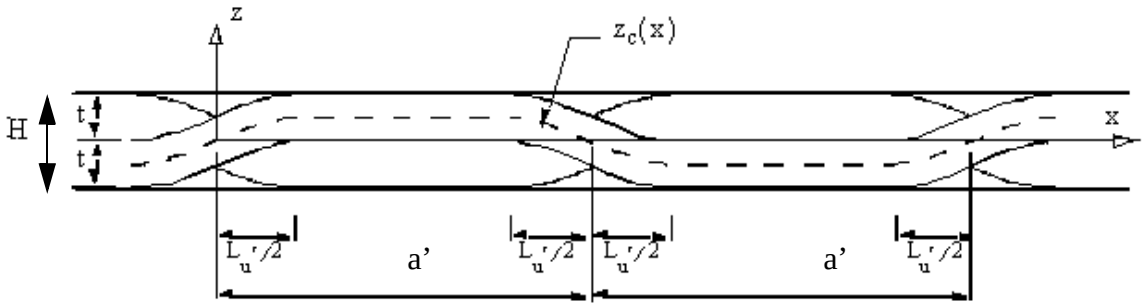

Fig. 3.2 Cross section of the RUC along the + θ_b braider yarn

The thickness of the yarn along the centerline of the yarn path is denoted by t. We assume that the ratio V_f/p_d remains in a range such that $0 \le L_u'/a' \le 1$ and thus, there is no need to add an additional resin layer to the unit cell. The condition of a low relative fiber volume fraction is discussed in more detail in Chapter 2, Section 2.2.5 on page 29. We thus get $H = 2t$. As in the plain weave fabric, the yarn undulations for the 2D braid are centered around three cross-over points for each yarn. The equation of the centerline in the undulating portions for the $+\theta_b$ braider yarn shown in Fig. 3.2 is given by:

$$z_c(x) = (t/2)\sin(\pi(x - x_{cop})/L_u') \qquad -L_u'/2 \le x - x_{cop} \le L_u'/2 \tag{3.2}$$

where $x = x_{cop}$ is a cross-over point. In the straight portion, the equation of the centerline becomes: $z_c(x) = \pm t/2$. Equations of the centerline along with small crimp angle approximation allow us to derive equations for the fiber volume fraction and the yarn cross-sectional shape of the yarn in a process similar to Section 2.2.4 on page 27 of Chapter 2. Replacing L_u by L_u', a by a', A by A' and with $h_r = 1$ (no resin added) we get the equivalent of Eq. (2.39):

$$V_f = p_d A'/ta' \qquad A' = a't\left[1-\left(\frac{L_u'}{a'}\right)(1-2/\pi)\right] \tag{3.3}$$

In terms of L_u, a and A, Eq. (3.3) becomes:

$$V_f = p_d A/ta \tag{3.4}$$

$$A = at\left[1-\left(\frac{L_u}{a}\right)(1-2/\pi)\right] \tag{3.5}$$

So Eq. (2.39) is unchanged and we can solve Eqs. (3.4) and (3.5) along with Eq. (2.1) to determine A, t and L_u.

3.1.3 Determination of three-dimensional effective moduli

As for the plain weave fabric, the RUC is assumed to be composed of three linear elastic phases: two $+\theta_b$ yarns, two $-\theta_b$ yarns, and resin matrix. The total strain energy for the RUC is

$$U = \frac{1}{2}\int_V \varepsilon^T C\varepsilon dV \tag{3.6}$$

where V is the volume of the RUC given by Eq. (3.1), the engineering strain vector is specified by $\varepsilon^T = \left[\varepsilon_x\ \varepsilon_y\ \varepsilon_z\ \gamma_{yz}\ \gamma_{zx}\ \gamma_{xy}\right]$ and C is the six-by-six, symmetric elasticity matrix. Homogenization of the RUC to determine its effective moduli is also based on the iso-strain assumption. By this iso-strain assumption, the strain vectors can be taken out of the integrand of Eq. (3.6) and the strain energy can be written in the form:

$$U = \frac{V}{2}\varepsilon^T C_{eq}\varepsilon \tag{3.7}$$

where the equivalent elasticity matrix for the RUC is defined by

$$C_{eq} \equiv \frac{1}{V}\int_V C dV. \tag{3.8}$$

As we assumed a small crimp angle, the integral above can be approximated by integrating along the projected path of the yarns, rather than the exact path. As a result, the differential volume element $dV = A\sqrt{1+(z_c')^2}dx$ (where x represents the local coordinate direction along the yarn path) is approximated by:

$$dV = Adx \tag{3.9}$$

The overall volume of the four braider yarns is then approximated by:

$$V_{yarn} = 4 \cdot A \cdot L_p \tag{3.10}$$

where the yarn projected length is defined by:

$$L_p = \frac{2a}{\sin 2\theta_b} \tag{3.11}$$

The volume of the RUC is therefore subdivided into the volume of the two $+\theta_b$ yarns, $2AL_p$, the two $-\theta_b$ yarns, $2AL_p$, and the volume of the resin matrix, $V_{\text{resin}} = V - V_{yarn}$. As for the plain weave, the equivalent elasticity matrix is the sum of the volume integral of the elasticity matrices over each phase. That is[1],

$$C_{eq} = \frac{1}{V}\left\{2A\int_0^{L_p} C_{\theta_b}dx + 2A\int_0^{L_p} C_{-\theta_b}dx + \int_{V_{\text{resin}}} C_{\text{resin}}dV\right\} \tag{3.12}$$

Equation (3.12) can be re-written in the form

$$C_{eq} = v_{\theta_b}C_{eq\theta_b} + v_{-\theta_b}C_{eq-\theta_b} + v_r C_{eqr} \tag{3.13}$$

1. Note the coefficient 2 in front of the braider yarn effective stiffness matrices as these matrices are identical for the two $+\theta_b$ yarns and for the two $-\theta_b$ yarns.

where the volume fractions of the $+\theta_b$ yarns, the $-\theta_b$ yarns, and the resin are given by

$$v_{\theta_b} = v_{-\theta_b} = (2AL_p)/V \qquad v_r = V_{\text{resin}}/V = 1 - v_{\theta_b} - v_{-\theta_b} \tag{3.14}$$

And the equivalent elasticity matrices for the $+\theta_b$ and $-\theta_b$ yarns in Eq. (3.13) can be expressed as:

$$C_{eq\theta_b} = \frac{1}{L_p}\int_0^{L_p} C_{\theta_b} dx = \frac{1}{L_p}\int_0^{L_p} C_1(\theta_b, \beta_{\theta_b}) dx \tag{3.15}$$

$$C_{eq-\theta_b} = \frac{1}{L_p}\int_0^{L_p} C_{-\theta_b} dx = \frac{1}{L_p}\int_0^{L_p} C_1(-\theta_b, \beta_{-\theta_b}) dx \tag{3.16}$$

where the elasticity matrix in the local *x*-*y*-*z* coordinate directions at a generic position in a yarn, is denoted by $C_1(\theta, \beta)$. The six-by-six matrix $C_1(\theta, \beta)$ is derived in Appendix B and given by Eq. (B.9).The angles of the centerlines of the $+\theta_b$ and $-\theta_b$ yarns with respect to the local x-axis are, respectively, determined by

$$\beta_{\theta_b} = \text{atan}\,(z'_{\theta_b}) \qquad \beta_{-\theta_b} = \text{atan}(z'_{-\theta_b}) \tag{3.17}$$

where the function z'_{θ_b} over one-half of the length of the $+\theta_b$ yarn is:

$$z'_{\theta_b} = \begin{cases} \tan\beta_c \cos(\pi x/L_u') & x \in (0, L_u'/2) \\ 0 & x \in (L_u'/2, a' - L_u'/2) \\ -\tan\beta_c \cos[\pi(x-a')/L_u'] & x \in (a' - L_u'/2, a') \end{cases} \tag{3.18}$$

and the function $z'_{-\theta_b}$ over one-half of the length of the $-\theta_b$ yarn is:

$$z'_{-\theta_b} = \begin{cases} -\tan\beta_c \cos(\pi x/L_u') & x \in (0, L_u'/2) \\ 0 & x \in (L_u'/2, a' - L_u'/2) \\ \tan\beta_c \cos[\pi(x-a')/L_u'] & x \in (a' - L_u'/2, a') \end{cases} \tag{3.19}$$

Recall that $a' = a/\sin 2\theta_b$ and $L_u' = L_u/\sin 2\theta_b$) and β_c denotes the crimp angle as seen along the braider yarn path, such that: $\tan\beta_c \equiv \pi t/(2L_u')$.

The resin is assumed to be homogeneous and isotropic, so its equivalent elasticity matrix is equal to its elasticity matrix evaluated point-wise; i.e.,

$$C_{eqr} = \frac{1}{V_{resin}} \int_{V_{resin}} C_{\text{resin}} dV = C_{\text{resin}} \tag{3.20}$$

This resin elasticity matrix is given by Eq. (B.10) in Appendix B. As for the plain weave, the integrations in Eq. (3.15) and (3.16) can be performed over one quarter of the RUC rather than on the overall volume. Indeed, the equivalent elasticity matrices for the $+\theta_b$ and $-\theta_b$ yarns are the same if these integrations are performed over the interval from 0 to *a'* or over the interval from *a'* to $2a' = L_p$. Thus we can write:

$$C_{eq\theta_b} = \frac{2}{L_p} \int_0^{a'} C_1(\theta_b, \beta_{\theta_b}) dx \tag{3.21}$$

$$C_{eq-\theta_b} = \frac{2}{L_p} \int_0^{a'} C_1(-\theta_b, \beta_{-\theta_b}) dx \tag{3.22}$$

The integrations indicated in Eqs. (3.21) and (3.22) are done numerically using the trapezoidal rule in the FORTRAN program 'braidedstiff.f'. This program uses the same subroutines as those described in Appendix C except for the GEOMET subroutine which is not used in the case of small crimp angle approximation. The architecture parameters are thus computed directly from the equations of Section 3.1.2 on page 73.

3.1.4 Comparison with R.A. Naik

Effective moduli are computed for a 2D braid example from Ref.[9]. As in the plain weave composite, a yarn spacing $a = 1.411\text{mm}$ and an overall fiber volume fraction $V_f = 0.64$ are used. Also, a yarn packing density $p_d = 0.75$ and a diameter of fiber $d_f = 0.007\,\text{mm}$ are considered. The yarn and resin properties are those given in Table 2.4 on page 45. As we assumed low crimp angles, there is no need to iterate to determine the geometry parameters t and L_u. From Eqs. (3.4) and (3.5) we get:

$$L_u = a\frac{p_d - V_f}{p_d}\left(\frac{\pi}{\pi - 2}\right) \tag{3.23}$$

And t is evaluated using Eq. (3.4) as:

$$t = p_d A/(V_f a) \tag{3.24}$$

For the corresponding values of V_f, a, p_d and d_f, the values of t, L_u and β_c are listed in Table 2.3 on page 36 as a function of the number of filaments within the yarns: n.

The results for the composite properties are given in Tables 3.1 and 3.2 as a function of the braid angle values within the range $\theta_b \in [10°, 80°]$. A good correlation is obtained with the results given in Ref. [9]. Also, for a 45 degree braid angle, Table 3.3 shows the comparison with the FEM results of Ref. [22] for the same braid parameters. As we have programmed the exact same equations as those given by R.A. Naik in Ref. [9], it is expected that we should get the same results. However some minor discrepancies arise as a result of round-off errors for example.

Tables 3.1 and 3.2 show that in-plane properties, E_{xx}, E_{yy}, G_{xy} and ν_{xy} vary significantly with braid angle, but through-thickness moduli E_{zz}, G_{yz}, G_{zx} and Poisson's ratios ν_{yz} and ν_{xz} are less sensitive to braid angle variations.

Table 3.1: Effective Moduli for the 2D braid example from Ref. [9]

θ_b (in deg).	E_{xx}, GPa	E_{yy}, GPa	E_{zz}, GPa	G_{yz}, GPa	G_{zx}, GPa	G_{xy}, GPa
10	11.45	115.62	11.55	5.19	4.34	8.40
20	11.43	85.31	11.75	5.27	4.44	16.55
30	11.97	46.95	12.07	5.78	4.80	25.49
40	14.66	23.73	12.42	5.52	5.16	31.41
45	17.97	17.97	12.48	5.31	5.31	32.25
50	23.73	14.66	12.42	5.16	5.52	31.41
60	46.95	11.97	12.07	4.80	5.78	25.49
70	85.31	11.43	11.75	4.44	5.27	16.55
80	115.62	11.45	11.55	4.34	5.19	8.40

Table 3.2: Effective Poisson's ratios for the 2D braid example from Ref. [9]

θ_b (in deg).	ν_{yz}	ν_{xz}	ν_{xy}
10	0.16	0.32	0.051
20	-0.00972	0.29	0.14
30	-0.033	0.24	0.31
40	0.043	0.15	0.57
45	0.0982	0.0982	0.74
50	0.15	0.043	0.92
60	0.24	-0.033	1.20
70	0.29	-0.00972	1.06
80	0.32	0.16	0.52

Table 3.3: Comparison of Effective Properties Results for 45 Degree Braid Angle

Model	E_{xx}, GPa	E_{yy}, GPa	E_{zz}, GPa	G_{yz}, GPa	G_{zx}, GPa	G_{xy}, GPa	ν_{yz}	ν_{xz}	ν_{xy}
Present	17.97	17.97	12.48	5.31	5.31	32.25	0.0982	0.0982	0.74
Ref. [9]	17.9	17.9	12.5	N.A.	N.A.	32.2	0.098	0.098	0.74
FEM results from Ref. [22]	17.9	17.9	12.5	N.A.	N.A.	32.2	0.098	0.098	0.74

3.2 2x2 2D Triaxial Braided Composite

3.2.1 Fabric architecture

A 2x2 2D triaxial braid differs from a 2x2 2D braid by the introduction of axial yarns between the braider yarns in the longitudinal or the vertical direction in the planform view. The incorporation of additional axially-oriented yarns provides a useful reinforcement to the braided structure and by controlling the relative size of the axial yarns and the braid angle, a wide range of final properties can be obtained. The axial yarns are supplied from a set of stationary carriers mounted parallel to the rotating carrier of the cylindrical mandrel. These longitudinal yarns pass through guide tubes located at the centers of the lobes of the undulating tracks that guide the braider yarn carriers, and consequently this third set of yarns is trapped between the two sets of braider yarns. The axial yarns are not truly interwoven with the yarns from either of the braider sets, which are themselves mutually intertwined, but the array of axial yarns is effectively located at the center plane of the resultant fabric and follows a straight path.

3.2.2 Geometric modeling

The RUC for the 2x2 2D triaxially braided laminate is taken from R.A. Naik [9] and is depicted in Fig. 3.3 a). Most of the equations derived in this section have been previously derived by R.A. Naik in Ref. [9] and [10]. However R.A. Naik omitted any reference to the geometrical assumptions related to his model; therefore, a detailed description of the different steps along with diagrams of the geometry are provided here. The sectional view in Fig. 3.3 b) (section S-S) shows the undulations of a $+\theta_b$ braider yarn as it crosses over both a $-\theta_b$ braider yarn and the axial yarns. The geometric model is based on the same assumptions as for the 2D braid, including the small crimp angle approximation. However, we have to distinguish the braider yarn geometry from the axial yarn geometry as the axial yarns are usually much thicker than the braider yarns. In order to simplify our modeling we will assume that both the braider and axial yarns have the same packing density, p_d, same fiber diameter, d_f, but that they have different filament counts, the axial yarn filament count being denoted by n_o and the braider yarn filament count being denoted by n_b, with usually $n_o > n_b$. If we note, respectively, A_o and A_b as the true (perpendicular to the yarn paths) axial and braider yarn cross-sectional areas, we can express A_o and A_b as a function of n_o and n_b similarly to Eq. (2.1):

$$\begin{aligned} A_o &= \frac{\pi d_f^2 n_o}{4 p_d} \\ A_b &= \frac{\pi d_f^2 n_b}{4 p_d} \end{aligned} \tag{3.25}$$

If the fiber diameter, yarn packing density and filament count is known for both axial and braider yarns, then Eq. (3.25) can be solved for A_o and A_b. As before, these quantities are assumed to remain constant along the entire yarn path.

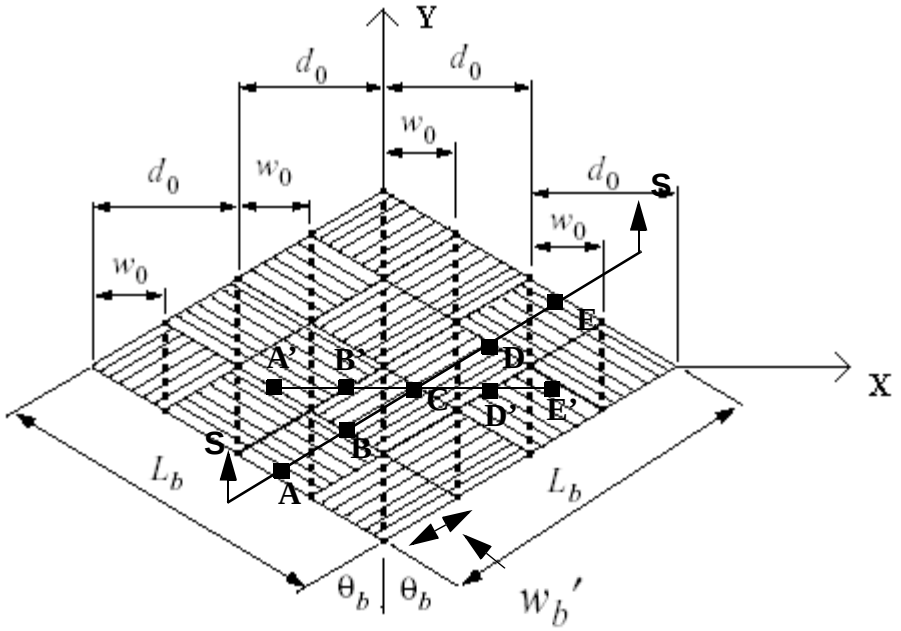

a)

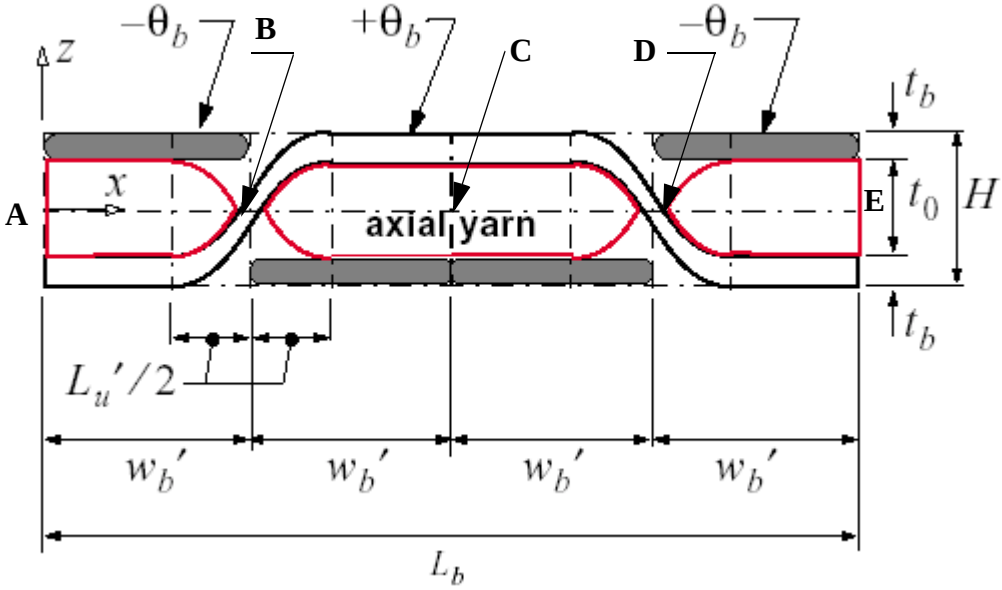

b)

Fig. 3.3 (a) Representative unit cell of a 2x2 2D triaxial braided composite; (b) Cross-sectional view along braider yarn of section S-S

As shown in Fig. 3.3 a) the RUC consists of four axial yarns and two sets of four braider yarns, one set oriented at an angle of $+\theta_b$, positive clockwise, with respect to the vertical axis in the figure (or the Y-axis) and the other set oriented at $-\theta_b$ with respect to the Y-axis. The axial yarns are aligned with the Y-axis, the width of each axial yarn is denoted by w_o and the axial yarn spacing is denoted by d_o. As can be determined from Fig. 3.4, the projected length of the braider yarns in the midplane of the RUC is given by:

$$L_b = 2d_o / \sin\theta_b \tag{3.26}$$

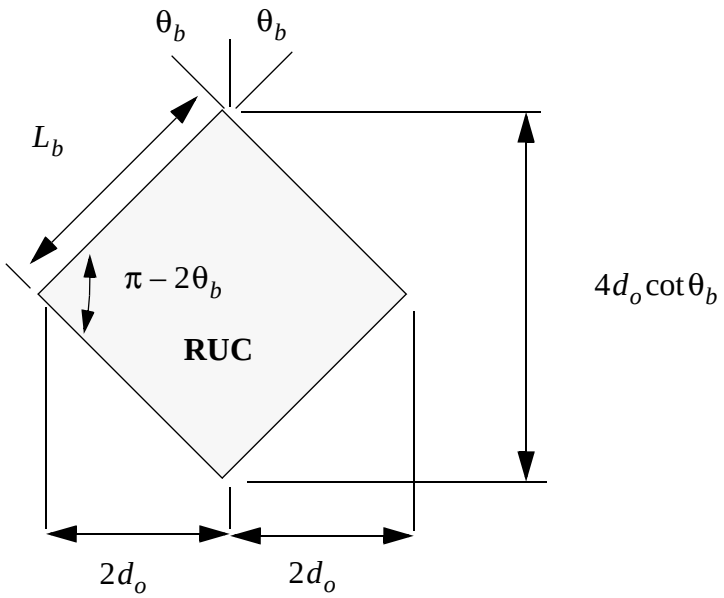

Fig. 3.4 RUC planform geometry

The width of the braider yarns (perpendicular to the yarn path) is denoted by w_b, which is also the yarn spacing as we assume that there is no gap between adjacent braider yarns. Along the braider yarn path, w_b projects into w_b' such that $w_b' \sin 2\theta_b = w_b$ and

$w_b' = L_b/4$. This width can also be related to the axial yarn spacing as shown in Fig. 3.4 by $w_b'\cos(\pi/2 - \theta_b) = d_o/2$, or

$$w_{b'} = d_o/(2\sin\theta_b) \tag{3.27}$$

So we can relate w_b to d_o to get

$$w_b = d_o\cos\theta_b \tag{3.28}$$

Eq. (3.28) allows us to determine the width of the braider yarns in terms of the axial yarn spacing and the braid angle.

To determine the overall length of the axial yarns in the RUC we consider the center-line of the first axial yarn on the left of the RUC (Fig. 3.5 a)). We can express the length l of this centerline in terms of the braider yarn width w_b' and the braid angle θ_b as shown in Fig. 3.5 b), we get $l = L/2 = w_b'\cos\theta_b$. As represented in Fig. 3.5 a), the lengths of succeeding axial yarns to the right of this yarn are respectively five, seven, and three times this length. Thus, if we denote by L_o the total length of the four axial yarns within the RUC we get $L_o = 16l = 16w_b'\cos\theta_b$. Eliminating w_b' in this last equation using Eq. (3.27), we can write:

$$L_o = 8d_o\cot\theta_b \tag{3.29}$$

The planform area of the RUC is $L_b^2\sin 2\theta_b$ and if we note respectively t_o and t_b the thicknesses of the axial and braider yarn along the centerline of the yarn paths the overall thickness of the RUC H can be written as:

$$H = 2t_b + t_o \tag{3.30}$$

Then the overall volume of the RUC is:

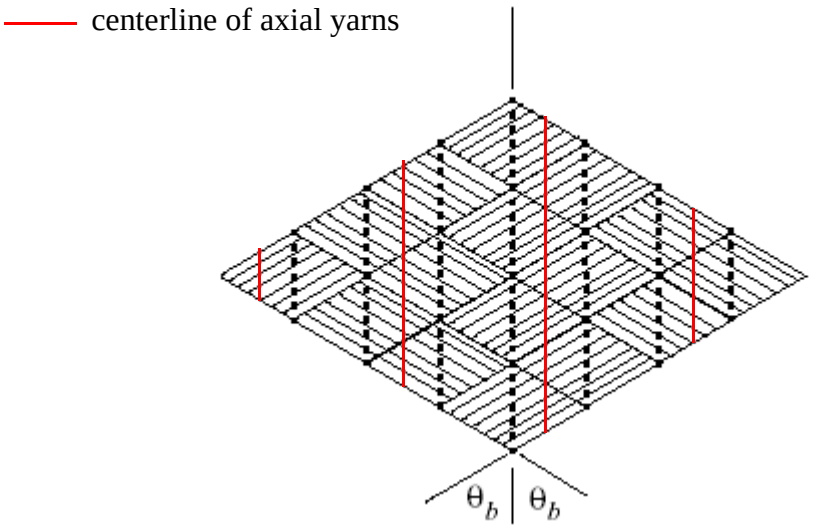

a)

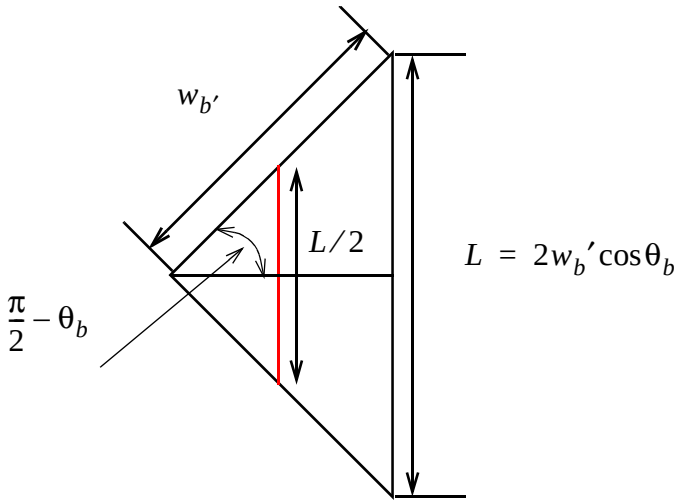

b)

Fig. 3.5 (a) Description of axial yarn centerlines; (b) Geometry of first axial yarn centerline

$$V = L_b^2 \sin 2\theta_b H \tag{3.31}$$

As we assumed small crimp angles, following the same reasoning as for the 2D braid, we can approximate the volume occupied by the braider yarns, V_b, by the product of their cross-sectional areas and their projected lengths in the midplane of the RUC. As the RUC consists of 8 braider yarns with identical cross-sectional areas A_b, and with projected lengths L_b, we get:

$$V_b = 8L_bA_b \tag{3.32}$$

As the axial yarn path consists only of straight portions, the exact volume occupied by the axial yarns within the RUC, V_o, is then:

$$V_o = L_oA_o \tag{3.33}$$

As a result, the volume occupied by the fibers within the RUC is $p_d(8L_bA_b + L_oA_o)$ and the volume occupied by the resin is:

$$V_r = L_b^2 \sin(2\theta_b)H - p_d(8L_bA_b + L_oA_o) \tag{3.34}$$

The total volume fraction of fiber in the RUC, V_f, is then given by:

$$V_f = \frac{p_d(8L_bA_b + L_oA_o)}{HL_b^2 \sin 2\theta_b} \tag{3.35}$$

Substitute Eq. (3.26) for the length L_b, and Eq. (3.29) for the length L_o, into Eq. (3.35) to get the total volume fraction of fibers in the RUC as (Eq. 11 in Ref. [9]):

$$V_f = \frac{p_d(4A_b \sin\theta_b + A_o \sin 2\theta_b)}{Hd_o \sin 2\theta_b} \tag{3.36}$$

Eq. (3.36) can be solved for H for given yarn packing density, p_d, braid angle, θ_b, axial yarn spacing, d_o, and after solving Eq. (3.25) for A_o and A_b.

3.2.3 Cross-sectional shapes of axial and braider yarn

Consider the cross section of the RUC along the centerline of a $+\theta_b$ braider yarn. This centerline is labeled A-B-C-D-E in Fig. 3.3 a) and the cross section is shown in Fig. 3.3 b). The projection of this centerline along a direction perpendicular to the axial yarn (or X-axis) coincides with the line labeled A'-B'-C-D'-E' shown in Fig. 3.3 a). The cross-section A'-B'-C-D'-E' is shown in Fig. 3.6. In this figure, the cross-sectional area of the axial yarn is a true area (not projected).

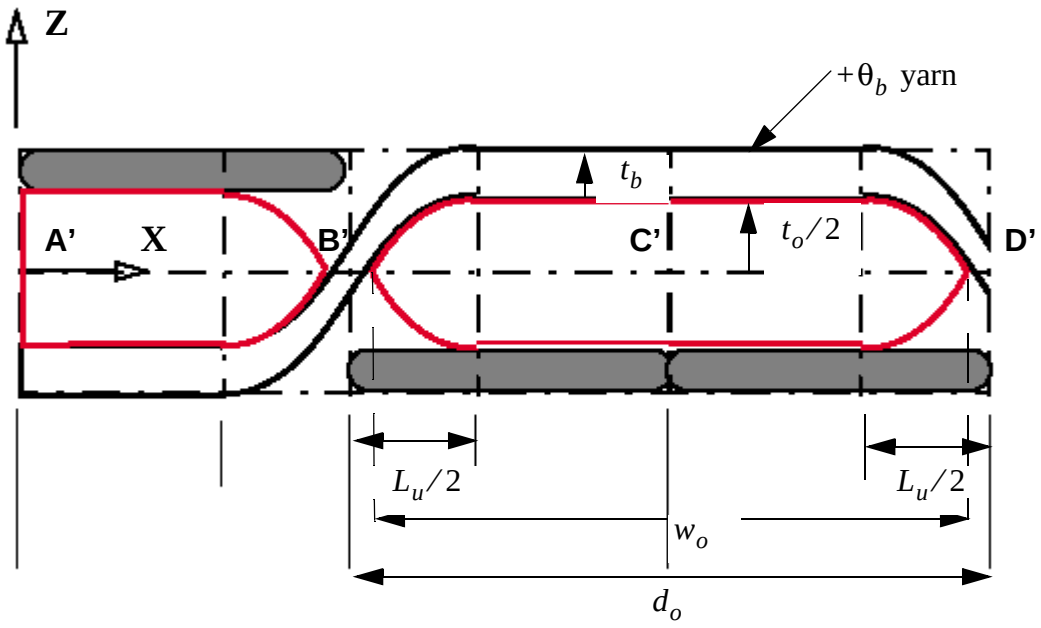

Fig. 3.6 Geometry of axial yarn cross-section

The equation of the centerline of the $+\theta_b$ braider yarn is then for $x \in [0, d_o]$:

$$z_c(x) = \begin{cases} \frac{t_o + t_b}{2} \sin\frac{\pi x}{L_u} & 0 \le x \le L_u/2 \\ \frac{t_o + t_b}{2} & L_u/2 \le x \le d_o - L_u/2 \\ -\frac{t_o + t_b}{2} \sin\frac{\pi(x - d_o)}{L_u} & d_o - L_u/2 \le x \le d_o \end{cases} \tag{3.37}$$

The equation for the curve corresponding to the bottom of the $+\theta_b$ yarn is thus obtained from this previous expression by a vertical shift of $-\frac{t_b}{2}$:

$$z_1(x) = \begin{cases} \frac{t_o + t_b}{2} \sin\left(\frac{\pi x}{L_u}\right) - \frac{t_b}{2} & 0 \le x \le L_u/2 \\ \frac{t_o}{2} & L_u/2 \le x \le d_o - L_u/2 \\ -\frac{t_o + t_b}{2} \sin\left(\frac{\pi(x - d_o)}{L_u}\right) - \frac{t_b}{2} & d_o - L_u/2 \le x \le d_o \end{cases} \tag{3.38}$$

As shown in Fig. 3.6 the tip of the axial yarn cross-section is aligned with the cross-over points of the braider yarn. This assumption determines what we call the “packaging constraint” for the axial cross-section area shape. This condition is fulfilled if $z_1\left(\frac{d_o - w_o}{2}\right) = 0$. We get:

$$\frac{t_o + t_b}{2} \sin\left(\frac{\pi(d_o - w_o)}{2L_u}\right) - \frac{t_b}{2} = 0 \tag{3.39}$$

From Eq. (3.39) we find:

$$\sin\left[\frac{(d_o - w_o)\pi}{2L_u}\right] = \frac{t_b}{t_o + t_b} \tag{3.40}$$

Define:

$$s = \operatorname{asin}\frac{t_b}{t_o + t_b} \tag{3.41}$$

and from Eq. (3.40) we get:

$$d_o - w_o = (2L_u s)/\pi \tag{3.42}$$

The upper part of the yarn cross sectional shape is assumed to follow the bottom curve of the braider yarn and its lower part is assumed to be symmetric with respect to the X-axis, such that the cross-sectional area of the axial yarn can be expressed as:

$$A_o = 2\int_{\frac{d_o - w_o}{2}}^{\frac{d_o + w_o}{2}} z_1(x)dx \tag{3.43}$$

This integration is derived in Appendix D.
Defining

$$V_s = t_o + t_b \tag{3.44}$$

we get from Eq. (3.43):

$$A_o = w_o t_o - L_u V_s\left[1 - \frac{2}{\pi}(s + \cos s)\right] \tag{3.45}$$

Eq. (3.45) is identical to Eq. 15 of Ref. [9]. Introducing the crimp angle β_c as the angle of the tangent to the sine function at x=0, with respect to the X-axis, we can express the undulating length, L_u, as a function of β_c:

$$L_u = \frac{\pi(t_o + t_b)}{2\tan\beta_c} \tag{3.46}$$

Also, introducing the yarn thickness ratio *m*:

$$m = \frac{t_o}{t_b} \tag{3.47}$$

we can then express the axial and braider yarn thickness as a function of *m* and *H*, from Eq. (3.30) we get:

$$t_b = \frac{H}{2+m} \qquad t_o = \frac{mH}{2+m} \tag{3.48}$$

Thickness H is determined through Eq. (3.36) for given yarn packing density, p_d, fiber volume fraction, V_f, braid angle, θ_b, axial yarn spacing, d_o, with areas A_o and A_b determined from Eqs. (3.25). The only two parameters left to be determined are thus *m* and β_c. Equation (3.45) gives us one equation to solve for *m* and β_c; we need one more equation to determine these two parameters. This equation is obtained by deriving the braider yarn cross-sectional area shape.

In order to keep the unknown parameters in the model to a minimum, the curved portion of the braider yarn cross-section (perpendicular to the yarn path), A_b, is assumed to be described by the same sinusoidal function as in Eq. (3.37), such that the upper curve of the braider yarn cross-section is described by the function:

$$z_u(x) = \begin{cases} \frac{t_o + t_b}{2}\sin\left(\frac{\pi x}{L_u}\right) & 0 \le x \le x_o \\ \frac{t_b}{2} & x_o \le x \le w_b - x_o \\ -\frac{t_o + t_b}{2}\sin\left(\frac{\pi(x - w_b)}{L_u}\right) & w_b - x_o \le x \le w_b \end{cases} \tag{3.49}$$

where x_o is the length of the undulating region as described in Fig. 3.7

.

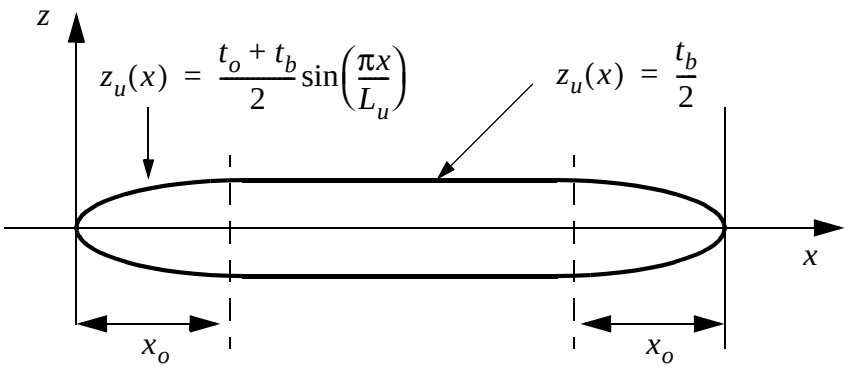

Fig. 3.7 Geometry of braider yarn cross-section

The condition for continuity for z_u at $x = x_o$ is given by $z_u(x_o^-) = z_u(x_o^+)$ which translates into:

$$\frac{t_o + t_b}{2}\sin\frac{\pi x_o}{L_u} = \frac{t_b}{2} \tag{3.50}$$

Solving Eq. (3.50) for x_o leads to:

$$x_o = \frac{L_u s}{\pi} \tag{3.51}$$

where s is defined by Eq. (3.41). Assuming that the cross-sectional area shape is symmetric with respect to the *x*-axis in Fig. 3.7 we can write:

$$A_b = 2\int_0^{w_b} z_u(x)dx \tag{3.52}$$

This integration is shown in Appendix D, we get:

$$A_b = w_b t_b - \frac{2}{\pi} L_u (t_b s - V_s(1 - \cos s)) \tag{3.53}$$

Equation (3.45) is identical to Eq. 16 of Ref. [9]. Now substitute Eq. (3.46) for L_u, Eq. (3.28) for w_b, Eq. (3.44) for V_s and Eq. (3.48) for t_o and t_b, into Eqs. (3.45) and (3.53) to express them as functions of *m*, *H*, β_c, *s*, d_o and θ_b only. We get:

$$A_o = \frac{H^2(1+m)}{(2+m^2)\tan\beta_c}\left[(1+m)\left(\cos s - \frac{\pi}{2}\right) + s\right] + \frac{d_o H m}{2+m} \tag{3.54}$$

$$A_b = \frac{H^2(1+m)}{(2+m^2)\tan\beta_c}[(1+m)(1-\cos s) - s] + \frac{d_o H \cos\theta_b}{2+m} \tag{3.55}$$

The two unknowns quantities in Eqs. (3.54) and (3.55) are the thickness ratio *m* and the crimp angle β_c. Eqs. (3.54) and (3.55) can be solved for these two parameters using a proper numerical scheme (e.g. fixed point iteration or Newton-Raphson).

3.2.4 Algorithm to determine the architecture parameters

The nonlinear equations describing the preform architecture are solved using an iterative procedure programmed in the Fortran language. The Fortran subroutine associated with these equations is called FINDM. The input parameters for the subroutine are listed in Table 3.4, and the output parameters are listed in Table 3.5.

Table 3.4: Input variables for subroutine FINDM

Variable	Description
n_o	filament count of axial yarn
n_b	filament count of braider yarn
d_f	diameter of a filament
p_d	yarn packing density
d_o	axial yarn spacing
V_f	fiber volume fraction of the RUC
TOL	tolerance on successive iterates of m
$imax$	maximum number of iterations

Table 3.5: Output variables for subroutine FINDM

Variable	Description
t_o	axial yarn thickness
t_b	braider yarn thickness
L_u	length of the undulation region
β_c	crimp angle
V_o	volume of the axial yarns in the RUC
V_b	volume of the braider yarns in the RUC
V	overall volume of the RUC
V_r	volume of the resin in one quarter of the RUC

An algorithm is developed to determine the thickness ratio *m* and the crimp angle β_c from Eqs. (3.54) and (3.55). The algorithm is based on a fixed point iteration scheme for *m* and β_c. The axial and braider yarn thicknesses, t_o and t_b, and the undulation length L_u are then updated using their corresponding expressions. The algorithm is as follows:

1. *Compute the cross-sectional area of axial and braider yarns, A_o and A_b, from Eq. (3.25) and solve Eq. (3.36) for H. Then start with initial guess for m: $m_{i=0} = m_o$, with $m_o > 1$.*

2. *Begin iteration loop: For $i = 1$ to $imax$ in steps of one.*

   2.a *Determine crimp angle value, $0 \le \beta_{c_{i-1}} \le \pi/2$, from given m_{i-1} through Eq. (3.55). The function atan being defined modulo π we can always find a root $\beta_{c_{i-1}}$ in this interval.*

   2.b *Take the smallest positive real root, and compute new value for m, $m_i = f(\beta_{c_{i-1}})$, through Eq. (3.54).*

   2.c *If $m_i < 1$, then STOP the program and send warning message. The aspect ratio of the fabric is changed somewhat and the model might be no longer valid.*

   2.d *Calculate the difference in the iterates using the measure* $\varepsilon = |m_i - m_{i-1}|$

   2.e *If $\varepsilon > TOL$, then increase the index $i \to i + 1$.*

   2.f *If $i \le imax$, then go to step 2.a.*

   2.g *If $i > imax$, then STOP and print non-convergence message.*

   2.h *If $\varepsilon < TOL$, then the fixed point iteration is judged to have converged to the thickness ratio $m = m_i$. Go to step 3.*

3. *Update all geometry parameters: t_o and t_b through Eq. (3.48), β_c through Eq. (3.55), then L_u through Eq. (3.46), V_o through Eq. (3.33), V_b through Eq. (3.32), V through Eq. (3.31) and finally V_r through Eq. (3.34).*

3.2.5 Determination of three-dimensional effective moduli

The derivation of three-dimensional effective stiffnesses follows the same reasoning as for the 2D braid. Based on an iso-strain assumption we can define an equivalent elasticity matrix for the RUC by

$$C_{eq} \equiv \frac{1}{V}\int_V C dV$$

The volume of the RUC is subdivided into the volume of the four $+\theta_b$ yarns, $4A_bL_b$, the four $-\theta_b$ yarns, $4A_bL_b$, the four axial yarns occupying a total volume of L_oA_o, and the volume of the resin matrix, V_r. As for the 2D braid, the equivalent elasticity matrix is the sum of the volume integral of the elasticity matrices over each phase. Using the small crimp angle approximation, we can write

$$C_{eq} = \frac{1}{V}\left\{4A_b\int_0^{L_b} C_{\theta_b}dx + 4A_b\int_0^{L_b} C_{-\theta_b}dx + A_o\int_0^{L_o} C_{ax}dx + \int_{V_r} C_{\text{resin}}dV\right\} \tag{3.56}$$

Eq. (3.56) can be re-written in the form

$$C_{eq} = v_{\theta_b}C_{eq\theta_b} + v_{-\theta_b}C_{eq-\theta_b} + v_{ax}C_{eqax} + v_rC_{eqr} \tag{3.57}$$

where the volume fractions of the $+\theta_b$ yarns, the $-\theta_b$ yarns, the axial yarn and the resin are given by

$$v_{\theta_b} = v_{-\theta_b} = 4A_bL_b/V \quad v_{ax} = A_oL_o/V \quad v_r = V_r/V = 1 - v_{\theta_b} - v_{-\theta_b} - v_{ax} \tag{3.58}$$

And the equivalent elasticity matrices for the $+\theta_b$ and $-\theta_b$ yarns in Eq. (3.57) can be expressed as:

$$C_{eq\theta_b} = \frac{1}{L_b}\int_0^{L_b} C_{\theta_b} dx = \frac{1}{L_b}\int_0^{L_b} C_1(\theta_b, \beta_{\theta_b}) dx \tag{3.59}$$

$$C_{eq-\theta_b} = \frac{1}{L_b}\int_0^{L_b} C_{-\theta_b} dx = \frac{1}{L_b}\int_0^{L_b} C_1(-\theta_b, \beta_{-\theta_b}) dx \tag{3.60}$$

where the elasticity matrix in the local *x-y-z* coordinate directions at a generic position in a yarn, is denoted by $C_1(\theta, \beta)$. The six-by-six matrix $C_1(\theta, \beta)$ is derived in Appendix B and given by Eq. (B.9).The angles of the centerlines of the $+\theta_b$ and $-\theta_b$ yarns with respect to the local x-axis are, respectively, determined by

$$\beta_{\theta_b} = \text{atan}\,(z'_{\theta_b}) \qquad \beta_{-\theta_b} = \text{atan}\,(z'_{-\theta_b}) \tag{3.61}$$

where the function z'_{θ_b} over one-half of the length of the $+\theta_b$ yarn is:

$$z'_{\theta_b} = \begin{cases} \dfrac{\pi(t_b + t_o)}{2L_u'}\cos\left(\dfrac{\pi x}{L_u'}\right) & x \in (0, L_u'/2) \\ 0 & x \in (L_u'/2, 2w_b' - L_u'/2) \\ -\dfrac{\pi(t_b + t_o)}{2L_u'}\cos\left(\dfrac{\pi(x - 2w_b')}{L_u'}\right) & x \in (2w_b' - L_u'/2, 2w_b' + L_u'/2) \\ 0 & x \in (2w_b' + L_u'/2, 4w_b' - L_u'/2) \\ \dfrac{\pi(t_b + t_o)}{2L_u'}\cos\left(\dfrac{\pi(x - 4w_b')}{L_u'}\right) & x \in (4w_b' - L_u'/2, 4w_b') \end{cases} \tag{3.62}$$

and the function $z'_{-\theta_b}$ over one-half of the length of the $-\theta_b$ yarn is:

$$z'_{-\theta_b} = \begin{cases} 0 & x \in (0,\ w_b' - L_u'/2) \\ \dfrac{\pi(t_b + t_o)}{2L_u'} \cos\left(\dfrac{\pi(x - w_b')}{L_u'}\right) & x \in (w_b' - L_u'/2,\ w_b' + L_u'/2) \\ 0 & x \in (w_b' + L_u'/2,\ 3w_b' - L_u'/2) \\ -\dfrac{\pi(t_b + t_o)}{2L_u'} \cos\left(\dfrac{\pi(x - 2w_b')}{L_u'}\right) & x \in (3w_b' - L_u'/2,\ 3w_b' + L_u'/2) \\ 0 & x \in (3w_b' + L_u'/2,\ 4w_b') \end{cases} \tag{3.63}$$

with $L_u' = L_u / \cos\theta_b$ (undulating length along the *x*-axis projected along the braider yarn path), $w_b' = w_b / \sin 2\theta_b$ (cross-sectional braider yarn width projected along the interlaced braider yarn path).

As the axial yarns are assumed to remain on a straight path, the equivalent elastic matrix for the axial yarns takes a very simple form:

$$C_{eqax} = \frac{1}{L_o} \int_0^{L_o} C_o dx = C_o \tag{3.64}$$

where C_o is the local stiffness matrix for the yarns as given in Appendix B obtained from the local compliance matrix, S_o, given by Eq. (B.3).

The resin is assumed to be homogeneous and isotropic, so its equivalent elasticity matrix is equal to its elasticity matrix evaluated point-wise; i.e.,

$$C_{eqr} = \frac{1}{V_{resin}} \int_{V_{\text{resin}}} C_{\text{resin}} dV = C_{\text{resin}} \tag{3.65}$$

This resin elasticity matrix is given by Eq. (B.10) in Appendix B. The integrations indicated in Eqs. (3.59) and (3.60) are done numerically using the trapezoidal rule in the FORTRAN program ‘tribraid.f’. This program uses the same subroutines as for the ‘exactplainweave.f’ program described in Appendix C, except for the GEOMET subrou-

tine which is replaced by the FINDM subroutine in order to determine the architecture parameters of the 2D triaxial braided composite.

3.2.6 Comparison with R.A. Naik[9] and J.G. Perez[23].

Effective moduli are computed for 2x2 2D triaxial braid examples from Ref. [9]. Results are obtained for three different triaxial braided composites taken from Ref. [14] and compared with TEXCAD analysis of Ref. [9] along with test data [14] and FEM results ([14], [22]). The yarn architecture parameters such as braid angle, braider and axial yarn sizes, axial yarn spacing and overall composite volume fraction for the three architectures (A1,B1,B2) are given in Table 3.6. These parameters along with a yarn packing density of 0.75 and a fiber diameter of 0.007mm are used as input for the Fortran program. The specimens in Ref.[14] are made with AS4 graphite fiber yarns and Shell 1895 epoxy resin and the yarn and resin material properties are assumed to be the same as those given in Table 2.4 on page 45.

Table 3.6: Different configurations of 2x2 2D triaxial braided composites from Ref. [14]

2-D triaxial braid	Braid angle, degrees	Braider yarn size, k	Axial yarn size, k	Axial yarn spacing, mm	Overall fiber volume fraction,%
A1	62.3	12	24	6.096	54.0
B1	67.4	6	18	5.320	51.2
B2	67.9	6	18	5.820	52.0

The results for the computed elastic constants and correlations with TEXCAD, test data and FEM results for each configuration are listed in Tables 3.7 and 3.8. The out-of-plane Poisson's ratios are also shown for information in Table 3.8 even though FEM and test data results do not allow to compute them.

Table 3.7: Comparison of results for moduli of 2x2 2D triaxial braided composites of Ref. [9]

Braid type	Approach	E_{xx}, GPa	E_{yy}, GPa	E_{zz}, GPa	G_{xy}, GPa	G_{zx}, GPa	G_{yz}, GPa
A1	TEXCAD [9]	45.14	40.10	10.42	14.84	4.64	4.13
	FEM ([14],[22])	53.16	46.95	-	-	-	-
	TEST[14]	45.44	45.64	-	-	-	-
	Present model	43.45	40.55	11.20	14.37	5.20	4.39
B1	TEXCAD [9]	48.42	42.48	10.13	11.07	4.40	3.90
	FEM ([14],[22])	62.12	47.51	-	-	-	-
	TEST[14]	44.47	45.16	-	-	-	-
	Present model	46.34	42.93	10.82	10.79	4.93	4.11
B2	TEXCAD[9]	50.42	42.63	10.23	11.08	4.31	3.90
	FEM([14],[22])	51.09	43.58	12.07	12.41	-	-
	TEST[14]	48.47	43.51	-	-	-	-
	Present model	48.57	43.09	10.89	10.85	4.79	4.11

Table 3.8: Comparison of results for Poisson's ratios of 2x2 2D triaxial braided composites of Ref. [9]

Braid type	Approach	ν_{xy}	ν_{xz}	ν_{yz}
A1	TEXCAD [9]	0.291	-	-
	FEM ([14],[22])	0.305	-	-
	TEST[14]	0.307	-	-
	Present model	0.277	0.332	0.258
B1	TEXCAD [9]	0.205	-	-
	FEM ([14],[22])	0.211	-	-
	TEST[14]	0.199	-	-
	Present model	0.196	0.362	0.288
B2	TEXCAD[9]	0.205	-	-
	FEM([14],[22])	0.214	-	-
	TEST[14]	0.190	-	-
	Present model	0.197	0.346	0.291

There is a good correlation of the three configurations A1, B1 and B2 with the TEX-CAD results obtained by R.A. Naik; however, a few discrepancies exist between the two sets of results as the geometrical iteration scheme differs between the two models. The results show also good correlation with the FEM and test data results even though further testing would be required to verify the results for the in-plane shear moduli and the

through-thickness properties. It is shown in Ref. [14] that the results for in-plane moduli (including G_{xy}) and Poisson's ratios using the present model correlate well with test data over a wide range of architecture parameters for 2x2, 2D triaxial braided composites. Parametric studies were also conducted in Ref. [9] and [14] to investigate the effects of fiber volume fraction, braid angle, yarn size, and axial yarn content on overall stiffness properties of triaxial braided composites.

A second comparison is made with J.G. Perez [23]. The architecture parameters of the preform such as braid angle, braider and axial yarn sizes, axial yarn spacing and overall composite volume fraction are listed in Table 3.9. These parameters along with a yarn packing density of 0.75 and a fiber diameter of 0.007mm are used as input for the Fortran program. The 2x2 2D triaxial braid of Ref. [23] is made with T-300 graphite fiber yarns and epoxy resin such that the yarn and resin properties are assumed to be the same as those given in Table 2.4 on page 45. The results are shown in Tables 3.10 and 3.11. As for the previous configurations, the results show a good correpondence between the present model and the results obtained with TEXCAD and a poorer, however satisfactory, correlation with the test data of Ref. [23].

Table 3.9: Input parameters for 2x2 2D triaxial braid from Ref. [23]

Braid angle, degrees	Braider yarn size, k	Axial yarn size, k	Axial yarn spacing, mm	Overall fiber volume fraction,%
64	6	18	5.3	55.26

Table 3.10: Comparison of moduli for 2x2 2D triaxial braided composite of Ref. [23]

Approach	E_{xx}, GPa	E_{yy}, GPa	E_{zz}, GPa	G_{xy}, GPa	G_{zx}, GPa	G_{yz}, GPa
Test data [23]	48.88	-	-	-	-	-
TEXCAD [9]	45.44	48.68	10.55	13.17	4.45	4.14
Present model	43.93	49.14	11.30	12.87	4.94	4.39

Table 3.11: Comparison of Poisson's ratios for 2x2 2D triaxial braided composite of Ref. [23]

Braid type	Approach	ν_{xy}	ν_{xz}	ν_{yz}
Reference [23]	Test data [23]	0.26	-	-
	TEXCAD [9]	0.21	0.30	0.26
	Present model	0.20	0.33	0.27

3.2.7 Limitations

The geometry of triaxially braided composites is troublesome because of the rather complicated shape of both the axial and braider yarn cross-sections as shown in Fig. 3.8. The equations that we derived to compute the cross-sectional shapes of the braider and axial yarns are based on simplified assumptions which do not take into account spacing between axial yarns. The shape of the axial yarn cross-section and the size of the undulat-

ing region in Fig. 3.6 are not captured accurately, especially for high braid angles where the presence of gaps between adjacent axial yarns can not be neglected (Fig. 3.8 b)). Also, during the resin impregnation process, the three sets of yarns are compressed together and form a disorganized pattern (Fig. 3.8 c)) which can not be modeled without making restrictive assumptions. The derivation of the braider yarn cross-sectional shape is also based on arbitrary assumptions that do not allow to capture the various possibilities of shapes resulting from the manufacturing process. Moreover, the mathematical restrictions that may apply to the equations related to the derivation of yarn thickness ratio *m* and crimp angle β_c, Eqs. (3.54) and (3.55), have been neglected as they involve complex mathematical considerations. As a result, the current model is restricted to the range $0 < \theta_b < 69°$. The fixed point iteration scheme to determine *m* and β_c would not converge for braid angles greater than 69°. Other numerical schemes were used to solve these equations, but none of them would converge for greater values than 69°. Increasing the range of application of the Fortran program would require further investigation of the mathematical equations related to the geometry. However, a literature review showed that few examples are documented for braid angles greater than 69°. Thus, the model remains valid for a wide range of configurations.

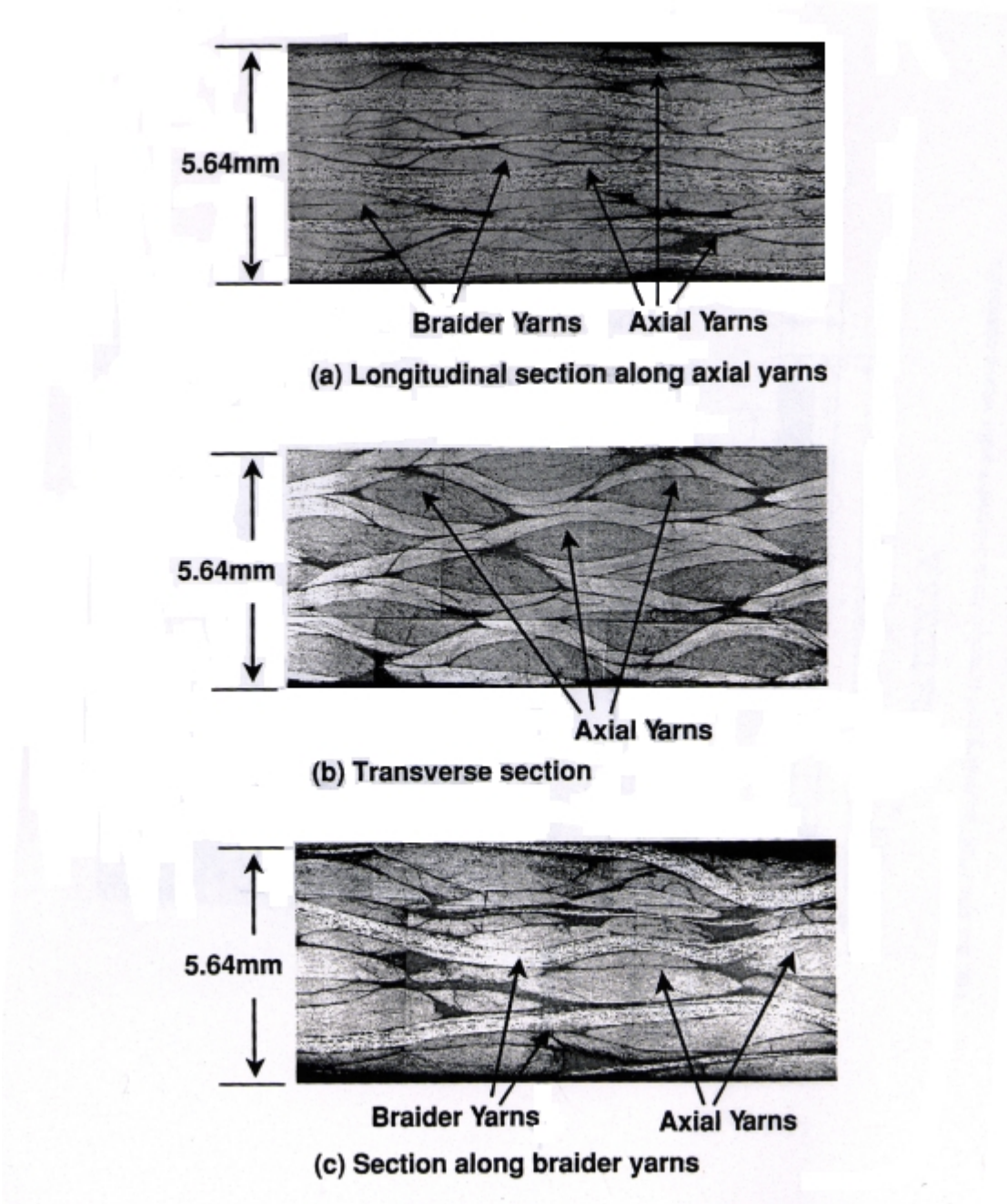

Fig. 3.8 Typical cross-sectional micrographs of 2x2 2d triaxial braided composites from Ref. [9]

3.3 Concluding Remarks

The 2D braid composite architecture didn't present any difficulties in the sense that its derivation was based on the exact same equations as those given by R.A. Naik in Ref. [9]. The results for the moduli were therefore similar to those given in Ref. [9]. Our model confirmed the effects of braid angle on the mechanical properties of the 2D braided composites predicted by R.A. Naik and showed that the model compared very well with FEM results [22].

The geometry of the 2x2 2D triaxial braid composite was more difficult to apprehend because of its complex architecture as shown in Fig. 3.8. However, the detailed rederivation of R.A. Naik's equations from Ref. [9], along with the proper corresponding assumptions, and their implementation in FORTRAN allowed us to measure the limitations of this model.

For the 2D triaxial braid examples taken from Ref. [9] and [23], the model showed a good correlation with test data, FEM and TEXCAD results. The presence of axial yarns in the triaxially braided composites leads to a good balance between on- and off-axis properties. Indeed, for a braid angle of 67°, the values of the in-plane moduli for a 2D braided fabric were evaluated as $E_{xx} \sim 70GPa$ and $E_{yy} \sim 11GPa$ while for the same value of braid angle, the in-plane moduli for a 2x2, 2D triaxial braid were $E_{xx} \sim 50GPa$ and $E_{yy} \sim 43GPa$.

The introduction of additional longitudinal yarns into the braided fabric permits to obtain a large range of properties while varying geometrical parameters such as the braid angle, the axial and braider yarn filament counts or the overall fiber volume fraction. Triaxially braided composites are thus well suited for structural applications in the automotive and aerospace industry and can be found in various structures that require torsional stiffness and strength.

Chapter 4. 4x4 Twill Fabric

4.1 Analytical Model

4.1.1 Geometric modeling

A 4x4 twill fabric consists of two sets of orthogonal interlaced yarns, called warp and fill, where the warp yarns alternately weaves over and under four fill yarns in a regular repeated manner. This produces the visual effect of a straight or broken diagonal ‘rib’ to the fabric as shown in Fig. 4.1. Twill weaves often exhibit better drapability than plain weave. With reduced crimp, the fabric also has a smoother surface and slightly greater in-plane mechanical properties.

The representative unit cell is made of 16 yarns, 8 warps and 8 fills, and is described in Fig. 4.1. The analytical model is based upon the same assumptions than those of the plain weave fabric, including the small crimp angle approximation. It is assumed that the spacing between the warp and fill yarns is the same and that there is no gap between adjacent yarns. The yarn spacing is denoted by a which is the also the yarn width. As a result the planform dimension of the RUC is $8a$ x $8a$. If we denote its thickness dimension by H, the overall volume of the RUC becomes then:

$$V = 64a^2H \tag{4.1}$$

Assuming the warp and fill yarns have the same filament count, n, and filament diameter, d_f, the unknown cross sectional area A for the yarns is given by Eq. (2.1) on page 17. The sectional view in Fig. 4.2 (section A-A of Fig. 4.1) shows the undulation of a warp yarns as it crosses over and under the fill yarns. The yarn path for each yarn in the RUC consists of straight portions and undulating portions where the yarns are assumed to follow a sinu-

soidal path. The equation of the yarn centerline, z_c, centered at a cross-over point is thus expressed as:

$$z_c(x) = \pm\frac{t}{2}\sin\left(\frac{\pi x}{L_u}\right) \tag{4.2}$$

The cross-sectional shape for the yarns can be derived in a similar manner as for the plain weave in the case of small crimp angle. If we denote L_u the length of the undulating region and *t* the yarn thickness, the cross-sectional area *A* is expressed as:

$$A = at - L_u t\left(1 - \frac{2}{\pi}\right) \tag{4.3}$$

The projected length, L_p, of the yarn path for each yarn is a function of the yarn spacing, *a*, and is given by $L_p = 8a$. the volume occupied by the 16 yarns within the RUC is then $16AL_p$. The overall fiber volume fraction can thus be derived as:

$$V_f = \frac{2p_d A}{Ha} \tag{4.4}$$

Eqs. (4.3) and (4.4) are equivalent to Eq. (2.39) on page 28. The basic equations for the preform architecture are thus very similar to those of the plain weave, only the number of yarns and thus the volume over which we integrate the stiffnesses is changed somewhat. Equations (4.3) and (4.4) can be solved numerically along with Eq. (2.1) on page 17 to determine the unknown parameters *A*, *t* and L_u.

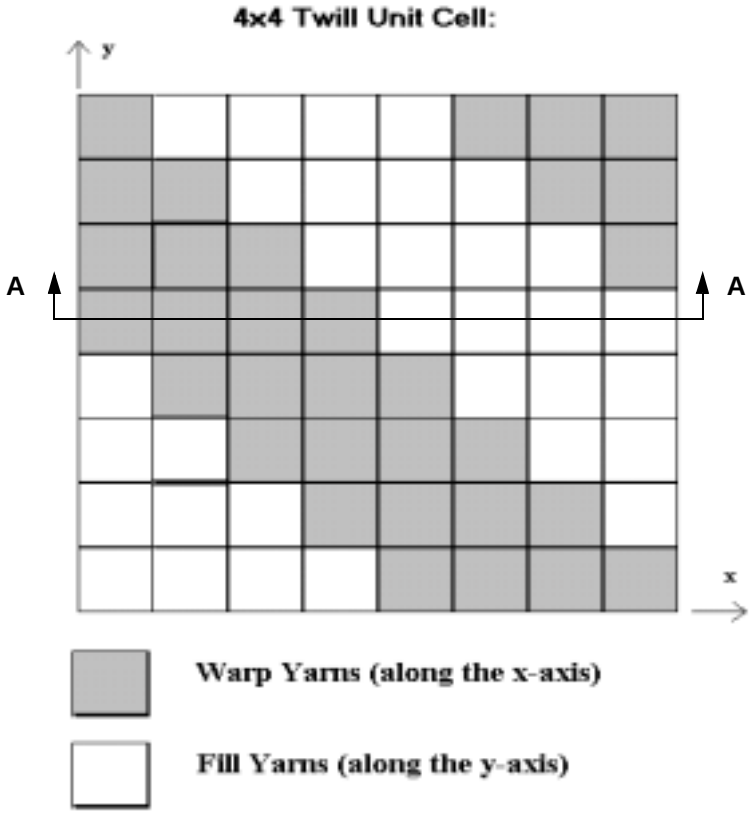

Fig. 4.1 Representative unit cell for the 4x4 twill architecture.

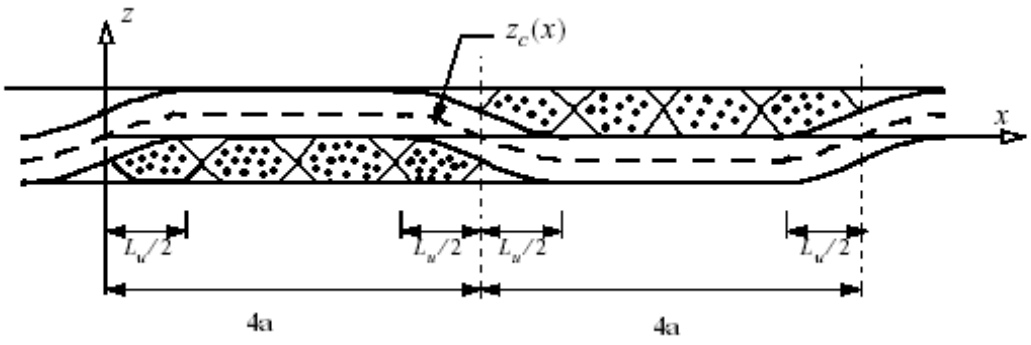

Fig. 4.2 Cross-sectional area shape for section A-A of Fig. 4.1

4.1.2 Calculation of three-dimensional effective stiffnesses

For the purpose of calculating overall properties, the RUC is assumed to be composed of three linear elastic phases: eight warp yarns, eight fill yarns, and resin matrix. A stress averaging technique based on an iso-strain assumption is used to define an equivalent elasticity matrix C_{eq} for the RUC, such that $C_{eq} \equiv \frac{1}{V}\int_V C dV$. Following a procedure similar to the plain weave and 2D braid fabrics, the equivalent elasticity matrix can be written as the sum of the volume integral of the elasticity matrices over each phase. That is,

$$C_{eq} = \frac{1}{V}\left\{ 8A\int_0^{L_p} C_w\, dx + 8A\int_0^{L_p} C_f\, dy + \int_{V_{\text{resin}}} C_{\text{resin}}\, dV \right\} \tag{4.5}$$

where $C_w = C_1(0, \beta_w)$ corresponds to the local stiffness matrix of the warp yarns, and $C_f = C_1(0, \beta_f)$ corresponds to the local stiffness matrix of the fill yarns. Note that the integrations of the local stiffness matrices for both the fill and warp yarns in Eq. (4.5) are independent of the path of the warp and fill yarns. Each warp and fill yarns consist indeed of two or three straight portions of total length $8a - 2L_u$ and two or three undulating regions of total length $2L_u$. As a result, the effective stiffness matrix for the RUC is somewhat independent of the pattern described in Fig. 4.1. The angles of the centerlines of the warp and fill yarns with respect to the local x-axis are, respectively, determined by:

$$\beta_w = \text{atan}\,(z'_w) \qquad \beta_f = \text{atan}\,(z'_f) \tag{4.6}$$

where z_w and z_f are, respectively, the warp and fill yarns centerline path equations. For the warp yarn of section A-A in Fig. 4.2, for example, z_w can be written as:

$$z_w(x) = \begin{cases} \frac{t}{2}\sin\frac{\pi x}{L_u} & 0 \le x \le L_u/2 \\ \frac{t}{2} & L_u/2 \le x \le 4a - L_u/2 \\ -\frac{t}{2}\sin\frac{\pi(x-4a)}{L_u} & 4a - L_u/2 \le x \le 4a + L_u/2 \\ -\frac{t}{2} & 4a + L_u/2 \le x \le 8a - L_u/2 \\ \frac{t}{2}\sin\frac{\pi(x-8a)}{L_u} & 8a - L_u/2 \le x \le 8a \end{cases} \tag{4.7}$$

Equivalent matrices are then computed for each phase, such that we can write:

$$C_{eqw} = \frac{1}{L_p}\int_0^{L_p} C_1(0, \beta_w)dx \tag{4.8}$$

$$C_{eqf} = \frac{1}{L_p}\int_0^{L_p} C_1(0, \beta_f)dy \tag{4.9}$$

$$C_{eqr} = \frac{1}{V_{resin}}\int_{V_{\text{resin}}} C_{\text{resin}}dV = C_{\text{resin}} \tag{4.10}$$

with:

$$C_{eq} = v_w C_{eqw} + v_f C_{eqf} + v_r C_{eqr} \tag{4.11}$$

where the volume fractions of the $+\theta_b$ yarns, the $-\theta_b$ yarns, and the resin are given by

$$v_w = v_f = (8AL_p)/V \qquad v_r = V_{\text{resin}}/V = 1 - v_w - v_f \tag{4.12}$$

Similarly to other architectures, the integrations indicated in Eqs. (4.8) and (4.9) are done numerically using the trapezoidal rule in the FORTRAN program ‘twill.f’. This program is based on the same subroutines as for the ‘exactplainweave.f’ program described in Appendix C except for the GEOMET subroutine which is not used in the case of small

crimp angle approximation. The architecture parameters are thus computed directly from the equations of Section 4.1.1 on page 109.

4.2 Results

Effective moduli are computed for a T-300 carbon/epoxy 4x4 twill composite using the same geometric parameters as for the plain weave example from Ref. [9]: a yarn spacing $a = 1.411\text{mm}$, an overall fiber volume fraction $V_f = 0.64$, a yarn packing density $p_d = 0.75$, and a diameter of fiber $d_f = 0.007\,\text{mm}$ are thus considered. The yarn and resin properties are those given in Table 2.4 on page 45. Figure 4.3 shows the variations of three-dimensional elastic constants for the plain weave composite example from Ref. [9] with respect to the yarn filament count (or yarn size), *n*. Figures 4.4 and 4.5 show the results obtained for the 4x4 twill composite moduli, crimp angle and Poisson's ratios using the same geometric input parameters.

Figures 4.3, 4.4 and 4.5 show that the 4x4 twill has smaller out-of-plane moduli and Poisson's ratios than the plain weave for which the periodic waviness of the yarns has greater values. The crimp angle has the same values as the two models are based on the same geometry, but the larger straight portion in the 4x4 twill reduces the values of the effective out-of-plane properties.

On the other hand, the in-plane properties have greater values for the 4x4 twill, especially for larger values of the yarn filament count *n*. For example, for n=18000, the in-plane Young modulus for the 4x4 twill is $E_{xx} = 68GPa$, while for the plain weave the value decreases to $E_{xx} = 50GPa$. The in-plane properties of the 4x4 twill are thus reinforced by the larger length of the straight portion.

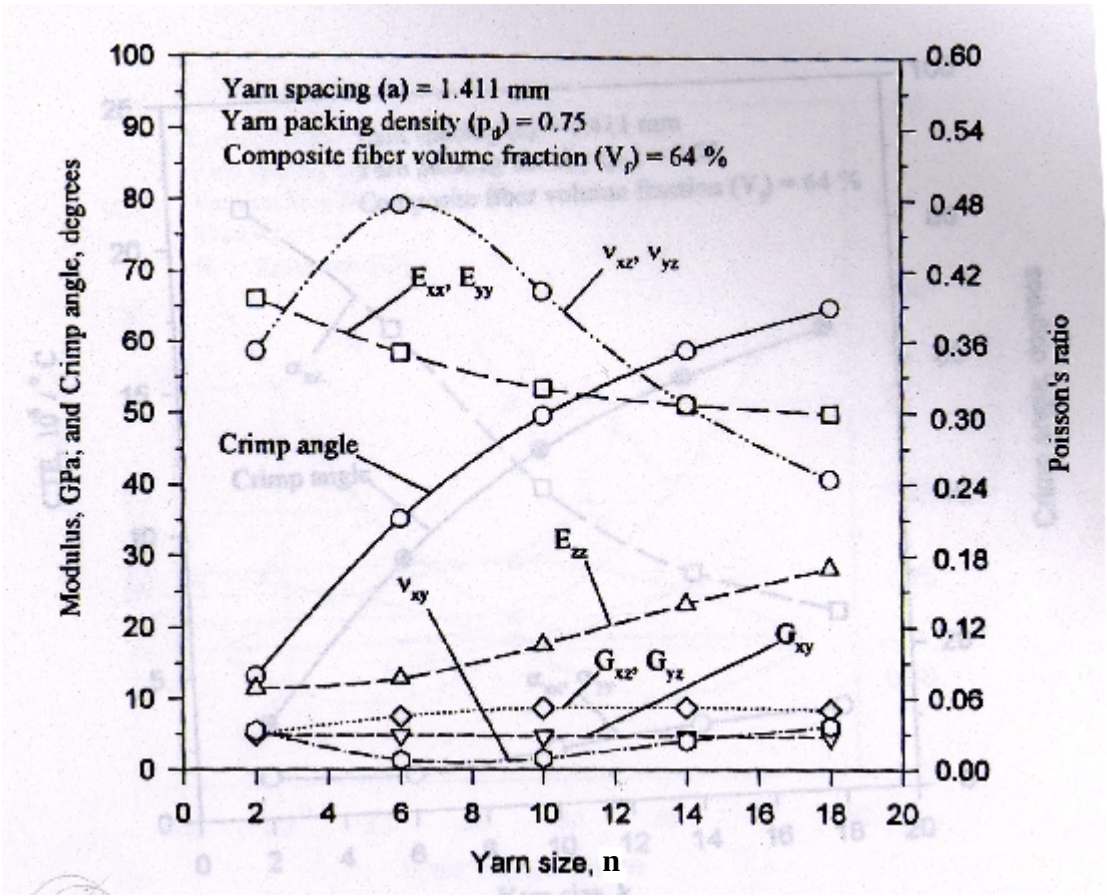

Fig. 4.3 Variation of effective moduli, Poisson's ratios and crimp angle with respect to yarn size for plain weave fabric example of Ref. [9]

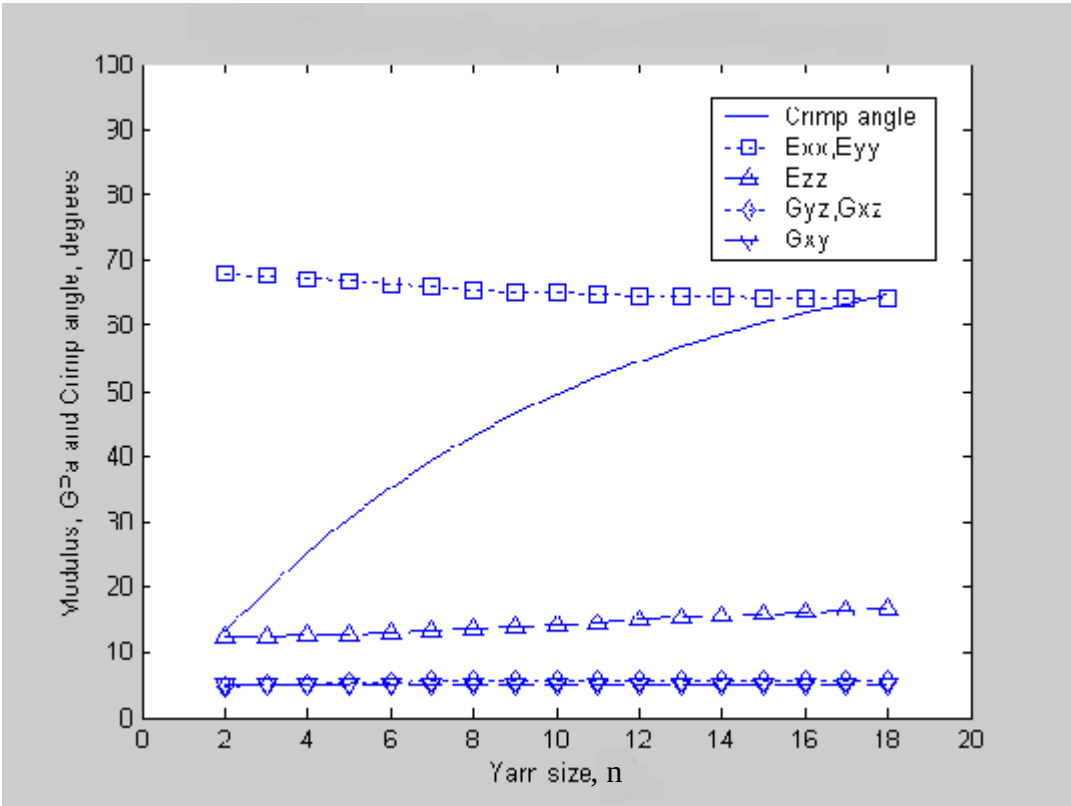

Fig. 4.4 Variation of 4x4 twill effective moduli and crimp angle with respect to yarn size for a=1.411mm, Vf=64% and pd=0.75

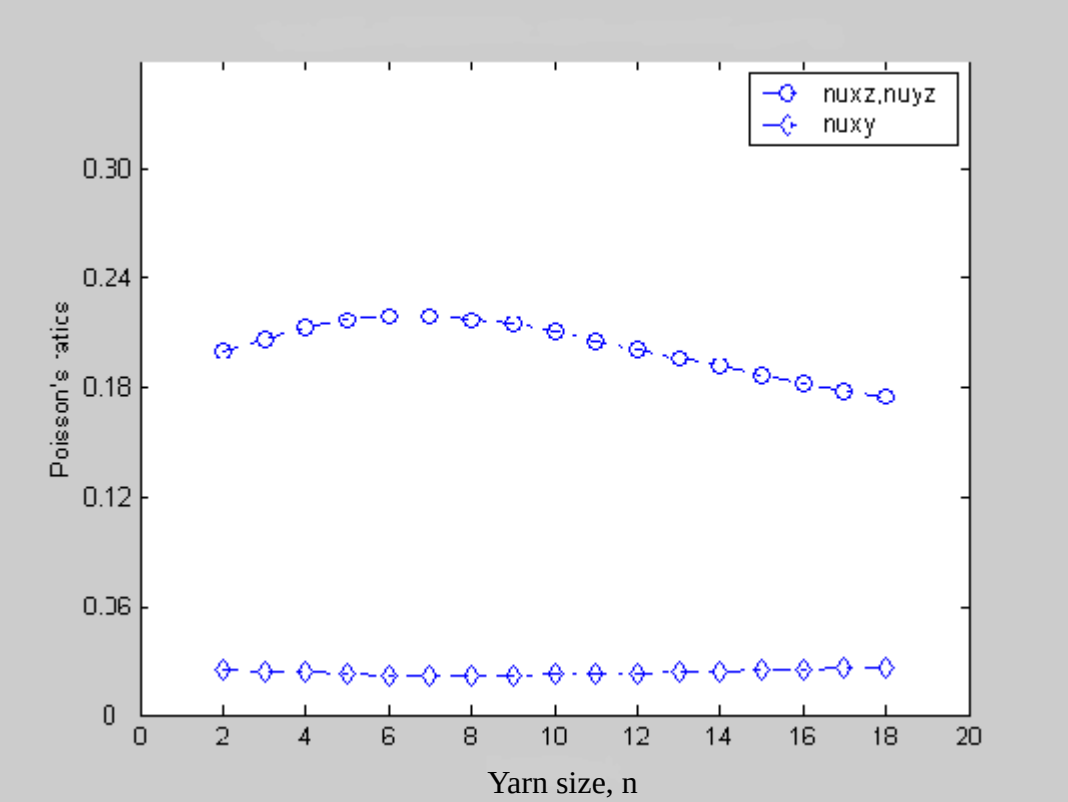

Fig. 4.5 Variation of 4x4 twill Poisson's ratios with respect to yarn size for a=1.411mm, Vf=64% and pd=0.75

4.3 Experimental Measurement of Fiber Volume Fraction

Being certain of fiber volume fraction is a critical issue in running predictive effective moduli codes. Indeed, one of the essential geometrical characteristics upon which the elastic constants depend, is the average fiber volume fraction, V_f. Generally the best guide to fiber volume fraction is an experimental measurement as volume fractions predicted a-priori from the manufacturer's specifications for a textile preform are vulnerable to error.

To measure the fiber volume fraction of a Toray T-300/Epoxy 4x4 twill composite, different samples of the composite were weighted dry, w_d, then wet, w_w. Then Archimedes' principle was applied to determine the buoyant force on the composite sample:

$$F = w_d - w_w = \Delta w \tag{4.13}$$

Through Archimedes' principle, this buoyant force on the sample was equal to the weight of the displaced fluid. As we weighed the composites in water, the weight of the displaced fluid was given by:

$$F = \rho_{H_2O} \cdot V_c \tag{4.14}$$

where $\rho_{H_2O} = 1 g/cc$ is the density of the water and V_c is the volume of the composite sample. Volume V_c can be expressed in terms of the composite density, ρ_c, and the dry weight of the composite, w_d, as:

$$V_c = w_d / \rho_c \tag{4.15}$$

Replacing V_c in Eq. (4.14) by its value in Eq. (4.15) and then substituting F in Eq. (4.13) leads to:

$$\rho_c = \frac{w_d}{w_d - w_w} \rho_{H_2O} \tag{4.16}$$

Finally a rule of mixture was applied, using the overall density of the composite, ρ_c, the density of the fibers, ρ_f, and the density of the resin, ρ_r, to get the fiber volume fraction V_f:

$$\rho_c = \rho_f V_f + \rho_r (1 - V_f) \tag{4.17}$$

Or in terms of V_f:

$$V_f = \frac{\rho_c - \rho_r}{\rho_f - \rho_r} \tag{4.18}$$

Table 4.1 lists the results obtained on 3 samples.

Table 4.1: Fiber volume fraction measurements for different Toray T-300/Epoxy 4x4 twill samples. Density of resin: 1.2 g/cc. Density of fiber: 1.76 g/cc. Density of water: 1.0 g/cc.

Sample n°	Weight dry	Weight wet	Delta weight	Density of composite[a]	Fiber volume fraction V_f.[b]
1	0.7797	0.2495	0.5302	1.470577	0.483173
2	1.2639	0.407	0.8569	1.474968	0.491014
3	1.1808	0.3815	0.7993	1.477293	0.495165

a. using Eq. (4.16)
b. using Eq. (4.18)

The average value was determined as: $V_f = 0.489784$ which is very close to the 49% given by the manufacturer. The standard deviation obtained on the average value for the fiber volume fraction was about 0.6%, which is fairly good.

4.4 Concluding Remarks

A procedure similar to the plain weave approach has allowed us to derive equations for the geometry of the 4x4 twill fabric as well as for the elastic constants of the representative unit cell. The homogenization method, on which these equations are based, thus appears to be a powerful and effective tool to compute three-dimensional effective moduli of a wide range of textile structural composites for which we can define a specific geometric modelization.

Effective moduli for a 4x4 twill composite have been compared to a plain weave composite with equivalent material properties and identical geometrical input parameters. The variations of the elastic constants with respect to the yarn filament count for both the 4x4 twill and the plain weave geometry are shown in Figures 4.3, 4.4 and 4.5. Results showed that the 4x4 twill fabric exhibits less out-of-plane moduli with respect to the plain weave configuration, but that the rather larger straight portion in the 4x4 twill RUC results in larger in-plane moduli with respect to the plain weave.

Chapter 5. Progressive Failure Analysis

5.1 Introduction

The first part of the project consisted in developing numerical constitutive models which approximated the mechanical response of specific textile composite materials at the local scale. In order to implement these constitutive models in the ABAQUS structural analysis software system, we had to move to the second phase which consisted in creating user defined subroutines, called UMAT, from the Fortran programs for the effective moduli. These subroutines, in correlation with ABAQUS analysis procedures, allowed us to define an incremental finite element approach to progressive failure. The last phase of the project was then to determine a material failure mechanism theory for the balanced plain weave architecture and implement this model into a specific UMAT.

5.2 UMAT Specifications

UMATs are user-written material subroutines in Fortran language that allow a definition a material's mechanical behavior. They are called in the ABAQUS analysis process at all material calculation points of elements for which the material definition includes the USER MATERIAL option. Most of the specifications for user material subroutines can be found in the ABAQUS/Standard user's manual; however, it seems judicious to recall the principal features of UMAT subroutines in order to clarify some essential notions.

A basic concept in ABAQUS is the division of the problem history into steps, or time increments. During the analysis the state variables (displacement field, strain and stress arrays, etc.) must be updated from one step to another according to the constitutive model. The UMAT subroutines must thus provide the material Jacobian matrix for each step *i*,

$J_i = \partial\Delta\sigma_i/\partial\Delta\varepsilon_i$ [1], where $\Delta\sigma_i$ are the stress increments and $\Delta\varepsilon_i$ are the strain increments at the *i*th step. $J_i(j, k)$ thus defines the change in the *j*th stress component at the end of the time increment caused by an infinitesimal perturbation of the *k*th component of the strain increment array $\Delta\varepsilon_i$ at the *i*th step. Also, for a specific strain increment, $\Delta\varepsilon_i$, the subroutine must output the updated stress tensor at the end of the increment, σ_i, from its value at the beginning of the increment, σ_{i-1}, such that: $\sigma_i = \sigma_{i-1} + J_i \cdot \Delta\varepsilon_i$.

Also, many of the constitutive models in ABAQUS require tensors to be stored, to define the state at a material calculation point. Among the variables to be defined by the UMAT, STATEV is an array that contains the solution-dependent state variables. To determine the failure ‘state’ or modes of the different yarns within the RUC we will thus use this tensor to store the information at all material calculation points. STATEV is passed in as the value at the beginning of the increment, unless it is updated in user-subroutines USFLD, and must be returned as the value at the end of the increment.

5.3 Balanced Plain Weave Failure Model

5.3.1 Prediction of failure within the yarns

The architecture of a textile composite is complex and, therefore, the parameters controlling its strength properties are numerous. The present study is an attempt to model with reasonably simple assumptions the progressive structural failure of a balanced plain weave composite. Prediction of failure at each incremental step is obtained by using a qua-

1. Note that the ordering of the components of the stress and strain tensors are changed somewhat in ABAQUS. τ_{12} and τ_{23} are permuted in ABAQUS ($\bar{\sigma} = [\sigma_1, \sigma_2, \sigma_3, \tau_{12}, \tau_{13}, \tau_{23}]$) such that we have to use a permutation matrix, to get the Jacobian matrix out of the equivalent stiffness matrix that we computed in Chapter 2.

dratic failure criterion (described later) applied to the local strains along with a stiffness and strength reduction scheme to account for damage within the yarns. The theory accounts for failure within the yarns but does not consider delamination phenomena at the interface between the yarn and the resin system within the RUC.

Recall that the RUC for the balanced plain weave fabric is made of four yarns, two warp and two fill, interlacing at right angle (see Fig. 2.1). The orthogonal, on-axis directions at an arbitrary point in a yarn are denoted as 1-2-3, where the 1-axis is parallel to the fibers, and the 2- axis is normal to the 1-axis and *z*-axis of the RUC. The 1-2-3 coordinate system is obtained from the global *x*-*y*-*z* coordinate system by rotating it consecutively through an angle θ about the z-axis ($(x, y, z) \rightarrow (x_1, y_1, z_1)$) and an angle β about the y_1-axis ($(x_1, y_1, z_1) \rightarrow (1, 2, 3)$) as described in Appendix B (Fig. B.1).

Each yarn consist of straight and undulation portions, and are treated locally as unidirectional laminates with transversely isotropic mechanical properties. This assumption allows us to select a laminated composite failure theory to apply to the local strains within the yarn. Many material failure theories are available in the literature, but we selected the theory by Tsai [20] to account for the progressive degradation of the strengths and stiffnesses of the yarns.

Following the lamina theory by Tsai, we can define five basic material strengths for the yarns as presented in Table 5.1.

Table 5.1: Local material strengths for the yarns

Name	Description
X_t	Tensile strength in the fiber direction
X_c	Compressive strength in the fiber direction
Y_t	Tensile strength in the transverse direction
Y_c	Compressive strength in the transverse direction
S	In-plane longitudinal shear strength

Let ε_0 denote the six-by-one vector of engineering strains in the on-axis system, $\varepsilon_0^T = \left[\varepsilon_1\ \varepsilon_2\ \varepsilon_3\ \gamma_{23}\ \gamma_{31}\ \gamma_{12}\right]$, or in contracted notations, $\varepsilon_0^T = \left[\varepsilon_1\ \varepsilon_2\ \varepsilon_3\ \varepsilon_4\ \varepsilon_5\ \varepsilon_6\right]$.We can then express the Tsai-Wu quadratic criterion in strain space as a function of the material strengths and ε_0. Assuming that the CLT assumptions are applicable locally for the yarns and that thus, the yarns are locally in a state of plane stress and that the Kirchhoff hypothesis apply to the local displacement field, the scalar equation in strains can be expressed as follows (see Tsai p.8-13):

$$G_{ij}\varepsilon_i\varepsilon_j + G_i\varepsilon_i = 1,\ \text{i=1,2,6} \tag{5.1}$$

when expanded:

$$G_{11}\varepsilon_1^2 + 2G_{12}\varepsilon_1\varepsilon_2 + G_{22}\varepsilon_2^2 + G_{66}\varepsilon_6^2 + G_1\varepsilon_1 + G_2\varepsilon_2 = 1 \tag{5.2}$$

where $G_{11} = F_{11}Q_{11}^2 + 2F_{12}Q_{11}Q_{12} + F_{22}Q_{22}^2$,

$G_{22} = F_{11}Q_{12}^2 + 2F_{12}Q_{12}Q_{22} + F_{22}Q_{22}^2$, $G_{12} = F_{11}Q_{11}Q_{12} + F_{12}(Q_{11}Q_{22} + Q_{12}^2)$,

$G_{66} = F_{66}Q_{66}^2$, $G_1 = F_1Q_{11} + F_2Q_{12}$ and $G_2 = F_1Q_{12} + F_2Q_{22}$.

The strength parameters $[F]$ are given as function of the material strength:

$$\begin{aligned} F_{11} &= \frac{1}{X_t X_c} & F_1 &= \frac{1}{X_t} - \frac{1}{X_c} \\ F_{22} &= \frac{1}{Y_t Y_c} & F_2 &= \frac{1}{Y_t} - \frac{1}{Y_c} \\ F_{66} &= \frac{1}{S^2} \end{aligned} \tag{5.3}$$

The interaction term F_{12} can only be determined from a combined-stress test, which is difficult to perform. F_{12} is thus often treated as an empirical constant. In the Tsai-Wu criterion it is usually normalized by:

$$F_{12} = \frac{F_{12}^*}{\sqrt{X_t X_c Y_t Y_c}} \tag{5.4}$$

where $-1 \le F_{12}^* \le 1$. In the program we take the generalized von Mises value: $F_{12}^* = -\frac{1}{2}$.

The reduced stiffnesses for the yarns in local coordinate system are obtained from the yarn five independent material properties (see Appendix B) (obtained through self-consistent model or rule of mixture) by:

$$\begin{aligned} Q_{11} &= E_1/(1-\nu_{12}\nu_{21}) & Q_{22} &= (E_2/(1-\nu_{12}\nu_{21})) \\ Q_{12} &= \nu_{21} Q_{11} = \nu_{12} Q_{22} & Q_{66} &= E_6 = G_{12} \end{aligned} \tag{5.5}$$

5.3.2 Material degradation model

Once the Tsai-Wu criterion is formulated in terms of the local strains using the material strengths and reduced stiffnesses in each yarn, failure is detected if the left hand side of Eq. (5.1) exceeds 1. We then need a stiffness and strength reduction scheme to account for yarn damage throughout the RUC.

Tsai developed a simple method to account for degradation of lamina strength and stiffness, that was successfully implemented in a study of an energy-absorbing structure by Woodson [25]. He assumed two types of material degradation within the composite lamina based on the sign of the local (on-axis) transverse normal strain (perpendicular to the fiber direction). Following a similar method, we then define two failure modes - matrix or fiber - associated with the local degradation of the yarns, such that:

1. *If the transverse strain, ε_2, is positive, and there are no prior failure to this yarn, the event is assumed to be a matrix failure, and a material degradation model which primarily reduces the transverse strength and stiffness is applied.*

2. *If the transverse strain, ε_2, is negative, or a prior failure has occurred in this lamina, the event is assumed to be a fiber failure, and an alternate material degradation model which also reduces the axial stiffness is applied.*

A matrix failure can precede a fiber failure but fiber failure is only allowed to occur once per yarn. The second indication of a fiber failure in any yarn is interpreted as ultimate failure and the strength and stiffnesses are not degraded further. As a result, each yarn can be either in one of the four failure states: (1) No failure; (2) Matrix failure; (3) Single fiber failure; (4) Matrix failure followed by fiber failure (ultimate failure). By symmetry, the two warp yarns (respectively fill yarns) are in the same failure state and we can reduce the failure analysis to one single warp (respectively fill) yarn. The information on the warp and fill yarns failure states are contained in the two-by-one array STATEV, the first row corresponding to the warp yarn and the second row to the fill yarn. SATEV can take four different integer values related to the four failure states: STATEV(1 or 2)=1, 2, 3 or 4.

To degrade the stiffnesses and strengths for each failure mode, we consider the empirical constants used in Tsai's model and given in Table 5.2. Constants E_m^* and E_f^* are, respectively, the matrix and fiber degradation factors, η_2 and η_{12} are the stress partitioning parameters, which account for different fiber and matrix stresses at the

micromechanical level, and n is a constant that governs the reduction in axial compressive strength X_c.

Table 5.2: Empirical constants for yarn degradation factors from Ref. [20]

Empirical constant	Value
E_m^*	0.15
E_f^*	0.01
η_2	0.5161
η_{12}	0.3162
n	0.1

A modified rule of mixtures is used to determine the loss of transverse yarn stiffness and in-plane shear stiffness due to material degradation. For both matrix and fiber failure modes, the degraded properties are given by Eqs. (5.6) and (5.7).

$$\frac{1}{E_2^{\text{degraded - m}}} = \frac{1}{(1+\nu_2^*)}\left[\frac{1}{E_{f2}} + \frac{\nu_2^*}{E_m^* E_m}\right]$$
$$\frac{1}{G_{12}^{\text{degraded - m}}} = \frac{1}{(1+\nu_{12}^*)}\left[\frac{1}{G_{f12}} + \frac{\nu_{12}^*}{E_m^* E_m}\right] \tag{5.6}$$

$$\frac{1}{E_2^{\text{degraded - f}}} = \frac{1}{(1+\nu_2^*)}\left[\frac{1}{E_{f2}} + \frac{\nu_2^*}{E_f^* E_m}\right]$$
$$\frac{1}{G_{12}^{\text{degraded - f}}} = \frac{1}{(1+\nu_{12}^*)}\left[\frac{1}{G_{f12}} + \frac{\nu_{12}^*}{E_f^* E_m}\right] \tag{5.7}$$

where E_m and G_m are the matrix moduli and E_{f2} and G_{f12} are the transverse fiber moduli. ν_2^* and ν_{12}^* are obtained from the stress partitioning parameters and the overall fiber volume fraction, V_f, through:

$$\nu_2^* = \eta_2 \frac{1 - V_f}{V_f} \qquad \nu_{12}^* = \eta_{12} \frac{1 - V_f}{V_f} \tag{5.8}$$

The axial compressive strength is reduced by using the constant n and the degraded in-plane shear moduli for either matrix or fiber failure, as given by:

$$\begin{aligned} X_c^{\text{degraded - m}} &= X_c \left(\frac{G_{12}^{\text{degraded - m}}}{G_{12}} \right)^n \\ X_c^{\text{degraded - f}} &= X_c \left(\frac{G_{12}^{\text{degraded - f}}}{G_{12}} \right)^n \end{aligned} \tag{5.9}$$

Also, to account for reduction in the interaction term of Tsai-Wu criterion after failure, F_{12}^* is degraded for each mode, such that:

$$F_{12}^{*\,\text{degraded - m}} = E_m^* F_{12}^* \qquad F_{12}^{*\,\text{degraded - f}} = E_f^* F_{12}^* \tag{5.10}$$

In summary, if either matrix or fiber failure is detected within a yarn, degradation of the local effective yarn stiffnesses and material strengths is obtained by multiplying the yarn

material data of the first column of Table 5.3 by the associated factors from either column 2 for matrix failure or 3 for fiber failure.

Table 5.3: Yarn degradation factors for matrix and fiber failure

Yarn material data	Matrix mode degradation factors	Fiber mode degradation factors
E_1	1.0	E_f^*
E_2	$E_2^{\text{degraded - m}}/E_2$	$E_2^{\text{degraded - f}}/E_2$
ν_{12}	E_m^*	E_f^*
G_{12}	$G_{12}^{\text{degraded - m}}/G_{12}$	$G_{12}^{\text{degraded - f}}/G_{12}$
X_t	1.0	1.0
X_c	$(G_{12}^{\text{degraded - m}}/G_{12})^n$	$(G_{12}^{\text{degraded - f}}/G_{12})^n$
Y_t	1.0	1.0
Y_c	1.0	1.0
S	1.0	1.0
F_{12}^*	E_m^*	E_f^*

To simplify our notations, we will denote, respectively, D_m and D_f as the matrix and fiber degradation vectors, defined by:

$$D_m = \begin{bmatrix} 1.0 \\ E_2^{\text{degraded - m}}/E_2 \\ E_m^* \\ G_{12}^{\text{degraded - m}}/G_{12} \\ (G_{12}^{\text{degraded - m}}/G_{12})^n \\ E_m^* \end{bmatrix} \qquad D_f = \begin{bmatrix} E_f^* \\ E_2^{\text{degraded - f}}/E_2 \\ E_f^* \\ G_{12}^{\text{degraded - f}}/G_{12} \\ (G_{12}^{\text{degraded - f}}/G_{12})^n \\ E_f^* \end{bmatrix} \tag{5.11}$$

5.3.3 Algorithm

The progressive failure analysis was programmed in a Fortran subroutine called PROFAIL which was added to the previous 'yarnstiff.f' Fortran program that computes effective properties of a balanced plain weave fabric under small crimp angle approximation. Input and output parameters for subroutine PROFAIL are listed in Table 5.4 and Table 5.5. The subroutine computes the degraded local effective compliance matrices for warp and fill yarns that are later used in the PSTIF subroutine to compute overall effective properties of the RUC. Other subroutines were added to determine the coefficients of the Tsai-Wu criterion (strength parameters $[F]$ and reduced stiffnesses $[Q]$) as well as the degradation vectors D_m and D_f, and the local strains as a function of *x* for the warp yarns or *y* for the fill yarns. These subroutines are not discussed here, they are directly related to the equations that were derived in the previous section.

As the Fortran language does not allow symbolic manipulations, we can not solve the Tsai-Wu criterion for each value of *x* or *y*. We thus have to discretize the yarns into slices and compute the value of the left hand side of Eq. (5.1) at each extremity of these slices. The number of slices is controlled by the input parameter *N* as described in Table 5.4.

Table 5.4: Input parameters for subroutine PROFAIL

Variable	Description
STATEV	Two-by-one vector containing the information on failure states for both warp and fill yarns.
STRAN	Six-by-one vector containing the total off-axis strains at the beginning of the increment.
X_t	Tensile strength in the fiber direction
X_c	Compressive strength in the fiber direction
Y_t	Tensile strength in the transverse direction
Y_c	Compressive strength in the transverse direction
S	In-plane longitudinal shear strength
F_{12}^*	Interaction term factor in Tsai-Wu criterion.
E_f	Two-by-one vector containing fiber in-plane and transverse Young moduli.
G_f	Two-by-one vector containing fiber in-plane and transverse shear moduli.
ν_f	Two-by-one vector containing fiber in-plane and transverse Poisson's ratios.
E_r	Resin Young modulus.
G_r	Resin shear modulus.
ν_r	Resin Poisson's ratio.
L_u	Length of undulating region for warp and fill yarns.
t	Yarn thickness.
a	Yarn spacing; also the half width of the RUC.

Table 5.4: Input parameters for subroutine PROFAIL

Variable	Description
p_d	Yarn packing density.
V_f	Fiber volume fraction of the RUC
N	Number of points where the Tsai-Wu criterion is evaluated.

Table 5.5: Output variables for PROFAIL subroutine

Variable	Description
S_0	Six-by-six-by-two matrix containing degraded compliance matrices for both warp and fill yarns.
NEWSTATEV	Two-by-one vector containing the new value for failure states of both warp and fill yarns.

The algorithm is as follows:

1. *Evaluate non-degraded effective properties for warp and fill yarns using self-consistent model (subroutine PROPER of 'yarnstiff.f'):* $E^T = [E_1, E_2]$, $G^T = [G_{12}, G_{23}]$, $\nu^T = [\nu_{12}, \nu_{23}]$.

2. *Define position vector,* X*, corresponding to the discretization of yarns:*

   $X(i) = \frac{(i-1)a}{N}$, i=1..N+1

3. *Initialize NEWSATEV=STATEV.*

4. *Evaluate degradation factors* D_m *and* D_f *(Eq. (5.11)) through DEGFAC subroutine.*

5. *Start progressive failure analysis and begin iteration loop: For i = 1, 2. (1: warp yarn analysis, 2: fill yarn analysis):*

5.a Degrade strength parameters X_c *and* F_{12}^* *corresponding to yarn failure state using Eqs. (5.9) and (5.10):*
If STATEV(i)=2, yarn is in matrix failure.
If STATEV(i)=3, yarn is in single fiber failure.

5.b Evaluate Tsai-Wu expression using local strains as a function of the position vector, $\varepsilon_0(X(j))$ *, for different values of j:*
Begin iteration loop: for j=1 to N+1 in steps of 1:

5.b.i Determine local strain tensor STRANLOC = $\varepsilon_0(X(j))$

5.b.ii Determine Tsai-Wu criterion coefficients through TSAIWU subroutine.

5.b.iii Evaluate Tsai-Wu expression (left-hand side of Eq. (5.1)) = $TSAI$.

5.b.iv If $TSAI > 1$ *, failure has occurred. Check previous failure state.*

5.b.v If STATEV(i)=1, first failure has occurred for this yarn:

5.b.v.1 If $\varepsilon_2 > 0$ *, matrix failure has occurred, degrade* E_2, ν_{12}, G_{12}. *Update NEWSTATEV(i)=2. Goto 5.c.*

5.b.v.2 Else if $\varepsilon_2 < 0$ *, first fiber failure has occurred, degrade* $E_1, E_2, \nu_{12}, G_{12}$. *Update NEWSTATEV(i)=3. Goto 5.c.*

5.b.vi Else if STATEV(i)=2 then yarn was in matrix failure and first fiber failure has occurred, degrade $E_1, E_2, \nu_{12}, G_{12}$. *Update NEWSTATEV(i)=3. Goto 5.c.*

5.b.vii Else the yarn is in ultimate failure and there is no need to degrade properties further. Goto 5.c.

5.b.viii If $TSAI \leq 1$ *failure does not occurred at this point. Go back to 5.b.i.*

5.c Update E, G and ν *for warp and fill yarn:* $E(1, i) = E_1,\ E(2, i) = E_2\ etc....$

5.d Update degraded compliance matrices for warp and fill yarns, $S_0(*, *, \mathrm{i})$ *out of* E, G and ν.

Fig. 5.1 shows the flow chart for the PROFAIL subroutine for a better understanding of this algorithm.

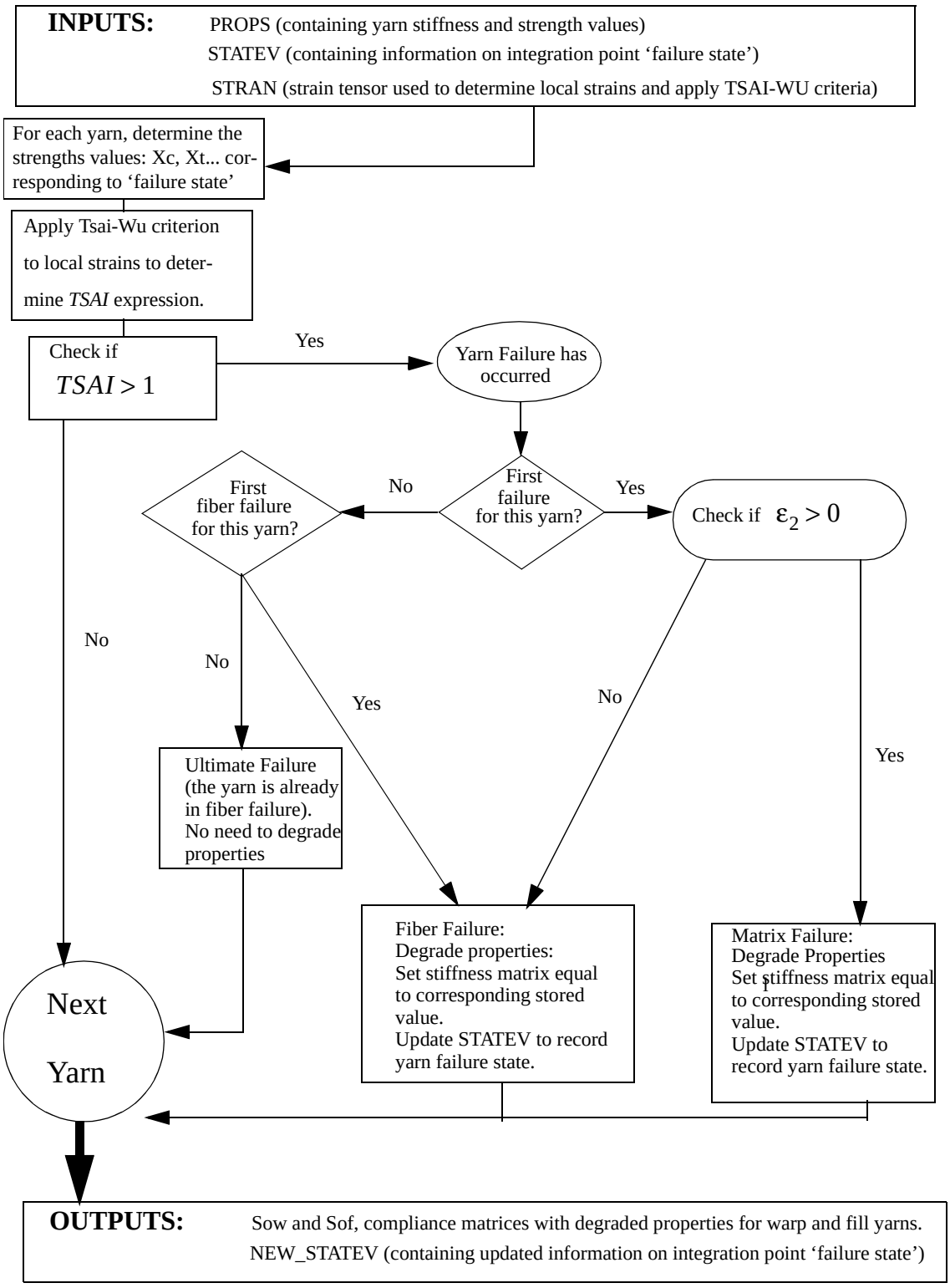

Fig. 5.1 Flow chart for balanced plain weave material failure and degradation

5.4 Concluding Remarks

For a balanced plain weave fabric we have defined a material failure model, applying Tsai-Wu quadratic criterion to the local strains within the warp and fill yarns, and derived equations to degrade strengths and stiffnesses for each set of yarns based on two modes of failure: matrix and fiber. For a given input array of strains at the beginning of an incremental step, the progressive model can thus predict, according to the previous failure state for each set of yarns, the next failure state of each yarn and then compute the effective stiffness matrix for the degraded RUC. The UMAT, associated with ABAQUS, thus defines a full progressive failure analysis where failure is predicted at each step of the procedure and at each material integration point of the finite element model.

At the present time, the subroutine has only been tested as a stand-alone program with Visual Fortran 6.0, where the strain tensor, STRAN, and the state variable, STATEV, are prescribed as data by the user. Future work would thus include the debugging of the UMAT within ABAQUS procedures. The resulting analysis technique could then be used to calculate overall load-displacement response of, and damage progressions in, a textile material coupon configuration under a simple loading. Also, the material failure model could be applied to more complicated architectures, such as the 2D braided or 2D triaxial braided composites. Further developments and improvements of this model are then fully envisaged and could lead to a simple but interesting approach to predict failure in textile composite materials.

References

[1] Poe, C.C., and Harris, C.E., “Mechanics of Textile Composites Conference”, NASA Conference Publication 3311, Part 1&2, October 1995.

[2] Scardino, F., “An Introduction to Textile Structures and their Behavior”, *Textile Structural Composites, Composite Material Series*, Vol. 3, Elsevier, New York, 1989, pp. 1-26.

[3] Source: http://www.netcomposites.com. Site accessed on February 15, 2002. Published courtesy of David Cripps, SP Systems.

[4] Cox, B.N. and Flanagan, G., “Handbook of Analytical Methods for Textile Composites”, NASA CR-4750, March 1997.

[5] Source: http://web.mit.edu/lmp/www/composites/costmodel/ProcessDescription/Braiding2D1.html. Site accessed on February 15, 2002.

[6] Chou, T.W. and Ishikawa, T. “Analysis and Modeling of Two-dimensional Fabric Composites”, Chapter 7 of *Textile Structural Composites*, *Composite Material Series, Vol.3*, by Chou T.W. and Ko, K., R. Byron Pipes Editor, 1989.

[7] Ishikawa, T. and Chou, T-W. “Stiffness and Strength Behavior of Woven Fabric Composites”, *Journal of Material Science*, 1982.

[8] Ishikawa, T. and Chou, T-W. “Elastic Behavior of Woven Hybrid Composites”, *Journal of Composite Materials*, 1982.

[9] Naik, R.A., “Analysis of Woven and Braided Fabric Reinforced Composites,” NASA Contractor Report CR-194930, 1994.

[10] Naik, R.A., Ifju, P.G., Masters, J.E. “Effect of Fiber Architecture Parameters on Mechanical Performance of Braided Composites”, NASA, Langley Research Center, The Fourth NASA/DOD Advanced Composites Technology Conference, Part 1, Volume 1, Dec. 1993, p. 525-554.

[11] Rosen, B.W., Chatterjee, S.N. and Kibler, J.J.: “An Analysis Model for Spatially Oriented Fiber Composites”, *Composite Materials: Testing and Design (Fourth Conference), ASTM STP 617,* American Society for Testing and Materials, 1977, pp.243-254.

[12] Naik, N.K., and Ganesh, V.K., “An Analytical Method for Plain Weave Fabric Composites,” *Composites*, Vol. 26, 1995, pp. 281-289.

[13] Scida D., Aboura Z., Benzeggagh M.L., Bocherens E., “A Micromechanics Model for 3D Elasticity and Failure of Woven-fibre Composite Materials”, *Composites Science and Technology*, 1999.

[14] Masters, J. E. , Foye, R.L., Pastore, C.M., Gowayed, Y.A., “Mechanical Properties of Triaxially Braided Composites: Experimental and Analytical Results”, *Journal of Composites Technology & Research*, Vol. 15, No. 2, Summer 1993, pp.112-122.

[15] Byun, J-H. “The analytical characterization of 2D braided textile composites”, *Journal of Composites Science and Technology,* Elsevier Science Ltd., 2000.

[16] Ko, F.K. and Pastore, C.M. “Structure and Properties of an Integrated 3D Fabric for Structural Composites”, *Recent Advances in Composites in the United States and Japan,* ASTM STP 864, J.R. Vinson and M. Taya, Eds., American Society for Testing an Materials, Philadelphia, 1985, pp. 428-439.

[17] Dow, N.F. and Ramnath, V. “Analysis of Woven Fabrics for Reinforced Composite Materials”, NASA CR-178275, April 1987, National Aeronautics and Space Administration, Hampton, Virginia.

[18] Naik, R.A. “Failure Analysis of Woven and Braided Fabric Reinforced Composites”, Analytical Services and Materials, Inc., Sept. 1994, Hamton, Virginia.

[19] Hyer, M.W., *Stress Analysis of Fiber-Reinforced Composite Materials*, WCB/ McGraw-Hill, 1998.

[20] Tsai, S.W, *Theory of composites design, Think Composite*, section 4.2, 1992.

[21] Naik, N.K, *Woven Fabric Composites*, Technomic publication, 1994.

[22] Foye, R.L. “Finite Element Analysis of the Stiffness of Fabric Reinforced Composites”, NASA CR-189597, Feb. 1992, National Aeronautics and Space Administration, Hampton, Virginia.

[23] Perez, J.G. “Energy Absorption and Progressive Failure Response of Composite Fuselage and Frames”, Master of Science Thesis in Aerospace Engineering, Virginia Polytechnic Institute and State University, Blacksburg, Virginia, July 1999.

[24] Whitney, J. M. , McCullough, R.L. *Micromechanical materials modeling*, Volume 2, Technomic publication, 1990.

[25] Woodson, M.B. “Optimal Design of Composite Fuselage Frames for Crashworthiness”, Doctor of Philosophy Dissertation in Aerospace Engineering, Virginia Polytechnic Institute and State University, Blacksburg, Virginia, December 1994.

[26] Abramowitz, M and I.A.Stegun, Handbook of Mathematical Functions, Dover Publications, 1965, section 17.6

Appendix A: Integration of A_{tip} for Plain Weave Architecture

The integral for the area of the tip of the fill yarn, Eq. (2.25), is evaluated by first changing the independent variable from x to ϕ as defined by $\phi \equiv (\pi x)/L_u$. Differentiation of Eqs. (2.14) and (2.15) with respect to x, and using Eqs. (2.2), (2.3), and (2.5), we find

$$\begin{aligned} \frac{dx_1}{dx} &= 1 - \tan^2\beta_c \sin\phi [1 + \tan^2\beta_c \cos^2\phi]^{-3/2} \\ z_1 dx &= \frac{tL_u}{2\pi}\{\sin\phi - [1 + \tan^2\beta_c \cos^2\phi]^{-1/2}\} d\phi \end{aligned} \tag{A.1}$$

and

$$\begin{aligned} \frac{dx_2}{dx} &= 1 + \tan^2\beta_c \sin\phi [1 + \tan^2\beta_c \cos^2\phi]^{-3/2} \\ z_2 dx &= \frac{tL_u}{2\pi}\{\sin\phi + [1 + \tan^2\beta_c \cos^2\phi]^{-1/2}\} d\phi \end{aligned} \tag{A.2}$$

Replace $\cos^2\phi$ by $1 - \sin^2\phi$ in Eqs. (A.1) and (A.2), use the definition of m in Eq. (2.7) to get

$$\begin{aligned} \int_{x_a}^{L_u/2} z_1(x) \frac{dx_1}{dx} dx = \frac{tL_u}{2\pi} \int_{\phi_a}^{\pi/2} &\{\sin\phi - [\sqrt{1 + \tan^2\beta_c}\sqrt{1 - m\sin^2\phi}]^{-1}\} \\ &\{1 - m[1 + \tan^2\beta_c]^{-1/2} \sin\phi [1 - m\sin^2\phi]^{-3/2}\} d\phi \end{aligned} \tag{A.3}$$

where $\phi_a = (\pi x_a)/L_u$. Similarly the second integral in the equation for A_{tip}, Eq. (2.25), can be expressed as

$$\int_{x_b}^{L_u/2} z_2(x)\frac{dx_2}{dx}dx = \frac{tL_u}{2\pi}\int_{\phi_b}^{\pi/2} \{\sin\phi + [\sqrt{1+\tan^2\beta_c}\sqrt{1-m\sin^2\phi}]^{-1}\} \{1 + m[1+\tan^2\beta_c]^{-1/2}\sin\phi[1-m\sin^2\phi]^{-3/2}\}d\phi \quad \text{(A.4)}$$

where $\phi_b = \pi x_b / L_u$. The sum of Eqs. (A.3) and (A.4) is A_{tip}. Since $x_b = -x_a$, we also have $\phi_b = -\phi_a$. The equation for A_{tip} is written in the form

$$A_{tip} = \frac{tL_u}{2\pi}G_2[\phi_a(\beta_c), \beta_c] \quad \text{(A.5)}$$

where the function of the crimp angle is defined by

$$G_2[\phi_a(\beta_c), \beta_c] \equiv I_1 - (I_2 + I_3)[1+\tan^2\beta_c]^{-1/2} + I_4[1+\tan^2\beta_c]^{-1} \quad \text{(A.6)}$$

The latter function is, in turn, defined by the integrals

$$I_1 = \int_{\phi_a}^{\pi/2} (\sin\phi)d\phi + \int_{-\phi_a}^{\pi/2} (\sin\phi)d\phi \quad \text{(A.7)}$$

$$I_2 = \int_{\phi_a}^{\pi/2} [1-m\sin^2\phi]^{-1/2}d\phi - \int_{-\phi_a}^{\pi/2} [1-m\sin^2\phi]^{-1/2}d\phi \quad \text{(A.8)}$$

$$I_3 = \int_{\phi_a}^{\pi/2} m\sin\phi[1-m\sin^2\phi]^{-3/2}d\phi - \int_{-\phi_a}^{\pi/2} m\sin\phi[1-m\sin^2\phi]^{-3/2}d\phi \quad \text{(A.9)}$$

$$I_4 = \int_{\phi_a}^{\pi/2} m\sin\phi[1-m\sin^2\phi]^{-2}d\phi + \int_{-\phi_a}^{\pi/2} m\sin\phi[1-m\sin^2\phi]^{-2}d\phi \quad \text{(A.10)}$$

Evaluation the first two integrals we get

$$I_1 = 2\cos\phi_a \qquad I_2 = -2F[\phi_a, m] \quad \text{(A.11)}$$

where $F[\phi_a, m]$ is the incomplete elliptic integral of the first kind. The third integral is

$$I_3 = \frac{\{2E[\phi_a, m] + 2(-1+m)F[\phi_a, m] - \sqrt{2}m\sin 2\phi_a[2-m+m\cos 2\phi_a]^{-1/2}\}}{(-1+m)} \quad \text{(A.12)}$$

where $E[\phi_a, m]$ is the incomplete elliptic integral of the second kind. The fourth integral is

$$I_4 = \frac{m\cos\phi_a}{(1-m)(1-m+m\cos^2\phi_a)} + \frac{m \cdot \operatorname{atan}\left[\sqrt{\frac{m}{1-m}}\cos\phi_a\right]}{(1-m)\sqrt{m(1-m)}} \quad \text{(A.13)}$$

Appendix B: Elasticity Matrices of the Yarn and Resin in RUC Coordinates

The filaments composing the yarn are assumed to be parallel and not twisted. Denote the orthogonal, on-axis directions at an arbitrary point in a yarn as 1-2-3, where the 1-axis is parallel to the filaments, and the 2- axis is normal to the *z*-axis of the RUC. Let θ denote the angle of rotation about the *z*-axis transforming the Cartesian systems $(x, y, z) \rightarrow (x_1, y_1, z_1)$, where the z_1-direction is the same as the *z*-direction. Consider a second rotation through angle β about the y_1-axis transforming the Cartesian systems $(x_1, y_1, z_1) \rightarrow (1, 2, 3)$ where the 2-direction is the same as the y_1-direction. See Fig. B.1. The direction cosine matrix of the rotations from RUC directions to the yarn 1-2-3 directions are given by

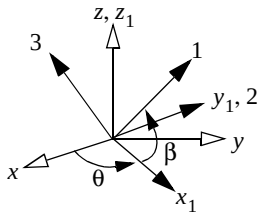

Fig. B.1Rotations from RUC directions to yarn 1-2-3 directions

$$\begin{array}{c} \\ 1 \\ 2 \\ 3 \end{array}\begin{array}{c} \begin{array}{ccc} x & y & z \end{array} \\ \begin{bmatrix} a_{11} & a_{12} & a_{13} \\ a_{21} & a_{22} & a_{23} \\ a_{31} & a_{32} & a_{33} \end{bmatrix} \end{array} = \begin{bmatrix} \cos\beta\cos\theta & \cos\beta\sin\theta & \sin\beta \\ -\sin\theta & \cos\theta & 0 \\ -\sin\beta\cos\theta & -\sin\beta\sin\theta & \cos\beta \end{bmatrix} \tag{B.1}$$

In the on-axis system let σ_0 denote the six-by-one vector of stress components, ε_0 the six-by-one vector of engineering strains, C_0 the symmetric six-by-six elasticity matrix, and let S_0 denote the symmetric six-by-six compliance matrix. The components of the stress and strain vectors are

$$\sigma_0^T = \begin{bmatrix} \sigma_1 & \sigma_2 & \sigma_3 & \sigma_{23} & \sigma_{31} & \sigma_{12} \end{bmatrix} \qquad \varepsilon_0^T = \begin{bmatrix} \varepsilon_1 & \varepsilon_2 & \varepsilon_3 & \gamma_{23} & \gamma_{31} & \gamma_{12} \end{bmatrix} \tag{B.2}$$

where $\gamma_{23}, \gamma_{31}, \gamma_{12}$ denote the engineering shear strains. The stress-strain form of the material law in the on-axis coordinates is $\sigma_0 = C_0\varepsilon_0$, and the strain-stress form is $\sigma_0 = S_0\varepsilon_0$. The elasticity matrix is the inverse of the compliance matrix; i.e., $C_0 = S_0^{-1}$. The yarn is assumed to be a transversely isotropic material in the 1-2-3 directions. The five independent material properties are the modulus of elasticity along the 1-axis E_1, the modulus of elasticity along the 2- and 3-axes, E_2, Poisson ratio in the 1-2 and 1-3 planes, ν_{12}, Poisson ratio in the 2-3 plane ν_{23}, and shear modulus in the 1-2 and 1-3 planes G_{12}. The on-axis compliance matrix is

$$S_0 = \begin{bmatrix} E_1^{-1} & -\nu_{12}E_1^{-1} & -\nu_{12}E_1^{-1} & 0 & 0 & 0 \\ -\nu_{12}E_1^{-1} & E_2^{-1} & -\nu_{23}E_2^{-1} & 0 & 0 & 0 \\ -\nu_{12}E_1^{-1} & -\nu_{23}E_2^{-1} & E_2^{-1} & 0 & 0 & 0 \\ 0 & 0 & 0 & 2(1+\nu_{23})E_2^{-1} & 0 & 0 \\ 0 & 0 & 0 & o & G_{12}^{-1} & 0 \\ 0 & 0 & 0 & 0 & 0 & G_{12}^{-1} \end{bmatrix} \tag{B.3}$$

Let the stress vector and strain vector in the (x, y, z) system, or off-axis system, be denoted by σ_1, and ε_1, respectively. The component form of these vectors are

$$\sigma_1^T = \begin{bmatrix} \sigma_x & \sigma_y & \sigma_z & \sigma_{yz} & \sigma_{zx} & \sigma_{xy} \end{bmatrix} \qquad \varepsilon_1^T = \begin{bmatrix} \varepsilon_x & \varepsilon_y & \varepsilon_z & \gamma_{yz} & \gamma_{zx} & \gamma_{xy} \end{bmatrix} \tag{B.4}$$

The transformation of the stress and strain vectors to the on-axis directions from the off-axis system is accomplished by the orthogonal six-by-six matrices T_σ and T_ε as shown by the following relations:

$$\sigma_0 = T_\sigma\sigma_1 \qquad \varepsilon_0 = T_\varepsilon\varepsilon_1 \tag{B.5}$$

Using second order tensor transformation relations, and the definition of the engineering strain vector, it can be shown that

$$T_\varepsilon = \begin{bmatrix} a_{11}^2 & a_{12}^2 & a_{13}^2 & 2a_{12}a_{13} & 2a_{11}a_{13} & 2a_{11}a_{12} \\ a_{21}^2 & a_{22}^2 & a_{23}^2 & 2a_{22}a_{23} & 2a_{21}a_{23} & 2a_{21}a_{22} \\ a_{31}^2 & a_{32}^2 & a_{33}^2 & 2a_{32}a_{33} & 2a_{31}a_{33} & 2a_{31}a_{32} \\ a_{21}a_{31} & a_{22}a_{32} & a_{23}a_{33} & a_{23}a_{32} + a_{22}a_{33} & a_{23}a_{31} + a_{21}a_{33} & a_{22}a_{31} + a_{21}a_{32} \\ a_{11}a_{31} & a_{12}a_{32} & a_{13}a_{33} & a_{13}a_{32} + a_{12}a_{33} & a_{13}a_{31} + a_{11}a_{33} & a_{12}a_{31} + a_{11}a_{32} \\ a_{11}a_{21} & a_{12}a_{22} & a_{13}a_{23} & a_{13}a_{22} + a_{12}a_{23} & a_{13}a_{21} + a_{11}a_{23} & a_{12}a_{21} + a_{11}a_{22} \end{bmatrix} \quad \text{(B.6)}$$

Substitute the stress and strain transformations into the on-axis material law to get

$$T_\sigma \sigma_1 = C_0 T_\varepsilon \varepsilon_1 \quad \text{(B.7)}$$

Premultiply this equation by T_σ^{-1} to get

$$\sigma_1 = T_\sigma^{-1} C_0 T_\varepsilon \varepsilon_1 = C_1 \varepsilon_1 \quad \text{(B.8)}$$

where the off-axis elasticity matrix for the yarn is denoted as C_1. From the tensor transformation equations it can be shown that the inverse of the stress transformation matrix is equal to the transpose of the strain transformation matrix; i.e., $T_\sigma^{-1} = T_\varepsilon^T$. We write the off-axis elasticity matrix as

$$C_1(\theta, \beta) = T_\varepsilon^T C_0 T_\varepsilon \quad \text{(B.9)}$$

For the warp yarn angle $\theta = 0$ and the angle $\beta = \beta_w(x)$. For the fill yarn angle $\theta = \pi/2$ and angle $\beta = \beta_f(y)$.

The resin matrix is assumed to be homogenous and isotropic. Hence there are two independent material properties: the modulus of elasticity E_r and Poisson's ratio ν_r. The elasticity matrix for the resin is

$$C_{\text{resin}} = \begin{bmatrix} E_r^{-1} & -\nu_r E_r^{-1} & -\nu_r E_r^{-1} & 0 & 0 & 0 \\ -\nu_r E_r^{-1} & E_r^{-1} & -\nu_r E_r^{-1} & 0 & 0 & 0 \\ -\nu_r E_r^{-1} & -\nu_r E_r^{-1} & E_r^{-1} & 0 & 0 & 0 \\ 0 & 0 & 0 & 2(1+\nu_r)E_r^{-1} & 0 & 0 \\ 0 & 0 & 0 & 0 & 2(1+\nu_r)E_r^{-1} & 0 \\ 0 & 0 & 0 & 0 & 0 & 2(1+\nu_r)E_r^{-1} \end{bmatrix}^{-1} \quad \text{(B.10)}$$

Appendix C: Description of ‘exactplainweave.f’ FORTRAN Program

Input Data

Geometry:

- **a**: yarn spacing in mm. As we assume there is no gap between the yarns, a is also the yarn width which is equal for warp and fill.
- **pd**: packing density of the yarns, i.e. the fiber volume fraction within a single yarn.
- **Vf**: overall fiber volume fraction within the RUC.

Then prescribe either:

- **(n,df)**: respectively number of filaments (fibers) within yarn and diameter of each of these filaments, in mm.

or:

- **t**: yarn thickness in mm.

Material properties:

Prescribe either:

- Fibers and resin properties as for the examples from N.K. Naik [12] and D. Scida [13]:

The fibers are assumed to be transversely isotropic so the properties ‘P’ of the fiber phase have only two different components: ‘Pl’, P longitudinal along the fiber axis, and ‘Pt’, P transversal. This leads to 6 variables for the material properties of the fiber that are the components of the 3 vectors $E_f = \left[E_{fl}\ E_{ft}\right]^T$, $G_f = \left[G_{fl}\ G_{ft}\right]^T$ and $\upsilon_f = \left[\upsilon_{fl}\ \upsilon_{ft}\right]^T$. In addition to these 6 values (in fact only 5 are independents as the fibers are isotropic in the plane orthogonal to their direction, so we get: $G_{ft} = E_{ft}/[2(\nu_{ft}+1)]$), the user must prescribe the material properties of the resin,

which is assumed to be the same for the yarns and for the overall composite. The resin is assumed to be isotropic, so the properties ‘P’ of the matrix phase have only one independent component, which leads to the 3 variables E_r, G_r, and ν_r. Note also that only two of these variables are independent as $G_r = E_r/[2(1+\nu_r)]$ [1].

Or prescribe:

- Yarn and resin properties as for the example from R.A. Naik [9]:

Once the user has given the material properties for the fibers and the resin, the main program calls a subroutine to evaluate the material properties of the yarns which will be used to compute the on-axis stiffness matrix of the yarns. However, in some cases the user can access directly the yarn material properties through experimental data. In this case the yarn properties are then prescribed by the user himself and used directly to compute the on-axis stiffness matrix for a given yarn.The resin, as explained previously, is assumed to be isotropic and should be the same as the resin used to manufacture the yarns.

The Subroutines

There are 28 subroutines related to the main programs, all these subroutines match one of the four following categories:

- PROP: subroutines that are used or intended to determine the mechanical properties of the yarns from the property data of the fibers and resin.
- GEO: subroutines that are used or intended to determine all geometry parameters (t, Lu, tr, β_c ...etc.) from the geometry input data (a, Vf, pd...)
- STI: subroutines that are used or intended to determine the plain weave effective stiffness matrix from one quarter of the RUC (in fact all of the subroutines contribute to

1. NB: for D. SCIDA [13] the Vinylester resin he uses as an example is not isotropic, for this case the relation here-above is no longer valid and we get 3 independent variables that have to be given as data.

this computation as it is the purpose of the program, but we consider here only the ones that are related to evaluations of local and global stiffness matrices)

- MAT: mathematical subroutines, e.g. matrix product, inversion, etc., that are used by miscellaneous subroutines to provide specific mathematical operations that are not obvious to compute with FORTRAN.

All the subroutine names have between 3 and 6 characters, often related to their function, and their arguments are ordered such that the outputs of the subroutine are written first and the inputs are written after. In the description of the different subroutines, the outputs will be identified by using bold-face characters.

PROP subroutines:

There are only two of them as there is two ways used to determine the yarns mechanical properties from fibers and resin properties. The first way is to use a self consistent model [24], the subroutine associated to this method is:

Subroutine PROPER(**E,G,nu**,pd,Ef,Er,Gf,Gr,nuf,nur): E,G and nu are the output mechanical properties of the yarns which are transversely isotropic as the fibers are transversely isotropic and the resin is isotropic.

The second way to determine these properties is to use a rule of mixture [24], the subroutine associated with this method is:

Subroutine MIXPRO(**E,G,nu**,pd,Ef,Er,Gf,Gr,nuf,nur).

GEO subroutines:

The main subroutine that determines all geometry parameters from given geometry data is called:

Subroutine GEOMET(**Lu,t,tr,betac,Vyarn,Vol,volr,newa**,a,Vf,pd,n,df,TOL,imax).

This subroutine uses a fixed point iteration scheme on both t and Lu. The inputs are the geometry data, a, Vf, pd, n and df as well as a tolerance parameter TOL such that the fixed

point iteration stops when: $|\beta c_{i+1} - \beta c_i| < TOL$, where βc_i is the crimp angle evaluated at the ith step, and imax is the maximum number of iterations. The outputs are the length of the undulating part Lu, the yarn thickness t, the added layer of resin (if necessary) tr, the crimp angle βc, the volume of fill and warp yarns on quarter of a unit cell Vyarn, the overall volume of the RUC Vol, the volume of resin within the RUC volr, and the new value of *a* when the crimp angle exceeds 45°: newa. This subroutine uses the algorithm described in Section 2.2.6 on page 32.

Other GEO subroutines:

Subroutine MAXCRP (**Lu,t,tr,Vyarn,Vol,volr,newa**,a,Vf,pd,n,df): this subroutine is called by the GEOMET subroutine when it converges towards a crimp angle that exceeds 45° at the end of step 2 of the algorithm. In this case as it is explained in Section 2.2.6 on page 32, we recompute a new value for a and therefore get a system of 3 equations for the 3 unknowns t, Lu and newa (or t, tr and newa if Lu exceeds a).

Subroutine FG1 (g1,betac): determines the function g1 for a given crimp angle betac(β_c), where g1 is defined by Eq. (2.10).

Subroutine FG2 (g2,phia,betac): determines the function g2 from given angle phia (ϕ_a) and crimp angle betac (β_c), where $g_2 = 1 - G_2[\phi_a(\beta_c), \beta_c]/\pi$. Function $G_2[\phi_a(\beta_c), \beta_c]$ is given by Eq. (A.6) in Appendix A.

Subroutine SOLPHIA (**phia**,betac,N,TOL): determines phia, the integration limit for the coefficients I_1, I_2, I_3, I_4 given in Eqs. (A.7) to (A.10) of Appendix A. Phia, or ϕ_a, is root of the transcendental Eq. (2.16).To solve this equation for ϕ_a, the subroutine SOLPHIA uses Newton's method with the function $f(x)$ defined by

$$f(x) = x + \tan^2\beta_c \cos x / \sqrt{1 + \tan^2\beta_c \cos^2 x} \qquad \text{(C.1)}$$

Parameter N defines the maximum number of iterations and TOL is a tolerance on ϕ_a such that the scheme stops when $|\phi_{ai} - \phi_{ai-1}| < TOL$ where ϕ_{ai} is the value of ϕ_a evaluated at the ith step.

STI subroutines:

For the purpose of calculating overall properties of the plain weave fabric, the RUC of the textile composite is treated as a spatially oriented fiber composite composed of yarns with transversely isotropic material properties and longitudinal material axes oriented at known angles θ and β.

Subroutine TRSFMA(**T**,beta,teta): determine the value of the strain-transformation matrix *T* for given angles β and θ. See Eqs. (B.1) and (B.6) in Appendix B.

Subroutine STIFLO(**C1**,Co,teta,beta): computes the stiffness matrix in local coordinate system C1 at given angles β and θ from a given on-axis stiffness matrix Co using Eq. (B.9) from Appendix B.

Subroutine BETAFI(**betaf**,x,Lu,t,a): evaluates the value of the out-of-plane angle β_f for the fill yarn for a given abscissa *x* and given geometry parameters Lu,t and a.

Subroutine BETAWA(**betaw**,x,Lu,t,a): same as BETAF but for the warp yarn

Subroutine FCTF(**Ff**,x,Co,Lu,t,a): defines the local stiffness matrix for the fill yarn ($\theta = \pi/2$) at a given abscissa *x* and for a given on-axis stiffness matrix Co and given geometry parameters Lu,t and a through the function $F_f(x) = C1(\pi/2, \beta_f(x))$.

Subroutine FCTW(**Fw**,x,Co,Lu,t,a): same as FCTF but for the warp yarn that is for $\theta = 0$, Fw is then defined as: $F_w(x) = C1(0, \beta_w(x))$

Subroutine TRAPZF(**Cin**,xo,xn,N,Co,Lu,t,a): Integrate Ff(x) between xo and xn using a trapezoidal rule on N subintervals, return the integral in matrix Cin.

Subroutine TRAPZW(**Cin**,xo,xn,N,Co,Lu,t,a): same as TRAPZF but for the warp yarn, that is Fw(x).

Subroutine ESTIFF(**Cef**,N,Co,Lu,t,a): determines the fill yarn stiffness matrix resultant Cef (denoted as Ceqf in Eq. (2.60)) for one quarter of the unit cell such that:

$$C_{ef} = \frac{1}{l}\int_0^a F_f(y)\sqrt{1+z_f'^2}\,dy = \frac{1}{l}\int_0^a C_1(\pi/2, \beta_f)\sqrt{1+z_f'^2}\,dy \tag{C.2}$$

where the arc-length of the one-half of the yarn in the RUC is denoted by l. (Note that l in Eq. (2.63) was used to represent the total arc-length of the yarn.) So we get

$$C_{ef} = \frac{1}{l}\left(\int_0^{L_u/2} F_f(y)\sqrt{1+z_f'^2}\,dy + \int_{L_u/2}^{a-L_u/2} Co\sqrt{1+z_f'^2}\,dy + \int_{a-L_u/2}^{a} F_f(y)\sqrt{1+z_f'^2}\,dy\right) \tag{C.3}$$

For the straight portion of the interval $[L_u/2,\, a-L_u/2]$ we get $C_1(\pi/2, \beta_f) = Co$. The subroutine uses a composite trapezoidal rule with N subintervals on both $[0,\, L_u/2]$ and $[a-L_u/2,\, a]$.

Subroutine ESTIFW(**Cew**,N,Co,Lu,t,a): same as ESTIFF but for the warp yarn.

Subroutine PSTIF(**Ceq**,N,Co,Cr,Lu,t,a,Vyarn,Volr,Vol): determines the effective stiffness matrix from one quarter of the RUC, Ceq, using the previous subroutines to compute the resultant stiffness matrix for warp and fill yarns and from given resin stiffness matrix Cr, on-axis stiffness matrix for the yarns Co, given geometry parameters Lu,t,a,Vyarn,Volr and Vol, using composite trapezoidal rule with N subintervals to compute Cef and Cew. We get with the programming notations:

$$C_{eq} = \frac{1}{Vol}\left(\frac{Vyarn}{2}C_{ef} + \frac{Vyarn}{2}C_{ew} + VolrC_r\right) \tag{C.4}$$

which is equivalent to Eq. (2.53).

MAT subroutines:

Subroutine CHOL1(SK,N,P): given an N by N positive-definite symmetric matrix A this routine constructs its cholesky decomposition, A = L.L^T On input, only the upper triangle of A, SK, needs to be given and it is not modified. The cholesky factor L is returned in the lower triangle of A except for its diagonal elements which are returned in P

Subroutine CHOL2(SK,N,P,**B**): solves the set of n linear equations A.x = b, where A is an N by N positive-definite symmetric matrix. A, N and P are inputs and only the lower triangle of A is accessed. B is input as the right hand side vector. The solution vector is returned in B. A,N, and P are not modified and can be left in place for successive calls with different right-hand sides B

Subroutine ELIPIE (**E**,m,phi,N): computes the incomplete elliptic integral of the second kind, E(m,phi) from given m and phi, with:

$$E(m, phi) = \int_0^{phi} (1 - m\sin\theta^2)^{-1/2} d\theta \qquad \text{(C.5)}$$

The subroutine uses a composite trapezoidal rule with N sub-intervals on [0,phi]. N is the last input argument of the subroutine.

Subroutine ELIPIF (**F**,m,phi,N): computes the incomplete elliptic integral of the first kind F(m,phi) from given m and phi, with:

$$F(m, phi) = \int_0^{phi} (1 - m\sin\theta^2)^{1/2} d\theta \qquad \text{(C.6)}$$

The subroutine uses a composite trapezoidal rule with N sub-intervals on [0,phi]. N is the last input argument of the subroutine.

Subroutine ELIPKE (**K,E**,m,Nmax,eps): computes the complete elliptic integrals of the first and second kind, respectively, K(m) and E(m), from given m, with:

$$K(m) = \int_0^{\pi/2} (1 - m\sin\theta^2)^{1/2} d\theta \qquad E(m) = \int_0^{\pi/2} (1 - m\sin\theta^2)^{-1/2} d\theta \qquad \text{(C.7)}$$

The subroutine computes the complete elliptic integrals using the method of the arithmetic-geometric mean described in Ref. [26], section 17.6. It starts with 5 initial coefficients:

$$a_o = 1, b_o = (1-m)^{1/2}, c_o = (m)^{1/2}, f_o = \frac{1}{2}, sum_o = 0 \qquad \text{(C.8)}$$

Then ELIPKE computes successively the coefficients $a_i, b_i, c_i, f_i, sum_i$,with:

$$a_i = (a_{i-1} + b_{i-1})/2 \qquad \text{(C.9)}$$

$$b_i = (a_{i-1} b_{i-1})^{1/2} \qquad \text{(C.10)}$$

$$c_i = (a_{i-1} - b_{i-1})/2 \qquad \text{(C.11)}$$

$$f_i = 2 f_{i-1} \qquad \text{(C.12)}$$

$$sum_i = sum_{i-1} + f_i c_i^{\,2} \qquad \text{(C.13)}$$

The subroutine stops at iteration Nmax, specified as input argument, when $\left|\frac{C_{Nmax}}{a_{Nmax}}\right| < eps$, where the tolerance eps is specified as the last input argument. Then we get:

$$K(m) = \pi/(2a_{Nmax}) \qquad E(m) = K(m)(1 - sum_{Nmax}) \qquad \text{(C.14)}$$

Subroutine INDUM(**A**,LL,KK): initialize all coefficients of a LLxKK matrix A to zero (using double precision) and return the initialized matrix in the original one (so A is both input and output of this subroutine).

Subroutine INVERT(A,**C**,M,N): inverse a positive symmetric matrix A using LU decomposition and return the result in the matrix C.

Subroutine MATMUL(AMAT1,AMAT2,**PROD**,M,N,MP,MQ): multiply an MxN matrix AMAT1 by an MPxMQ matrix AMAT2 and return the result in the matrix PROD. Also return a warning message if $N \neq MP$.

Subroutine POLSOL(**sol1,sol2,typ**,a,b,c): solves the quadratic homogeneous equation: $ax^2 + bx + c = 0$ for given coefficients a,b and c, and return the two roots sol1 and sol2 (when real solutions are found) along with the logical parameter typ such that typ=true when the solutions are real, and typ=false when the solutions are complex.

Subroutine TRANSP(A,**C**,M,N): evaluate the transpose of an MxN matrix A and return result in C

Output Data:

The aim of this program is to output the textile composite material properties but the program can also output the geometry data that have been computed during the different steps if the user needs them.

Geometric output data

Variable	Description
t	yarn thickness
L_u	length of the undulation region
β_c	crimp angle
t_r	thickness of additional resin layer
$newa$	new yarn spacing; only if $\beta_c = 45°$
V_{yarn}	volume of the yarns in one quarter of the RUC
Vol	volume of one quarter of the RUC
Vol_r	volume of the resin in one quarter of the RUC

Material properties

- The 3 Young Moduli, Exx, Eyy and Ezz.
- The 3 Shear Moduli Gxy, Gyz,Gxz.
- The 3 Poisson's ratio: ν_{xy}, ν_{yz}, ν_{xz}

There are various possibilities to output these results, they can be displayed directly on the screen or stored in a file that can be read by ABAQUS for example if we want to use the program as a subroutine for this software.

Program Flow Chart:

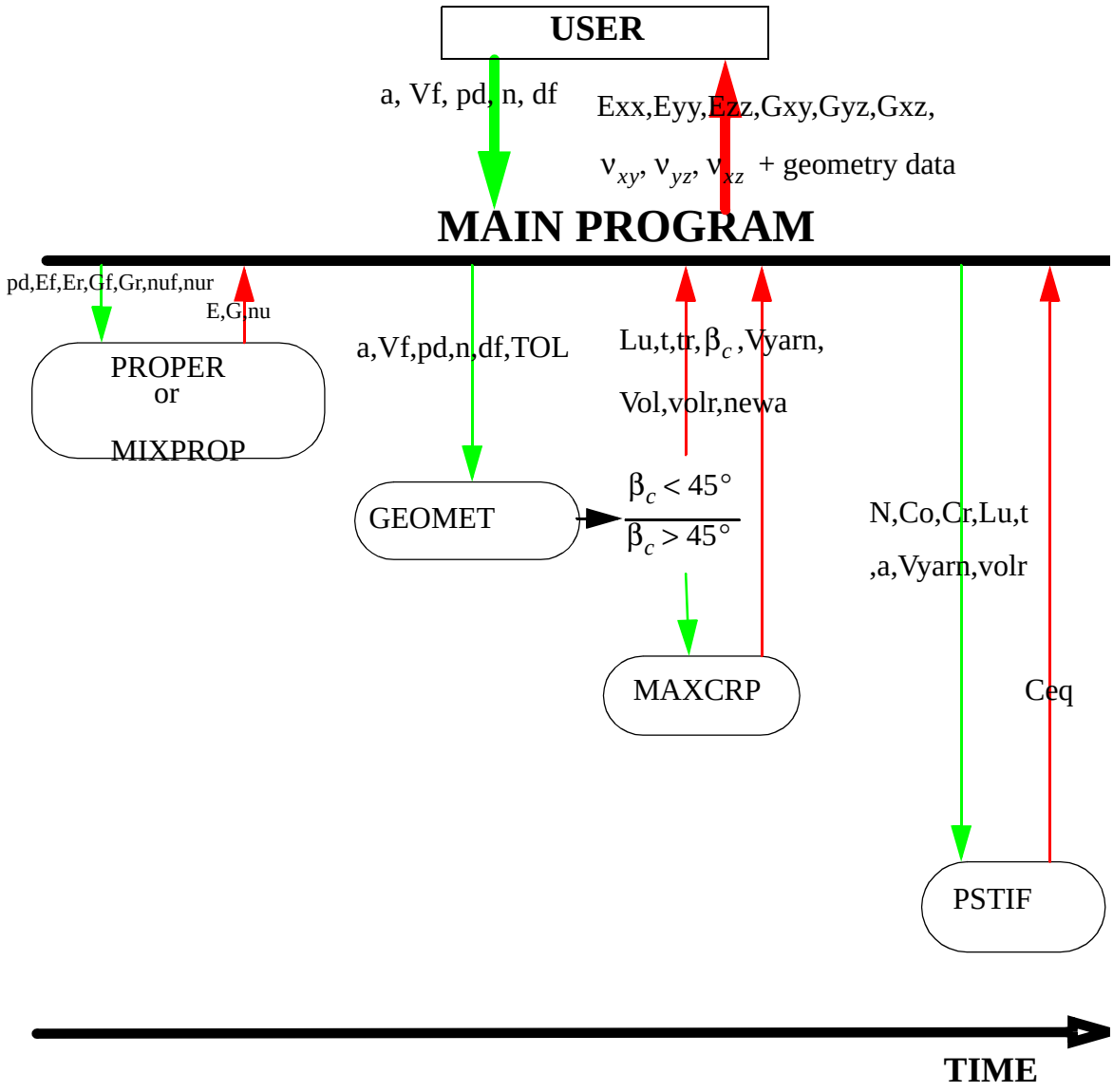
USER
a, Vf, pd, n, df
Exx,Eyy,Ezz,Gxy,Gyz,Gxz,
ν_{xy}, ν_{yz}, ν_{xz} + geometry data
MAIN PROGRAM
pd,Ef,Er,Gf,Gr,nuf,nur
E,G,nu
PROPER
or
MIXPROP
a,Vf,pd,n,df,TOL
GEOMET
Lu,t,tr,β_c,Vyarn,
Vol,volr,newa
$\beta_c < 45°$
$\beta_c > 45°$
MAXCRP
N,Co,Cr,Lu,t
,a,Vyarn,volr
Ceq
PSTIF
TIME

Appendix D: Integration of Ao and Ab for 2x2 2D Triaxial Braided Composite

Derivation of the axial yarn cross-sectional area A_o.

We start from Eq. (3.43) on page 92 in Chapter 3:

$$A_o = 2\int_{\frac{d_o - w_o}{2}}^{\frac{d_o + w_o}{2}} z_1(x)dx \tag{D.1}$$

where $z_1(x)$ is given by Eq. (3.38) on page 91. Separating the undulating regions from the straight portions of the upper curve of the axial yarn cross-section in Fig. 3.6 on page 90, we can rewrite Eq. (D.1) as:

$$A_o = 2\left[\int_{\frac{d_o - w_o}{2}}^{L_u/2} z_1(x)dx + \int_{L_u/2}^{d_o - L_u/2} z_1(x)dx + \int_{d_o - L_u/2}^{\frac{d_o + w_o}{2}} z_1(x)dx\right] \tag{D.2}$$

The first integral can be written as:

$$\int_{\frac{d_o - w_o}{2}}^{L_u/2} z_1(x)dx = \int_{\frac{d_o - w_o}{2}}^{L_u/2} \frac{(t_o + t_b)}{2}\sin\left(\frac{\pi x}{L_u}\right) - \frac{t_b}{2}\,dx \tag{D.3}$$

Recall that $d_o - w_o = (2L_u s)/\pi$ (Eq. (3.42)), we get:

$$\int_{\frac{d_o - w_o}{2}}^{L_u/2} z_1(x)dx = \frac{t_o + t_b}{2}\left[-\frac{L_u}{\pi}\cos\left(\frac{\pi x}{L_u}\right)\right]\Bigg|_{(L_u s)/\pi}^{L_u/2} - \frac{t_b}{2}\left[\frac{L_u}{2} - \frac{L_u s}{\pi}\right] \tag{D.4}$$

After simplification we find:

$$\int_{\frac{d_o - w_o}{2}}^{L_u/2} z_1(x)dx = \frac{t_o + t_b}{2}\left[\frac{L_u}{\pi}\cos s\right] - \frac{t_b L_u}{4}\left[1 - \frac{2s}{\pi}\right] \tag{D.5}$$

Now, the second integral can be easily computed:

$$\int_{L_u/2}^{d_o - L_u/2} z_1(x)dx = \int_{L_u/2}^{d_o - L_u/2} \frac{t_o}{2}dx = \frac{t_o}{2}[d_o - L_u] \tag{D.6}$$

And the last integral, by symmetry, is equal to the first one, so we get:

$$\int_{\frac{d_o - w_o}{2}}^{L_u/2} z_1(x)dx = \int_{d_o - L_u/2}^{\frac{d_o + w_o}{2}} z_1(x)dx \tag{D.7}$$

So finally we can write for A_o:

$$A_o = 2\left[2\left[\frac{(t_o + t_b)}{2}\frac{L_u}{\pi}\cos s - \frac{t_b L_u}{4}\left(1 - \frac{2s}{\pi}\right)\right] + \frac{t_o}{2}[d_o - L_u]\right] \tag{D.8}$$

Simplifying Eq. (D.8) leads to:

$$A_o = t_o d_o - L_u\left(\frac{t_o + t_b}{2}\right)\left(1 - \frac{2}{\pi}\left(\frac{s\,t_b}{t_o + t_b} + \cos s\right)\right) \tag{D.9}$$

Introducing the vertical shift $V_s = t_o + t_b$ and noticing that $\frac{t_b}{t_o + t_b} = \sin s$ we find:

$$A_o = t_o d_o - L_u V_s\left[1 - \frac{2}{\pi}(s\sin s + \cos s)\right] \tag{D.10}$$

Now, $d_o = w_o + \frac{2L_u s}{\pi}$ so we can simplify Eq. (D.10) to match Eq. (15) of Ref. [9]:

$$A_o = t_o w_o + \frac{t_o 2L_u s}{\pi} - L_u V_s\left[1 - \frac{2}{\pi}(s\sin s + \cos s)\right] \tag{D.11}$$

$$A_o = t_o w_o + (t_o + t_b)\left(\frac{t_o}{t_o + t_b}\right)\frac{2L_u s}{\pi} - L_u V_s\left[1 - \frac{2}{\pi}(s\sin s + \cos s)\right]$$

Now $\frac{t_o}{t_b} = m$ and $\frac{t_b}{t_o + t_b} = \sin s$ so we can write:

$$A_o = t_o w_o - L_u V_s \left[1 - \frac{2}{\pi}(s \sin s(1+m) + \cos s) \right] \tag{D.12}$$

But $1 + m = 1 + \frac{t_o}{t_b} = \frac{t_b + t_o}{t_b} = \frac{1}{\sin s}$, so we finally get:

$$A_o = w_o t_o - L_u V_s \left[1 - \frac{2}{\pi}(s + \cos s) \right] \tag{D.13}$$

Eq. (D.13) is identical to Eq. 15 of Ref. [9].

Derivation of the braider yarn cross-sectional area A_b.

We start from Eq. (3.52) on page 94:

$$A_b = 2 \int_0^{w_b} z_u(x) dx \tag{D.14}$$

where $z_u(x)$ is given by Eq. (3.49) on page 93. Separating the undulating regions from the straight portions of the upper curve of the braider yarn cross-section in Fig. 3.7 on page 94, we can rewrite Eq. (D.14) as:

$$A_b = 2 \left[\int_0^{x_o} z_u(x) dx + \int_{x_o}^{w_b - x_o} z_u(x) dx + \int_{w_b - x_o}^{w_b} z_u(x) dx \right] \tag{D.15}$$

The first integral can be written as:

$$\int_0^{x_o} z_u(x) dx = \int_0^{x_o} \left(\frac{t_o + t_b}{2} \right) \sin\left(\frac{\pi x}{L_u} \right) dx \tag{D.16}$$

Recall that $x_o = \frac{L_u s}{\pi}$ from Eq. (3.51), we find:

$$\int_0^{x_o} z_u(x)dx = \int_0^{\frac{L_u s}{\pi}} \left(\frac{t_o + t_b}{2}\right)\sin\left(\frac{\pi x}{L_u}\right)dx \tag{D.17}$$

Thus:

$$\int_0^{x_o} z_u(x)dx = \left[-\left(\frac{t_o + t_b}{2}\right)\cdot\frac{L_u}{\pi}\cdot\cos\left(\frac{\pi x}{L_u}\right)\right]\Bigg|_0^{\frac{L_u s}{\pi}} \tag{D.18}$$

And finally, we get:

$$\int_0^{x_o} z_u(x)dx = \frac{t_o + t_b}{2}\cdot\frac{L_u}{\pi}\cdot[1-\cos s] \tag{D.19}$$

The second integral can be evaluated as:

$$\int_{x_o}^{w_b - x_o} z_u(x)dx = \int_{\frac{L_u s}{\pi}}^{w_b - \frac{L_u s}{\pi}} \frac{t_b}{2}\,dx = \frac{t_b}{2}\left[w_b - \frac{2L_u s}{\pi}\right] \tag{D.20}$$

The third integral is equal to the first one by symmetry, so we get:

$$\int_0^{x_o} z_u(x)dx = \int_{w_b - x_o}^{w_b} z_u(x)dx \tag{D.21}$$

Using Eq. (D.19), (D.20) and (D.21) we can write for A_b:

$$A_b = 2\left[2\cdot\frac{t_o + t_b}{2}\cdot\frac{L_u}{\pi}\cdot(1-\cos s) + \frac{t_b}{2}\left(w_b - \frac{2L_u s}{\pi}\right)\right] \tag{D.22}$$

Introducing the vertical shift $V_s = t_o + t_b$ we can rewrite Eq. (D.22) as:

$$A_b = w_b t_b - \frac{2}{\pi}L_u[t_b s - V_s(1-\cos s)] \tag{D.23}$$

Eq. (D.23) is identical to Eq. 16 of Ref. [9].

Vita

Nicolas Chretien was born on December 29, 1977 in Paris, France. He graduated from high school with honors in 1995 and after three years in preparatory classes at Lycee Stanislas in Paris, he entered the engineering school ENSICA (Ecole Nationale Superieure d'Ingenieurs de Constructions Aeronautiques) in Toulouse, where he pursued a Master's degree in aerospace engineering. During his last year at ENSICA he went to Virginia Polytechnic and State University within the scope of a graduate exchange program to complete his degree at ENSICA. In order to add an international dimension to his education and deepen his technical skills, he then decided to apply to the graduate school to get a Master of Science degree from the Aerospace and Ocean Department at the same time. He graduated in May 2002 and returned to Europe to start a career in the aerospace industry.